

The official bi-monthly publication of Bhabha Atomic Research Centre



BARC

newsletter

May-June 2022



Improved Osseointegration

Laser assisted surface microstructuring of biomaterials

Editor

Dr. S. Adhikari

Editorial Assistant

Shri Madhav N

Design & Creative Work

Shri Dinesh J. Vaidya

Shri Madhav N

Newsletter Committee**Chairman**

Dr. A.P. Tiwari

Members

Dr. A.K. Nayak

Dr. G. Sugilal

Dr. V.H. Patankar

Dr. (Smt.) B.K. Sapra

Dr. L.M. Pant

Dr. Ranjan Mittal

Dr. (Smt.) S. Mukhopadhyay

Dr. K.P. Muthe

Dr. V. Sudarsan

Dr. A.V.S.S.N. Rao

Dr. S.R. Shimjith

Dr. Sandip Basu

Dr. Pranesh Sengupta

Dr. R. Tripathi

**Member Secretary &
Coordination**

Shri Madhav N



BARC Newsletter

May-June 2022

ISSN: 0976-2108



TECHNOLOGIES FOR
NEW INDIA @ 75

आज़ादी का अमृत महोत्सव



EDITOR'S MESSAGE

This issue of BARC Newsletter is a compendium of articles, which encapsulate activities in various domains of basic sciences and engineering, as part of R&D mandate of the Department of Atomic Energy (DAE). Activities of BARC related to healthcare, food security, clean drinking water, which impact positively to the society, are covered in this issue.

BARC continues a strong impetus for expanding the spectrum of activities under radiopharmaceuticals. One of the articles in this issue describes an Immuno Assay Kit developed by the Radiation Medicine Centre, a unit of BARC. The kit measures serum thyroglobulin *in vitro* in differentiated thyroid cancer patients.

Besides, this issue also reports numerous new developments, including ongoing studies on frozen coolant salt for Molten Salt Breeder Reactor, microstructural and diffraction studies on Th-U-Mo (metallic fuel) alloys, waste water management, fluorescence based techniques for chemical and biochemical applications, use of laser assisted surface microstructuring of several biomaterials, and various other activities, which are being explored to lay open new horizons of science and technology in the country.

We take this opportunity to thank everyone for their committed efforts that have contributed positively to the preparation and timely release of this issue of newsletter. We hope this publication would find considerable appeal among the readers and would eventually trigger greater levels of curiosity in their minds. Finally, it occurs naturally to us in our thinking that the contents would help to improve overall understanding of the readers on the range of activities of BARC.

(Dr. Soumyakanti Adhikari)
Editor and Head, SIRD



RESEARCH AND DEVELOPMENT

- 7** Development of Immunoradiometric Assay Kits for Measuring Serum Thyroglobulin in Differentiated Thyroid Cancer Patients
Chandrakala Gholve et al.
- 13** Development and Shelf-life Extension of Nutritious RTE Fish Spread using Gamma Irradiation
Aarti S. Kakatkar et al.
- 17** Development of an Effective Industrial Effluent Treatment System for Irrigation Purposes
Snehal Kale et al.
- 20** Development and Installation of Remotely Operated Telescopic Camera System to View Pouring and Handling Operations
Rahul Tripathi et al.
- 26** Influence of Picosecond Laser Induced Topographical Modification on *In-vitro* Osseointegration of Ti6Al4V bio-alloy
Sunita Kedia et al.
- 30** Polarization-based Laser Resonator Cavity
Siba Prasad Sahoo et al.
- 34** Thermophysical Properties of Frozen Coolant Salt
Rimpi Dawar et al.
- 39** Microstructural and Diffraction Studies on Th-U and Th-U-Mo Alloys
Raj Kumar et al.
- 47** Studies on Surface Plasmon Coupled Fluorescence with a Custom-made Optical Setup for Measuring Angle-resolved Emission Spectra
S. Dutta Choudhury
- 52** Remotely Operated UHV Compatible Sample Manipulator for Spectroscopy Synchrotron Beamline at Indus-2
A.D. Patil et al.
- 55** Special Design Considerations Applicable for Civil Structures and Foundations for Electrical Substations of Nuclear Facilities
Saha Dauji et al.

RESEARCH SYNOPSIS

- 61** Microbial Iridescence in Uranium Tolerant Bacterium
Celin Acharya

NEW TECHNOLOGIES FOR SELF-RELIANT INDIA

- 62** A New Milestone in Vitrification of Nuclear Waste
Subrat Kaushik et al.

BOOK REVIEW

- 64** Smarting Energy Management - The IIoT Way
A.K. Bhattacharjee

POPULAR SCIENCE

- 65** ISO 45001:2018 - The New Occupational Health & Safety Management System
Vyom Saxena

OUTREACH

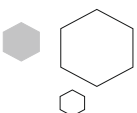
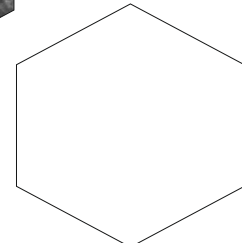
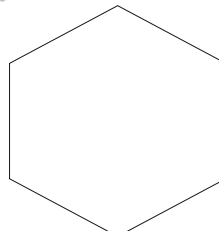
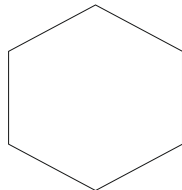
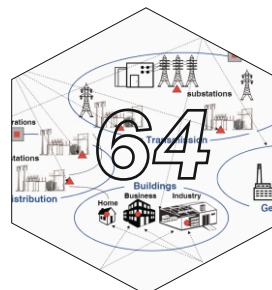
- 70** Students of Gujarat visit BARC.
Mega Exhibition in Dehradun.
Student Outreach in Kolkata.

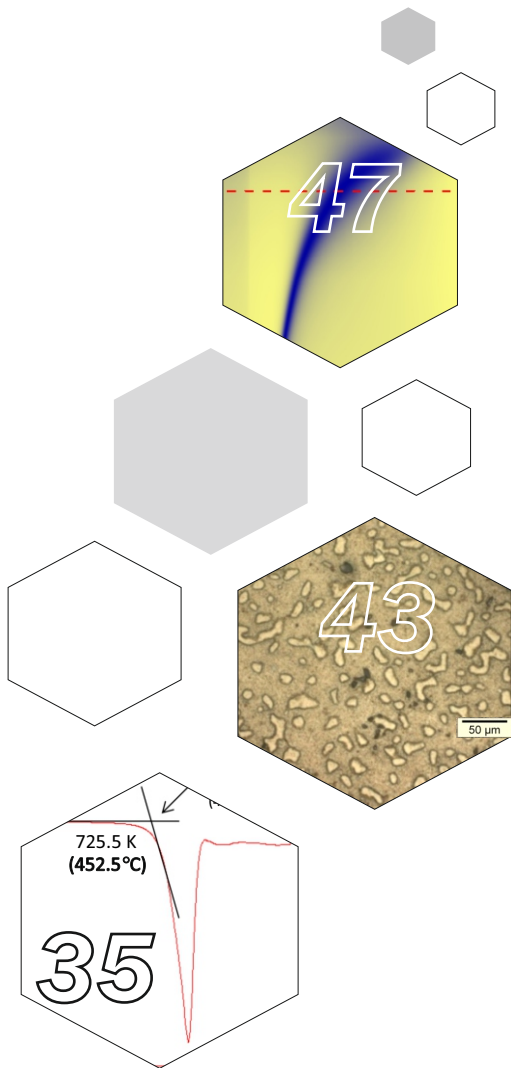
CONNECT

- 72** 65th Solid State Symposium.
16th Radiation and Photochemistry Symposium.

AWARDS AND HONORS

- 74** Tarun Datta Memorial Award to BARC Scientist



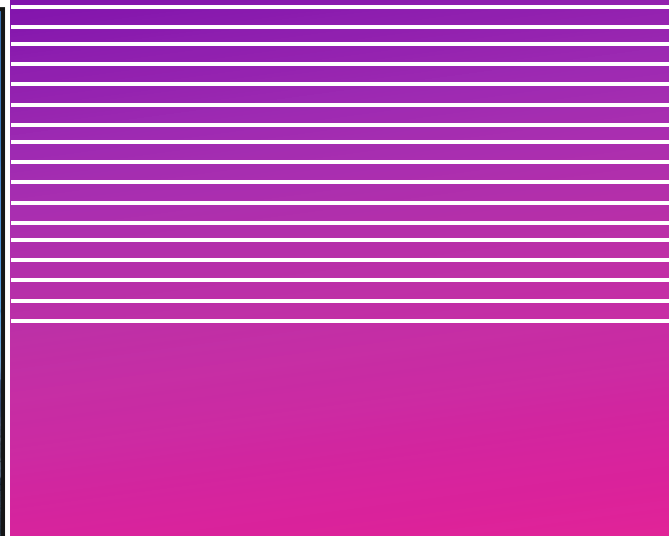


C O N T E N T S

FORTHCOMING ISSUE

Key Highlights

- Very High Energy Gamma-ray Astronomy
An Indian Perspective
- MACE TELESCOPE**
- Conceptualizing the Telescope
A Brief Historical Account
- Simulation Studies...
- Optical System...
- Camera and Subsystems...
- Observation, Data Acquisition & Monitoring...
- Commissioning Activities... ■ Exploring the Nature of Dark Matter... ■ Life in Hanle...



This page is intentionally left blank

Biochemical Tumour Marker

Development of Immunoradiometric Assay Kit for Measuring Serum Thyroglobulin in Differentiated Thyroid Cancer Patients

Chandrakala Gholve^{1*}, S. K. Ghorui², J. Kumarsamy¹, Archana Damle¹ and Savita Kulkarni¹

¹Radiation Medicine Centre, BARC, TMH Annexe, Mumbai-400012, INDIA

²National Research Centre on Camel, Bikaner-334001, INDIA



RMC-Tg kit (deployed as biochemical tumour marker) developed in Radiation Medicine Centre

ABSTRACT

Thyroglobulin (Tg) serves as a useful biochemical tumour marker in follow-up cases of patients with differentiated thyroid carcinoma (DTC). A sensitive immunoradiometric assay (IRMA) for serum thyroglobulin (Tg) estimation was developed at Radiation Medicine Centre, with analytical and functional sensitivities of 0.10 ng/ml and 0.4 ng/ml, respectively. The assay uses anti-Tg camel polyclonal antibody as capture antibody and ¹²⁵I labeled monoclonal anti-Tg antibody as detector antibody. A good correlation was obtained on comparison with commercial Izotop® TG IRMA kit (n=142, r=0.98, p<0.001). So far, we have analyzed approximately 36,000 routine clinical samples with the new in-house developed kit. Indigenously developed radioisotopic TG IRMA kit (RMC-Tg KIT) is convenient, robust, cost-effective, automated and is being used satisfactorily for the last 8 years, in the routine *in-vitro* 'Immunoassay Services' at RMC by substituting the expensive commercial Tg kits.

KEYWORDS: Thyroglobulin, Camel polyclonal antibody, Differentiated thyroid carcinoma, Immunoradiometric assay, Monoclonal antibody, Sensitivity.

Introduction

Radiation Medicine Centre (RMC), a Nuclear Medicine Department of Bhabha Atomic Research Centre, is one of the largest referral bases in India for the management of patients with various thyroid disorders including differentiated thyroid cancer (DTC)[1]. For the better management of patient services, various developments; including *in-vivo* and *in-vitro* diagnostics, and therapeutic strategies are continuously being explored and applied here. RMC being a pioneer in Nuclear Medicine is equipped with the infrastructure for the development and use of radioisotopic kits for routine *in-vitro* patient services. Various assay formats for serum thyroglobulin (Tg) and thyroid autoantibodies *viz.*, anti-Tg autoantibody (TgAb) and anti-thyroid peroxidase autoantibody (TPOAb) have been developed and validated at RMC[2-6]. Present work herewith also endeavors to fulfill the prerequisite by using the in-house developed TG IRMA kits (RMC-Tg KIT) for *in-vitro* measurement of Tg in DTC patients.

Patients diagnosed with DTC following thyroidectomy undergo radioiodine (¹³¹I) therapy for ablation of residual thyroid tissue and treatment of recurrent disease and metastases[7]. Serum Tg is an established tumour marker used in the management of DTC patients. Several methods for the measurement of serum Tg are being used depending upon the prerequisite and infrastructure available at the institution. The type of method, radioimmunoassay (RIA) or immunometric assay (IMA), used to measure Tg in sera, governs the clinical utility and interpretation of Tg values. Currently, commercial assays favor

the IMA technique, because RIA poses certain technical limitations like long incubation times, limited working ranges, short shelf-life and inherent instability of the tracer (¹²⁵I-Tg). In contrast, IMA methods achieve better sensitivity than RIA in a shorter incubation time, cover a broader working range, use a more

labeled antibody preparation and in their non-radioisotopic format, *viz.*; chemiluminescent immunometric assay (CLIA) have the potential to be automated. However, non-radioisotopic assays like CLIA and Fluoroimmunoassay have a high background (due to autofluorescence of biological samples and/or interfering compounds) and high instrumentation cost. Today even after radical advancement in the immunoassay methodologies, measurement of Tg still remains technically challenging, thereby influencing the clinical reliability of Tg determinations. Lack of universal method standardization, inadequate assay sensitivity (especially with RIA) and precision; and interference from heterophilic antibody or Tg autoantibody (TgAb) that can cause under or overestimation in Tg concentration are the key factors responsible for the reliability of current Tg assays[8]. However, due to the occurrence of TgAb in approximately 25% of DTC patients; its detection and evaluation of its interference during serum Tg measurement becomes mandatory [8]. Community Bureau of Reference has developed an international Tg reference preparation, CRM 457, which is being used directly or indirectly for calibration in most immunoassays[3, 8].

The development of a two-step immunoradiometric assay (IRMA) using rabbit anti-Tg polyclonal antibodies has been discussed earlier[3]. The development of IRMA for routine

*Author for Correspondence: Chandrakala Gholve
E-mail address: kalagholve@barc.gov.in

clinical use in patients demanded a large and uninterrupted supply of antibodies, and producing IRMA kits using commercial antibodies was also not economically feasible. Given this, present efforts were directed to develop an IRMA system that uses anti-Tg polyclonal antibodies from a larger species like a camel. In this collaborative work, anti-Tg polyclonal antibodies were raised in camels at ICAR (Indian Council of Agricultural Research)-National Research Centre on Camel, Bikaner. In the one-site IRMA system mentioned here, Tg is captured onto anti-Tg camel polyclonal antibody (PAb) bound or immobilized on a solid-phase (polystyrene tubes). The assay is carried out by reacting ¹²⁵I labeled monoclonal anti-Tg antibody (¹²⁵I-MAb) with Tg, which is bound to the PAb on the solid phase. Excess of unreacted ¹²⁵I-MAb is removed by washing the tubes with the wash buffer. The sandwich formed remains bound to the solid-phase antibody which is later quantified by counting the bound radioactivity in a gamma counter. The concentration of Tg in samples is directly proportional to the radioactivity and is obtained by interpolation from the standard curve.

Thyroglobulin autoantibody, heterophile antibodies, or non-specific effects in a patient's serum can interfere with serum Tg measurement thereby giving underestimated or overestimated Tg values depending upon the type of assay used[8]. Nevertheless, the presence of TgAb leads to

underestimation of the Tg concentration in the IRMA system which can be detected by performing parallelly the 'Tg-Recovery Test' for each sample under investigation, using RMC-Tg KIT.

RMC has a large registry of more than 15,000 DTC patients who are monitored for the efficacy of treatment during their routine follow-up. Management of these patients is based on serum Tg measurement and ¹³¹I whole-body scanning. Hence, our aim was to develop a low-cost in-house TG IRMA kit for the estimation of serum Tg in these patients; as an import substitute for high-cost commercial IRMA kits. This article reports the development of single-step IRMA for serum Tg measurement for routine clinical use in DTC patients. The flow chart in Fig.1 illustrates various steps involved in the development of RMC-Tg KIT. About 5800 patient's sera are quantitated annually for Tg and Tg-Recovery using the indigenously developed kits. Our end-users are patients from RMC OPD, Tata Memorial Hospital, Rajiv Gandhi Cancer Institute and Research Centre, New Delhi; and a few nearby Government hospitals (Fig.2). In the past 8 years, we have produced approx. 1702 kits (100 determinations/kit) and have investigated around 36,000 routine serum samples for Tg and 'Tg-Recovery Test'.

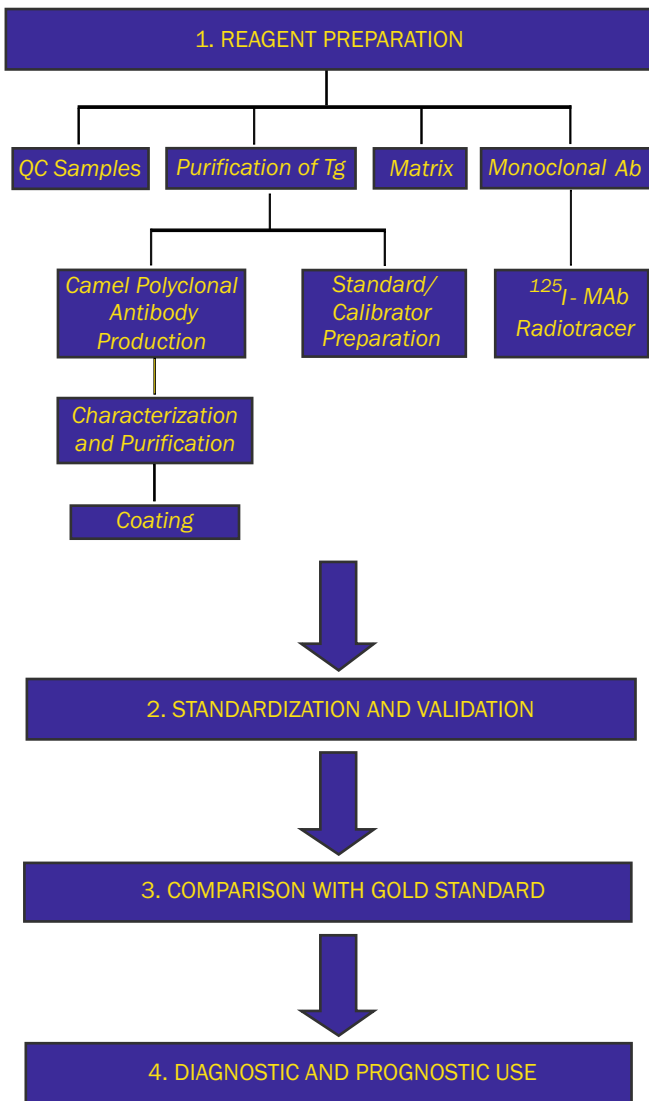


Fig.1: Steps involved in the development of RMC-Tg KIT.

Important Highlights of the Work

1. Reagent preparation in bulk for the production of indigenous RMC-Tg KITS.
2. Standardization and Validation of the in-house developed Tg IRMA assay.
3. Comparison of in-house Tg IRMA assay with a gold standard method.
4. Application of RMC-Tg KITS for the management of DTC patients at RMC.
5. Novel components of the RMC-Tg KIT influencing the total production cost.
6. Retrenchment in the Organizational Annual Budget by replacing Commercial TG Izotop® kit with cost-effective in-house developed RMC-TgKIT.

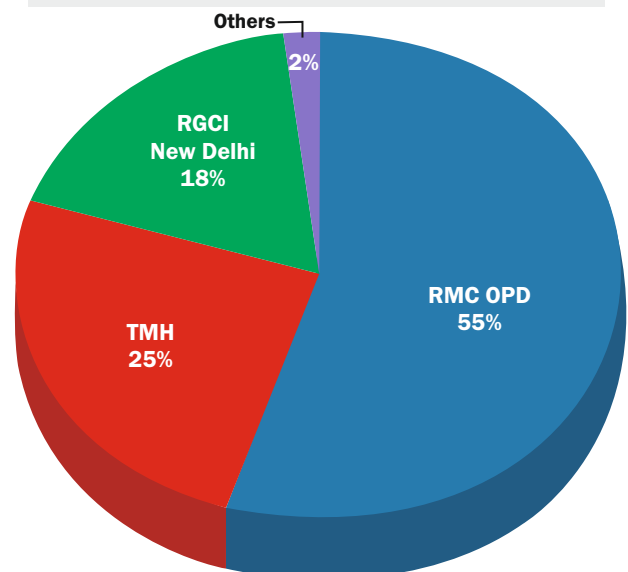


Fig.2: End-users of the indigenously developed RMC-Tg KIT and their break-up.

Experimental

1. Reagent Preparation

i. Extraction and purification of human Tg (antigen preparation)

The in-house purified Tg from normal human thyroid tissues was extracted within 4-6 h of the autopsy, purified and used for standard preparation and evaluation by comparing the dose-response curves with Izotop® kit standards. Various steps followed in the purification of Tg are illustrated in Fig.3. Standards with varying Tg concentrations were prepared using different matrices: synthetically prepared in-house matrix, human hormone-free serum and pooled Tg serum samples from disease-free DTC patients. Tg levels assayed using these matrices were compared with commercial kit (Izotop® TG IRMA kit) results. The Izotop® kit standards were calibrated against CRM 457. The stocks of purified Tg (preserved in phosphate-buffered saline) are maintained at -30 °C at RMC.

ii. Production of camel anti-hTg polyclonal antibody

Antibodies to human Tg were raised in 2 young male Indian Camels (*C. dromedarius*, J242 and J244) by subcutaneous immunization with 400 µg of in-house purified Tg in Complete Freund's Adjuvant. Following the initial dose, 3-4 booster doses with the same amount of Tg in Incomplete Freund's adjuvant were administered after 3-4 weeks respectively. The camels were then bled at fortnightly intervals after the final booster. Antisera were characterized for their specificity, avidity and titre; and stored at -20 °C till further use.

iii. Immobilization of camel polyclonal anti-Tg on polystyrene solid-phase

By passive adsorption, the polystyrene tubes were immobilized with approximately 50 µg of caprylic acid fractionated [9] or ammonium sulfate precipitated camel Ig fraction of PAb (in 0.3 ml of 0.1 M borate buffer, pH 8.0) and incubated overnight at room temperature. The unbound PAB solution was aspirated and the tubes were washed twice with 2 ml of 0.1 M NaHCO₃ buffer. The empty sites on the polystyrene surface were blocked with 0.5 ml of 0.1 M Tris buffer containing 0.3% BSA (w/v) and 1% sucrose (w/v) for an overnight period. The blocking solution was aspirated and the tubes were air-dried for an overnight period and stored in airtight plastic zip sealed bags at 4 °C for further use. The entire antibody coating process which is a labor-intensive step is performed manually. Antibody pipetting is done manually using Eppendorf-Multipette whereas aspiration and washing are performed using an in-house fabricated aspirator and washer.

iv. Radioiodination of monoclonal anti-Tg antibody

In-house produced murine anti-Tg monoclonal antibody (MAb) [10] was labeled with Na¹²⁵I by iodogen method following radioiodination protocol mentioned in our earlier report[3].

2. Standardization and Validation of Tg assay

Various reaction parameters such as concentration of reagents, reaction kinetics, sequential addition of reagents, time, temperature, etc. were evaluated to arrive at a suitable assay system which is given in Table 1.

Sensitivity, non-specific binding (NSB), precision, reproducibility, recovery, and dilution test were some of the quality control parameters performed to evaluate the performance of indigenous Tg IRMA assay. Considering 20% coefficient of variation (CV) as the acceptable assay precision, the working range was determined from the precision profile. The assay was studied for the influence of excess Tg concentration leading to high dose 'Hook-Effect'. The stability

Table 1: Optimized parameters of Tg assay.

Parameter	Optimized values
Concentration of capture antibody (PAb)	~ 50 µg/tube
Coating volume	300 µl
Standard/sample volume	100 µl
Concentration of tracer antibody 125 I-MAb	4800 Bq/200 µl
Incubation Period	15-16 hrs

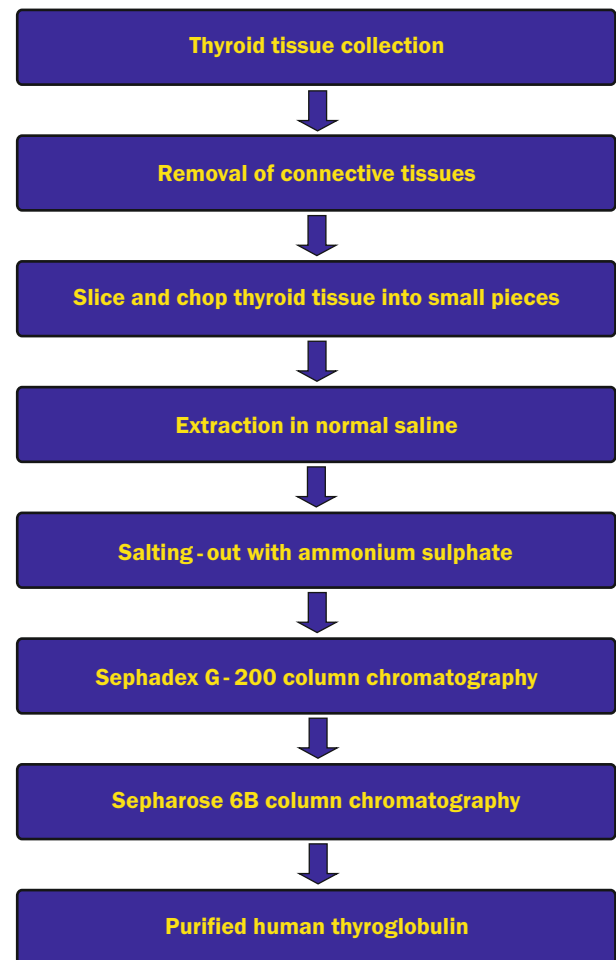


Fig.3: Extraction and purification of thyroglobulin obtained from human thyroid tissue.

of the capture antibody (antibody-coated tubes stored at 4 °C) was established by checking the immunoreactivity of the antibody-coated tubes for 24 months.

Tg IRMA protocol

To the antibody-coated tubes, the following components were added in sequence:

- 100 µl standard Tg, QC or serum sample.
- 200 µl of ¹²⁵I-MAb (4800 Bq).
- Incubate the tubes overnight (optimized for 15-16 h) on an orbital shaker at room temperature.
- Aspirate the content of tubes and wash twice with 2 ml of wash solution (PBS with 0.05% Tween 20).
- Decant the fluid and blot on filter paper and count the tubes for radioactivity in RIASTAR Multi-well gamma counter/SR 300 RIA autoanalyzer.

Table 2: Overview of Cost and total number of RMC-Tg KIT(s) produced and utilized in RMC.

Overview of RMC-Tg KIT production		
1.	RMC-Tg KITS produced Since 2014	1702 (170200 Tubes)
2.	Samples analysed Since 2014	72000 Determinations
	Tg Tg Recovery test	36000 36000
3.	Cost (in Rupees)/Kit (100 Determinations)	
	Commercial (IZOTOP Kit)	~17,500
	RMC-Tg KIT	~2500
4.	Annual Cost of TG Kits (in Rupees)	
	Commercial (IZOTOP Kit)	~40,00,000
	RMC-Tg KIT	~5,50,000

Tg-Recovery Test

The concentration of the recovery serum (approximately 500 ng Tg/ml) is checked with serum diluent or diluent recovery (DR) reference tubes. Recovery (in %) in each serum sample is then calculated using the following formula [2].

Recovery (in %) in the serum sample:

$$\frac{\text{ngTg/ml } R_x - \text{ng Tg/ml } S_x}{\text{ng Tg/ml DR}} \times 100 = \% \text{ Recovery}$$

Where Rx is recovery obtained, Sx is the Tg concentration for the sample and DR is the recovery obtained with serum diluent (to check the concentration of recovery serum).

3. Comparison of in-house Tg Assay with a Gold Standard Method

Serum samples from patients referred to Radiation Medicine Centre, with an established diagnosis of DTC (n=142) were analyzed for the presence of serum thyroglobulin. Developed serum RMC-Tg KIT was validated and compared with a gold standard and commercially available TG Izotop® kit. A linear regression analysis was performed for the data obtained.

Results and Discussions

Serum Tg measurement is a technically challenging assay for a marker of choice during the follow-up of DTC patients. Hence, the user of Tg assay should be well-versed about the technical difficulties. At our Centre, because of an increasing number of samples for serum Tg estimation, we developed TG IRMA wherein all the reagents are prepared in-house viz., hTg, anti-Tg antibodies (PAb and MAb), tracer, matrix, standards and QC samples. One of the principal reagents involved in the manufacture of TG kits is purified Tg from human thyroid tissue. Commercially available human Tg is highly expensive. Therefore, at RMC, we have extracted and purified approximately 1200 mg of Tg (total Tg yield) from two thyroid tissues which is being used for immunization, standard preparation and radiolabeling (for testing the antibody titre).

These purified Tg stocks are appropriately stored at RMC and apart from its main use in RMC-Tg KIT production had other applications too [11-13].

The uniqueness of the in-house developed Tg assay lies in the application of camel polyclonal antibodies for immobilization as a capture antibody. Conventionally immunometric assays for Tg uses a panel of two or more monoclonal antibodies for capture or signal. Nonetheless, the use of monoclonal antibodies has a limitation of Tg epitope specificities in detecting abnormal tumor Tg isoforms[14]. Secondly, in comparison to rabbits [3], camel provides a large supply of polyclonal antibodies, which is one of the prerequisites during the development of any non-competitive immunoassays. Thus, the preparation of reagents in bulk for the production of RMC-Tg KIT has greatly reduced the overall cost in comparison to the highly expensive imported TG IRMA kits (Table 2), without compromising on the quality of the performance. In addition to this, by adopting a passive adsorption method of coating as compared to chemical means [3] there is a reduction in the overall time taken and the manpower involved in the antibody immobilization process; a contributing aspect in reducing the cost of the kit. Initially, we had used the ammonium sulfate precipitation method as it is the most commonly used method. But later switched over to the caprylic acid method as it yields a high amount of purified IgG without reducing antibody titre, immunoreactivity, and distorting its structure. The stability of the capture antibody (camel anti-Tg coated tubes stored at 4 °C), was checked for 24 months which showed specific binding ranging between 35 to 45% and NSB between 0.10 to 0.25%. Therefore, even the 24-month-old antibody-coated tubes could be used satisfactorily for the estimation of Tg.

Variations between different methods used for assaying serum Tg arises from differences between the matrix used to prepare standards and dilute patient’s serum. We have prepared a well-defined stable matrix, synthetic hormone-free serum (SFS) and determined its utility as a stripped-out serum substitute in assays for serum Tg. This allows the production of the matrix in bulk quantities, with precise lot-to-lot consistency. Additional benefits include the complete absence of endogenous Tg, interfering antibodies, and potentially harmful bloodborne pathogens. The in-house prepared Tg standards were evaluated by comparing dose-response curves for in-house standards and Izotop kit standards. Standard curves were found to be almost superimposable (Fig.4) indicating that it can be used for Tg IRMA assays for clinical application.

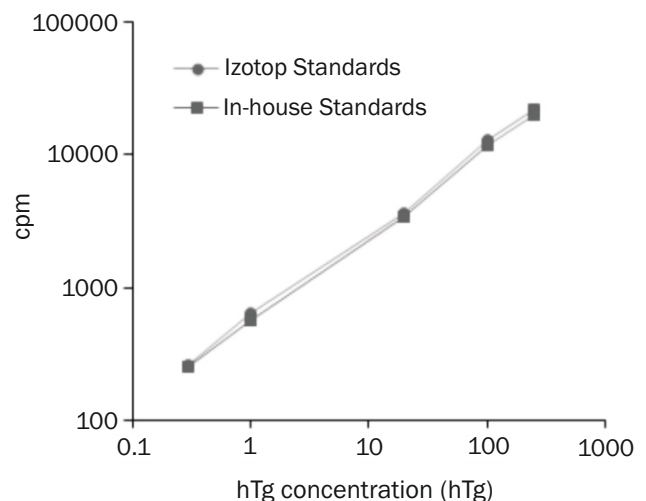


Fig.4: Comparison of dose response curves for in-house and Izotop® kit standards.

Recovery and dilution tests were also performed to ensure the accuracy and suitability of the matrix used for making standards. However, in our laboratory for routine usage, RMC-Tg KIT(s) are being produced using the leftover (excess) TSH standards (prepared in bovine serum) from Immunotech, France, after further appropriate modification and testing (viscosity of the matrix is compared with that of the SFS and dose-response curves are compared); as a basis of the matrix for preparing Tg standards. This has tremendously helped us in making in-house produced RMC-Tg KIT more economical.

Fig.5 shows two distinct peaks obtained after labeling anti-Tg monoclonal antibodies. The first peak corresponds to radiolabeled antibody and the second to free iodide. The labeling efficiency and specific activity ranged from 70-85% and 444-703 kBq/ μ g respectively. Sensitivity and NSB for IRMA assays are governed by two important parameters viz; specific activity and quality of the labeled antibody. The assay has been well optimized for radioiodination procedure to yield an assay with analytical and functional sensitivities of 0.10 ng/ml and 0.4 ng/ml respectively, and NSB < 0.2%.

Intra-and-inter-assay precision was respectively determined by setting-up replicates of two quality control samples in a single assay as well as in assays carried out at different intervals. Analytical recovery, estimated by adding a known amount of Tg to two serum samples, negative for the presence of TgAb, ranged from 78% to 120%. Parallelism of the assay was evaluated by assaying a serum sample, with high Tg content, serially diluted using matrix. The observed concentration to the expected (% O/E) ranged from 82% to 120% displaying a good agreement between the two. With 20% CV as the acceptable assay precision, the working range was determined as 0.4-300 ng/ml. TG IRMA which is an 'inclusive-assay' did not show any kind of high dose 'hook-effect' up to a concentration of ~12,800 ng/ml. The salient features of the indigenous RMC-Tg KIT are listed in Table 3.

Laboratories can implement one of the steps to identify TgAb interferences; measurement of TgAb, discordance between Tg values by RIAs and immunometric assays; and recovery of added Tg[7]. We used the 'Tg-Recovery Test' for detecting the interference of anti-Tg autoantibodies in the Tg IRMA system. Recoveries obtained between 80% and 130% are considered valid, levels of <70% or >130% are due to interference (autoantibody interference and non-specific serum interference) and the Tg level of the relevant original sample is considered invalid. Levels between 70%-80% are due to equivocal autoantibody interference. Tg Recovery (%) in

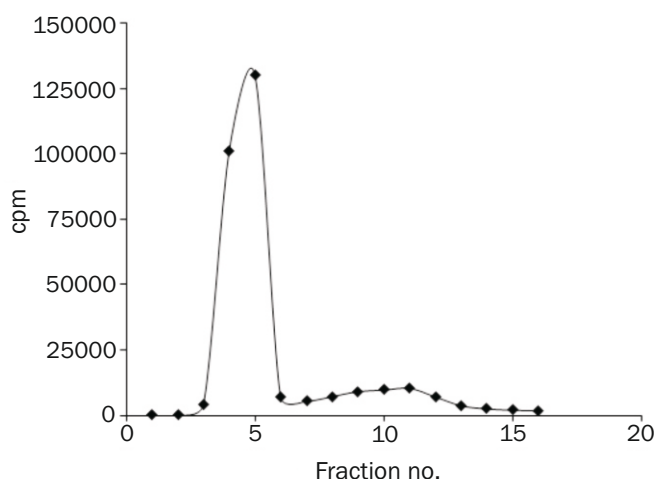


Fig.5: Elution profile of ¹²⁵I-monoclonal anti-Tg antibody post radiolabeling.

Table 3: Salient features of RMC-Tg KIT.

Parameter	TG IRMA
Sensitivity	
a. Analytical	0.10 ng/ml
b. Functional	0.40 ng/ml
NSB	< 0.2%
Precision	
a. Intra-assay variation	Control A: 0.9 ± 0.09 ng/ml, % CV=9.9 Control B: 73.9 ± 5.8 ng/ml, % CV=7.8
b. Inter-assay variation	Control A: 0.95 ± 0.13 ng/ml, % CV=14.4 Control B: 77.8 ± 8.9 ng/ml, % CV=11.5
Recovery	78 to 120%
Linearity	82 to 120
Assay range	0.1-300 ng ml
Hook effect	No hook effect up to 12,800 ng/ml
Stability of antibody coated tubes	24 months
Stability of tracer	2 months
Incubation time	15-16 hrs.

complement with Tg IRMA information aids in recognition of interference in Tg measurements[15].

Comparison of Tg levels in the serum sample of patients with DTC, estimated by the present method and by Izotop TG IRMA kit, showed good agreement. Regression analysis showed good correlation (r=0.98, n=142, p<0.001) as shown in Fig.6. TgAb positive samples were excluded from the analysis as they are known to interfere in all Tg assays. Use of different sources and nature of kit calibrators, heterogeneity of analyte, antibodies with different specificities towards the Tg isoforms are all responsible for variations in Tg values obtained using different methods. Most of the Tg assays use CRM 457 for calibration, still, inter-method variability exists. Therefore, as recommended by American Thyroid Association, the same immunoassay should be used while monitoring an individual patient [16].

Conclusion

This publication addresses the preparation of principal reagents and steps involved in the production of indigenous RMC-Tg KIT (Fig.7) at the laboratory level for monitoring of serum Tg levels which is of great clinical significance in the long-term management to detect recurrence of disease, monitor the course of the disease and efficacy of the treatment in DTC. The average serum Tg test cost (without anti-Tg autoantibody test/information) in various Indian cities is approximately ₹1000. Therefore, to meet the growing demand of RMC-Tg KIT, automation in coating procedure would support large-scale production, thereby extending the benefit to a large number of patient population. The in-house developed kit is convenient, robust, cost-effective, fully automated for SR 300 RIA autoanalyzer and is being used satisfactorily in RMC for routine patient service for the last 8 years (Fig.8) by replacing

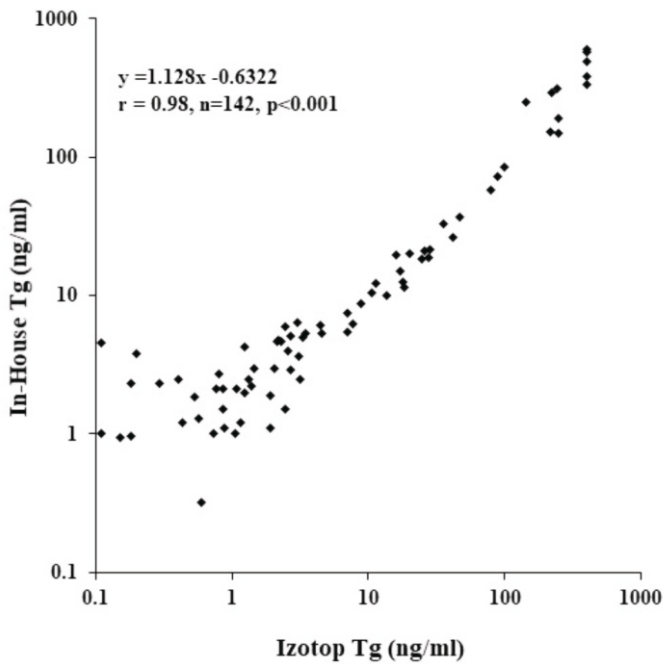


Fig.6: Scatter diagram for Tg by in-house RMC-Tg KIT and commercial TG IRMA kit (Izotop) in TgAb negative samples.

the imported and expensive commercial Izotop TG IRMA kits. Indeed, Radiation Medicine Centre is the only Centre in India that produces and uses entirely indigenously developed RMC-Tg KITS for routine measurement of serum Tg in DTC patients (approx. 36,000 clinical samples analyzed so far). For the larger benefit of the society, we have thereby encompassed the application of radioisotope technology in the field of Nuclear Medicine.

Acknowledgements

The authors would like to thank P. K. Pujari, Head, Radiation Medicine Centre for his support and encouragement. Sincere gratitude to the Former Heads of RMC, M.G.R Rajan for his guidance and motivation for initiating the work and Smt. Sharmila Banerjee, for her invaluable support and encouragement. The authors whole-heartedly thank Jayendra Mori, U. Shaikh, Dinesh Bagul, Keshar Singh, D. S. More, Smt. Kanta Ayer and Rahul Kashid for their involvement at various stages of this work. Sincere thanks to collaborators, N.V. Patil and Rajesh Sawal, Former Director(s), ICAR-NRCC, Bikaner for their continuous support during the course of the work.

References

[1] A. Kalshetty and S. Basu, Indian J. Nucl. Med., 2018, 33, 218-223.
 [2] C. S. Gholve. Studies on solid-phase immunoassays for serum thyroglobulin with specific reference to the influence of anti-thyroglobulin autoantibodies. M.Sc. thesis, University of Mumbai, India, 2009.
 [3] C.S. Gholve, J. Kumarasamy, A. Damle, S. Kulkarni and M.G.R. Rajan, Indian J. Appl. Res., 2016, 6(3), 468-472.
 [4] C.S. Gholve, J. Kumarasamy, S. Kulkarni and M.G.R. Rajan, Indian J. Clin. Biochem., 2017, 32(1), 39-44.
 [5] C.S. Gholve, S. Banerjee and S. Kulkarni, J. Radioanal. Nucl. Chem., 2020, 323(3), 1041-1046.
 [6] C.S. Gholve, A. Damle, S. Kulkarni, S. Banerjee and M.G.R. Rajan, Indian J. Clin. Biochem., 2021,



Fig.7: In-house made RMC-Tg KIT.

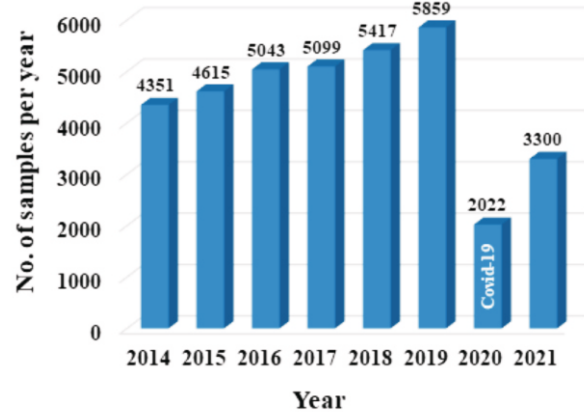


Fig.8: No. of serum samples sent for Tg analysis at RMC saw a drastic fall in 2020 and also in the following year, which is mainly due to the onset of Covid-19 pandemic.

<http://doi.org/10.1007/s12291-021-01005-9>.

[7] C. Evans, S. Tennant and P. Perros, Scand. J. Clin. Lab. Invest., 2016, 76(sup245), S119-123.
 [8] C. S. Gholve, J. Kumarasamy, A. Damle, S. Kulkarni, M. Venkatesh, S. Banerjee and M.G.R. Rajan, Indian J. Clin. Biochem., 2019, 34(4), 465-471.
 [9] C. S. Gholve, J. Kumarsamy, A. Damle, S.K. Ghorui, N.V. Patil, S. Kulkarni and S. Banerjee, Indian J. Clin. Biochem., 2018, doi.org/10.1007/s12291-018-0795-1: p101.
 [10] A.A. Damle, A.A. Narkar and D.H. Shah, Indian J. Exp. Biol., 2004, 42(4), 354-360.
 [11] B. Jain, J. Kumarasamy, C.S. Gholve, S. Kulkarni and M.G.R. Rajan, Indian J. Clin. Biochem., 2017, 32(2), 193-199.
 [12] B. Jain, J. Kumarasamy, C.S. Gholve, S. Kulkarni, M.G.R. Rajan, J. Immunoassay Immunochem., 2017, 38(3), 271-284. doi:10.1080/15321819.2016.1250771.
 [13] J. Kumarasamy, S. K. Ghorui, C. S. Gholve, B. Jain, Y. Dhekale, G. D. Gupta, A. Damle, S. Banerjee, M.G.R. Rajan and S. Kulkarni, J. Immunol. Methods., 2021, 492, 112990.
 [14] C. Spencer and S. Fatemi, Best Pract. Res. Clin. Endocrinol. Metab., 2013, 27(5), 701-712.
 [15] L. Giovannella, U. Feldt-Rasmussen, F. A. Verburg, S. K. Grebe, Stephan, M. Plebani, P. M. Clark, Clin. Chem. Lab. Med., 2015, 53(9), 1301-1314.
 [16] D. M. Rotteveel-de Groot, H. A. Ross, M. Janssen, R. T. Netea-Maier, J. D. Oosting, F. Sweep and A. E. van Herwaarden, Practical Laboratory Medicine. 2016, 5(1), 6-13.

Food Preservation

Development and Shelf-life Extension of Nutritious RTE Fish Spread using Gamma Irradiation

Aarti S. Kakatkar, Raj Kamal Gautam, Prashant K. Mishra, Vivekanand Kumar, Ashika Debbarma and Suchandra Chatterjee*

Seafood Technology Group, Food Technology Division, Bhabha Atomic Research Centre, Mumbai-400085, INDIA



Ready-to-eat fish spread

ABSTRACT

Modern lifestyle demands convenient, ready-to-cook (RTC), ready-to-eat (RTE), easily available and nutritious food. A high protein, low fat and no sugar-based spread was developed from readily available fish Bombay Duck (*Harpodonnehereus*). The shelf life of fish spread was extended by 2 months using gamma irradiation (5 kGy) and chilled storage (4 °C). Acceptability of the spread was confirmed based on microbiological, biochemical and organoleptic assessments. No significant change in the nutritional quality between non-irradiated and radiation processed samples was observed. The fish spread is safe for all consumers including diabetics and health conscious.

KEYWORDS: RTE, Fish spread, Nutritious, Shelf-life, *Harpodonnehereus*, Gamma irradiation

Introduction

Consumers' demand for healthy food products is increasing worldwide. Modernization has led to increase in the number of working personnel with higher income, education, better consciousness towards quality, freshness, nutrition, hygiene and health. This has necessitated supply of healthy, wholesome, nutritious diet consisting of low salt, low sugar, high protein and high fiber without compromising the taste. More emphasis is on development of convenient, minimally processed, ready to eat and easily available foods. Muscle food products are an essential component of a balanced diet in the developed countries. Their principal components, besides water, are proteins and fats, with substantial contribution of vitamins and minerals. Muscle proteins are of high nutritional quality due to their high biological value (BV) and bio-availability [1]. Fish is the most nutritious food consisting of proteins, long chain omega 3 fatty acids, vitamin D, selenium and iodine. This awareness has increased the demand for fish amongst the rich and the poor as a cheap and readily available source of nutrition. However, few convenient, RTC/ RTE fish products available in the supermarkets that include fish patties, fish burgers, cutlets, sausages etc. However, the fish-based products are highly perishable. There is a demand for meat-based spreads like fish spread which is not available at present. The Compounded Annual Growth Rate (CGAR) of spreads is expected to reach 23.7 billion by 2022[2]. In the present study, a low cost, easily available fish, Bombay duck (*Harpodon nehereus*) was used to develop a nutritious ready-to-eat (RTE) fish-spread and its shelf-life extension using gamma irradiation under chilled storage 4°C was studied by microbiological, biochemical, organoleptic and nutritional analysis.

Development of Fish Spread

Fresh beheaded, eviscerated and deboned fish (Bombay duck or Bombil,) was cleaned by chilled water (4°C) and cut into small pieces. The fish was steamed under pressure to soften the fish muscle which makes easier for removal of soft muscular bones and homogenized. This was homogenized with spices and ingredients like finely chopped and sautéed fresh onion (25 %), garlic (2.4%), ginger (1%), green chillies (3%), coriander leaves (3.5%). The samples were packed in polypropylene (PP) containers (Trendplast Pouch Pack Private Limited, Mumbai) of 3.5 mm height x 1.2 mm thickness x 70 mm diameter and sealed using multilayered aluminum foil lid by cup sealer (Aman Engineering Works, Mumbai) set at 250 °C. The developed product is shown in Fig.1.



Fig.1: Ready to eat fish spread.

Irradiation and Storage Studies

Samples were irradiated at a dose of 5 kGy in ice in food package irradiator (Atomic Energy of Canada Ltd, with a ⁶⁰Co source at a dose rate of 3 kGy/h) while un-irradiated samples served as control. The dose measurements were done using Fricke dosimeter. Both the samples were stored at 4°C and

*Author for Correspondence: Suchandra Chatterjee
E-mail: suchanc@barc.gov.in

Table 1: Nutritional Composition of Control and Irradiated (5 kGy) Fish Spread.

	Control	Irradiated
Energy (kcal/100g)	106.61±2.14 ^a	108.26±3.36 ^a
Protein(g/100g)	12.75±0.35 ^a	13.59±1.01 ^a
Fat	3.53±0.26 ^a	3.54±0.37 ^a
Carbohydrate	5.95±0.51 ^a	5.49±0.36 ^a
Sugar	0±0 ^a	0±0 ^a
Moisture	76.25±0.31 ^a	75.73±1.11 ^a
Ash	1.51±0.08 ^a	1.63±0.09 ^a

Results are expressed as Mean ± SD. The values are average of 3 independent experiments in triplicates (n=9). Values marked by same letter (superscripts) are not significantly different (P ≥ 0.05).

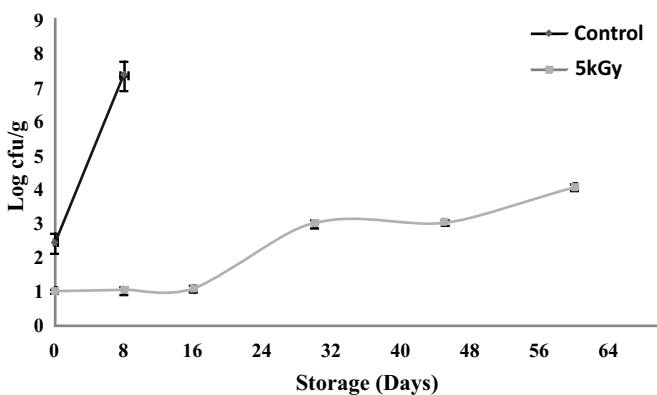


Fig.2: Total bacterial count (TBC) of control and irradiated (5kGy) on storage at 4°C. The values are average of 3 independent experiments in triplicates (n=9).

analyzed on 0, 8, 16, 30, 45 and 60 days for quality and acceptance by microbiological, biochemical and organoleptic analysis. Nutritional analysis was validated through National Accreditation Board for Testing and Calibration Laboratories (NABL) certified laboratory (Ram Krishna Bajaj CFBP Consumer Education and Testing Center, Mumbai, India). The statistical analyses were performed with DSASTAT ver, 1.101.

Results and Discussion

Nutritional Composition

Convenient, ready-to-eat, healthy food with high protein, low fat, low sugar is preferred by modern consumers. The market survey showed that the spreads had higher fat, sugar and low protein content. For example, an egg-less sandwich spread had fat content of 38.6%, protein content of 1.6%, sugar content of 8.2% and carbohydrate content of 8.7%; a cucumber carrot sandwich spread had fat content 37.4%, protein 2.0%, sugar content 13.2% and carbohydrate content of 18.2% while tomato onion jalapeno spread was low in fat (1.63%) as well as protein (0.71%) but contained 7% of sugar and 12.71% of carbohydrate. No significant (p <0.05) difference in nutritional composition of control and irradiated fish spread was observed (Table 1). The developed RTE fish spread has a high protein content of 12-14%, low fat (3-4%) and carbohydrate (5-6%) content with low sugar content, making the fish spread a suitable choice for all including special requirement group like diabetics and calorie conscious consumers.

Microbiological Analysis

The initial bacterial load (2.42 ± 0.28 log cfu/g) of fish spread was reduced to 1.01 ± 0.06 log cfu/g in irradiated samples immediately on the zero day. The control samples showed increase in the microbial load on the 8th day of storage (7.35 ± 0.43 log cfu/g) indicating spoilage while, irradiated samples showed a gradual increase to 4.07 ± 0.11 log cfu/g at the end of 60 days of storage at 4°C (Fig.2). Initially, total mold count was absent in both the samples which increased to 3.97± 0.01 logcfu/g after 8th day with mold growth visible on the control samples, while irradiated samples were free of mold growth till 60 days of storage. Similar results in the reduction of total microbial load and shelf life extension were observed in irradiated Threadfin bream whole fish, Tilapia fillets and Seer steaks on storage at 4°C [3-5]. The repair mechanism of bacteria is hampered due to various hurdles used in the development of product, which affects their growth and hence, are not able to survive for long [6]. Therefore, irradiation along with refrigerated storage is essential for lower bacterial load and shelf-life extension of the fish spread up to 60 days.

Fish and fishery products are known to be carriers of different food borne pathogens [7]. Therefore, screening for the presence of important food-borne pathogens is essential to ensure safety of fishery products. The fish spread was free of all the food-borne pathogens tested (*Escherichia. coli*, *Salmonella* spp, *Listeria monocytogenes*, *Yersinia enterocolitica* and coagulase positive *Staphylococcus aureus*). indicating that the pathogenic bacteria in and around fish may be low or cooking of raw materials may have helped in lowering the microbial load.

Irradiation is the most widely studied decontamination method in fish species and is utilized in fresh, frozen, canned, dried and cured fish and also in ready-to-eat fish products[8]. There are reports of radiation preservation of minced meat-based product (Pâté), produced mainly from a minced mixture of offal (particularly liver), muscle, fat, vegetables, herbs and spices which is cooked at relatively low temperatures[9]. Radiation treatment (2-4 kGy) of many RTE foods like dried meat (beef jerky), uncooked and fermented minced meat products (salami), cooked offal or minced meat products (chicken liver pâté or luncheon sausage), and cooked whole meat products (ham) caused reduction of *Salmonella* spp. or *L. monocytogenes*[10].

Biochemical Indices

The results suggest a positive correlation between increase in the bacterial load and increased TVBN and TMA in fish spread for control samples (Table 2). There was no significant difference (p <0.05) between the TVBN and TMA values of irradiated samples on storage; however, both control and irradiated samples showed the values within the prescribed limits of 35 mg N/100g and 15 mg N/100g respectively indicating a fresh original sample[11]. TVBN (8.4 ± 2.54 to 18.4 ± 2.42 mg N/100g) and TMA (3.51 ± 0.86 to 7.71 ± 0.50 mg N/100g) increased in control samples during storage of 8 days while it remained constant for irradiated samples up to 45 days and increased at the end of storage of 60 days (Table 2).

Both the control and irradiated samples showed increase in the TBA values from 1.67 ± 0.06 µg malondialdehyde/g (MA/g) to 1.95 ± 0.06 µg MA/g during storage of 8 days which are near the upper limit of 2 µg MA/g [11]. However, no significant difference (p>0.05) in TBA values was observed between control and irradiated samples on the same day

Table 2: Biochemical analysis of control and irradiated (5 kGy) fish spread on storage at 4 °C.

Parameters	Samples	Storage time (days)					
		0	8	15	30	45	60
TVBN (mg N/100g)	Control	8.4 ± 2.54 ^b	18.2 ± 2.42 ^a	ND	ND	ND	ND
	Irradiated	8.4 ± 1.19 ^b	8.4 ± 1.05 ^b	9.8 ± 2.42 ^b	9.8 ± 2.42 ^b	11.2 ± 2.42 ^b	19.8 ± 2.42 ^a
TMA (mg N/100g)	Control	3.51 ± 0.86 ^{cd}	7.71 ± 0.50 ^a	ND	ND	ND	ND
	Irradiated	2.93 ± 0.24 ^d	3.34 ± 0.37 ^{cd}	3.91 ± 0.24 ^c	3.42 ± 0.24 ^{cd}	5.60 ± 0.38 ^b	7.42 ± 0.24 ^a
TBA (µg MA/g)	Control	1.67 ± 0.06 ^d	1.95 ± 0.06 ^c	ND	ND	ND	ND
	Irradiated	1.74 ± 0.06 ^d	1.99 ± 0.06 ^c	2.34 ± 0.05 ^a	2.02 ± 0.07 ^c	2.13 ± 0.04 ^b	2.38 ± 0.06 ^a

ND= Not done as sample spoiled

Results are expressed as Mean ± SD. The values are average of 3 independent experiments in triplicates (n=9). Different letters (superscripts) in row/ column indicate significant differences ($P \leq 0.05$) for each biochemical analysis.

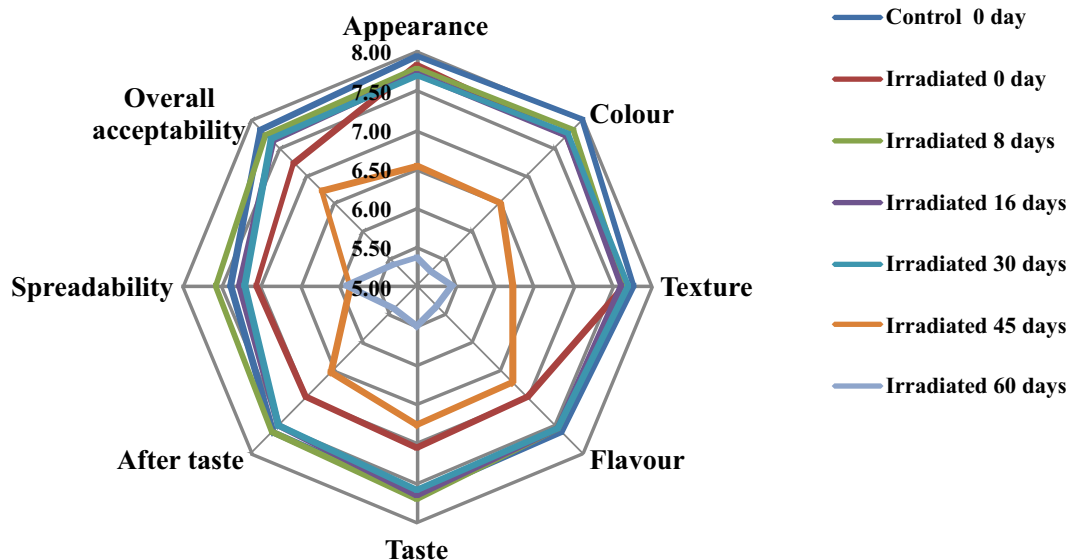


Fig.3: Web diagram showing organoleptic evaluation of control and irradiated fish spread on storage at 4 °C.

(Table 2). This may be due to low fat content of Bombay duck. These results are in accordance with other studies [12, 6].

Organoleptic Analysis

Organoleptic evaluation is the most popular method to assess freshness and acceptability of fish. Organoleptic properties including visual appearance, color, flavor and texture are the important parameters observed by the taste

panels during analysis. Initially, both control and irradiated samples had overall acceptability score of 7.8-7.2 respectively (Fig.3). The sensory web diagram showed no change in the sensory attributes of the irradiated samples on storage up to 30 days. However, on 45th day the overall score decreased to 6.7 (between like moderately and like slightly). On 60th day, score further decreased to 5.4 (between like slightly to neither like nor dislike). Thus, sensory acceptability decreased as the microbial load increased. Similar correlation between sensory

scores and microbiological quality was observed previously [13-14].

Conclusion

A nutritious and RTE fish spread was developed with readily available fish, Bombay duck using hurdles like radiation processing (5 kGy) and chilled storage (4°C). The product was microbiologically, biochemically and organoleptically acceptable up to 60 days. Therefore, we suggest a shelf life of 60 days for irradiated RTE fish spread when stored under chilled temperature. The RTE fish spread treated by irradiation with extended shelf-life is pathogen free, protein, PUFA rich, and sugar free, making it suitable for all consumers of different age groups, including infants, elderly, malnourished, calorie conscious people and diabetics. It can be an ideal breakfast bread spread. Regular use of such spreads may provide desired health benefits without additional dietary supplements.

Acknowledgements

Authors sincerely acknowledge technical assistance rendered by Shabbir Alam during entire study period.

References

- [1] Tahergorabi, R., Matak, K. E., Jaczynski, J. "Fish protein isolate: Development of functional foods with nutraceutical ingredients". *Journal of Functional Foods*, 2015, 18, 746- 756.
- [2] Euromonitor International <https://www.euromonitor.com/spreads-in-india/report> (accessed 09 October 2020).
- [3] Food safety and standard authority of India- 3rd amendment regulations, 2017, (<http://www.fssai.gov.in/>) (accessed 06 April 2021)
- [4] Jeevanandam, K., Kakatkar, A., Doke, S. N., Bongirwar, D., Venugopal, V. "Influence of salting and gamma irradiation on the shelf life extension of threadfin bream in ice". *Food Research International*, 2001, 34, 739- 746.
- [5] ElGhafour, S. A., Zakar, A. H. (2017) "Impact of gamma irradiation on the quality of tilapia fish (*Oreochromis niloticus*) stored under refrigerated condition". *International Journal of ChemTech Research*, 2017, 10, 573- 581.
- [6] Kakatkar, A.S., Gautam, R. K., Shashidhar, R. "Combination of glazing, nisin treatment and radiation processing for shelf-life extension of seer fish (*Scomberomorus guttatus*) steaks". *Radiation Physics and Chemistry*, 2017, 130, 303-305.
- [7] Leistner, L., "Basic aspects of food preservation by hurdle technology". *International Journal of Food Microbiology*, 2000, 55, 181- 186.
- [8] Venugopal, V., Doke, S. N., Thomas, P., "Radiation processing to improve the quality of fishery products". *Critical Reviews in Food Science*, 1999, 39, 391- 440.
- [9] Andoni, E., Ozuni, E., Bijo, B., Shehu, F., Branciari, R., Miraglia, D., Ranucci, D. "Efficacy of non-thermal processing methods to prevent fish spoilage". *Journal of Aquatic Food Product and Technology*, 2021, 30, 228- 245.
- [10] Jørgensen, F., Sadler-Reeves, L., Shore, J., Aird, H., Elviss, N., Fox, A., Kaye, M., Willis, C., Amar, C., De Pinna, E., McLauchlin., J. "An assessment of the microbiological quality of lightly cooked food (including sous-vide) at the point of consumption in England". *Epidemiology and Infection*, 2017, 145, 1500- 1509.
- [11] Szczawińska M, E. "Application of Ionizing Radiation for Control of Salmonella in Food, In: Mihai Mares (Ed) *Current Topics in Salmonella and Salmonellosis*". IntechOpen, 2017.
- [12] Connell, J. J. "Methods of Assessing and Selecting for Quality. Control of Fish Quality". Fishing News Books, Oxford, 1990.
- [13] Hocaoglu, A., Sükrü, D. A., Gümüş, T., Demirci, M. "Effects of gamma irradiation on chemical, microbial quality and shelf life of shrimp". *Radiation Physics and Chemistry*, 2012, 81, 1923-1929.
- [14] Chouliara, I., Savvaidis, I. N., Riganakos, K., and Kontominas, M. G. "Shelf-life extension of vacuum-packaged sea bream (*Sparus aurata*) fillets by combined γ -irradiation and refrigeration: microbiological, chemical and sensory changes". *Journal of Science Food and Agriculture*, 2005, 85, 779- 784.

Water Management

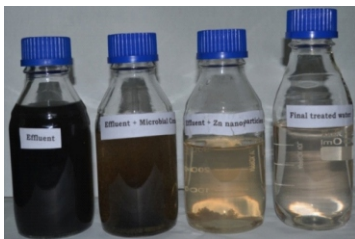
Development of an Effective Industrial Effluent Treatment System for Irrigation Purposes

Snehal Kale¹, Niranjana Ramgir^{2,3}, K.P. Muthe², A.K. Debnath^{2,3} and Sayaji Mehetre^{1,3*}

¹Nuclear Agriculture and Biotechnology Division, Bhabha Atomic Research Centre, Mumbai-400085, INDIA

²Technical Physics Division, Bhabha Atomic Research Centre, Mumbai-400085, INDIA

³Homi Bhabha National Institute, Anushaktinagar, Mumbai-400094, INDIA



Effluent waste water successively treated using three-stage treatment system

ABSTRACT

Industrial waste water presents significant challenge as regards its treatment and reuse for irrigation in terms of qualifying parameters like biological and chemical oxygen demands, respectively (BOD and COD). In order to make such effluent reusable for irrigation purpose, an efficient treatment system has been successfully designed, developed, tested, validated and deployed. Moreover this system offers a definitive value addition in terms of an enhanced nutrient content in the treated effluent. In particular, the system is capable of complete removal of colour, odour and impurities from the effluent. Besides, the BOD and COD levels were reduced to the extent of more than 94% within a week thereby making the effluent suitable reusable for agriculture purposes.

KEYWORDS: Industrial effluent treatment, Filtration system, Microbial treatment, Plant growth, Zinc nitrate nanoparticle

Introduction

Industrial effluent treatment has gained global significance and became a high priority as well as an incrementally challenging task of recent times. This is attributed to the relentless advances in industries fueled by the exponential population growth which have in consequence contributed to the enormous rise in effluent volume. Different technologies and/or methods are being employed to manage this mammoth effluent generated all over the globe according to Shah [1]. Generally, the effluents are sent to Common Effluent Treatment Plants (CETP) for treatment. This increases the process cost, transportation overheads and time of treatment. In order to address these issues and achieve decentralised waste management an in-situ treatment of waste water is desired which is quite pertinent to small industries. Such in-situ treatment plants will be the key step in the cost-effective management of the huge quantity of effluent. Besides, re-purposing the industrial effluent through bio-remediation and its reuse for different applications has also emerged as an attractive research avenue of particular significance considering the ever-depleting water resources which in the long term are anticipated to compromise the sustainability of industrial growth as well as general societal wellbeing as per Pandey and Jain [2]. Utilization of heavy metal resistant bacteria from industrial waste water is extensively practiced in the bio-remediation studies as they can withstand the highly polluted environment and simultaneously detoxify the effluent. Therefore, the selection of suitable bacterial consortium having ability to survive in the highly polluted environment, tolerate the high levels of heavy metal concentrations and simultaneously degrade the toxic components is very much essential. Based on these aspects, a novel and improved

integrated system has been developed and deployed. This system has brought a major reduction in the cost involved in transporting the water through pipes to and fro the CETP site. Besides, through the insightful use of zinc nitrate nanoparticles, it has also achieved the definitive value addition of the treated water in terms its nutrient enrichment namely zinc and nitrate content. The subsequent utilization of this nutrient enriched treated water has been fruitfully manifested for the healthy growth of plants.

Materials and Methods

Sample Collection from different Industrial Areas

Industrial effluent samples were collected from different industrial areas located in Maharashtra. All the standard procedures were followed during the sampling as well as analysis purpose. These samples were analyzed periodically for standard water quality parameters including pH, temperature, conductivity, total dissolved solids, TDS, total suspended solids (TSS), BOD, COD, alkalinity, chlorides, hardness and heavy metal content as reported by Kale and Bandela [3].

Primary Microbial Treatment

For bio-remediation of the waste water, selection of effective microbial consortium is a prerequisite. Effective bacteria were isolated from the same industrial effluent (*in situ*) and used for laboratory as well as field study. These bacteria were characterized for their ability to improve the water quality parameters as well as for their tolerance to different heavy metals and subsequently used as consortia for microbial treatment of the effluent.

Development of Filtration System

Filtration is an integral part of any effluent treatment

*Author for Correspondence: Sayaji Mehetre
E-mail: smehetre@barc.gov.in

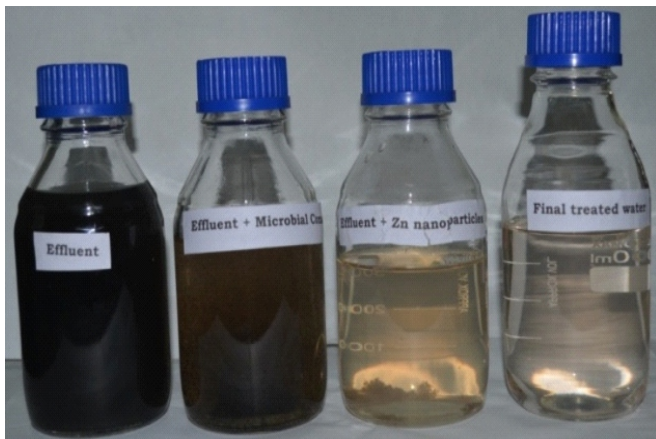


Fig.1: Effluent waste water treated successively using three-stage treatment system.



Fig.2: Pilot scale facility installed at BARC Training School Building, Anushaktinagar, Mumbai.

system. Conventional filtration systems are based on either sand or charcoal. In the present study, an improvised filtration system has been developed which comprises sand, charcoal, rice husk ash (waste product of rice processing industry) and resins (both cation and anion 1:1). All these materials were available locally and used for experimental purpose.

Secondary Treatment of Zinc Nitrate Nano Particles and Nanoparticle Characterization

Use of nanoparticles for water treatment has assumed a critical significance due to their reactivity and ability to reduce different pollutants. During the present study, zinc nitrate (zerovalent form @ 25 ppm) was used as a secondary treatment agent.

Pilot Study of Effluent Treatment Process

After benchmarking all the process parameters at laboratory scale, the system was successfully scaled up to treat 100 litre effluent per day under field condition. This

system has been deployed (using plastic drums and columns made from PVC pipes) at Training School Complex, Anushaktinagar, Mumbai. At the beginning, microbial treatment of industrial effluent was done by inoculation with consortia comprising 05 bacteria each @ 1×10^6 cells/ml in a plastic drum and subsequently aerated for 4 days. At the end of first stage, 90% water was transferred to next filtration stage with flow rate of 10 lit/h (in view of holding 10% microbial consortia for second cycle). Filtered water was collected in the plastic tank used for secondary treatment by nanoparticle solution (25 ppm) for 3 days. Post treated water after passing through muslin cloth was collected and tested for its BOD and COD level and used subsequently for irrigation purpose.

Effect of Post Treated Water on Growth of Crop Plants

Post treated water was tested in pot and microplots using Munbean and Spinach as test crop grown in duplicate. Both these plants were observed for their growth after treating with normal water (control) and treated one (post treated effluent water).

Results and Discussion

Sample Collection, Processing and Laboratory Studies on Effluent Treatment System

Based on the maximum threshold limit, colony characterization and growth behaviour, 05 bacteria were selected for microbial treatment. These bacteria include *Providencia stuartii*, *Klebsiella pneumonia*, *Alcaligenes spp.*, *Citrobacter spp.*, *Pseudomonas aeruginosa* as reported by Kale et al [4]. These bacteria survived in both acidic and basic pH conditions with optimum pH 7 and temperature 37°C, and also in salt concentration up to 10%. All the bacteria were found to secrete important enzymes like catalase, cellulose and amylase. These bacteria were mixed together to form consortium and used for treatment of effluent. After 3-4 days of microbial treatment, effluent was passed through filtration system followed by incubation with zinc nitrate nanoparticles which helped in further reduction of most of the water quality parameters. At last stage the effluent turned completely colourless (Fig.1) and all the water quality parameters were reduced to the levels as prescribed by regulatory agencies as per CPHEEO [5].

Pilot Scale Study on Effluent Treatment System Under Field Conditions

The industrial effluent brought from different industrial areas was tested in pilot plant of 100 L capacity per day (Fig. 2). All the water quality parameters were checked during entire experimental period. The effluent turned colourless and having all the water quality parameters well below the prescribed limits as set by pollution Control boards as per CPHEEO [5].

The developed system has successfully removed more than 94% COD, TDS and chlorides to acceptable limit.

Effect of Post Treated Water on the Growth of Crop Plants

Post-treated water was used as irrigation to Mung bean and Spinach plants grown in pots and micro plots. The treated water was found to be equally effective for growth of both the plants without any adverse effect on their growth (Fig. 3).

Industrial effluent treatment technologies are as old as the industries itself and are widely used by industries for treating effluent. CETP offers common platform for such technologies and thus widely accepted approach amongst all. In spite of availability of many technologies for treatment of effluent, there are incidences of not following proper disposal procedures by industries. The adoption of the available

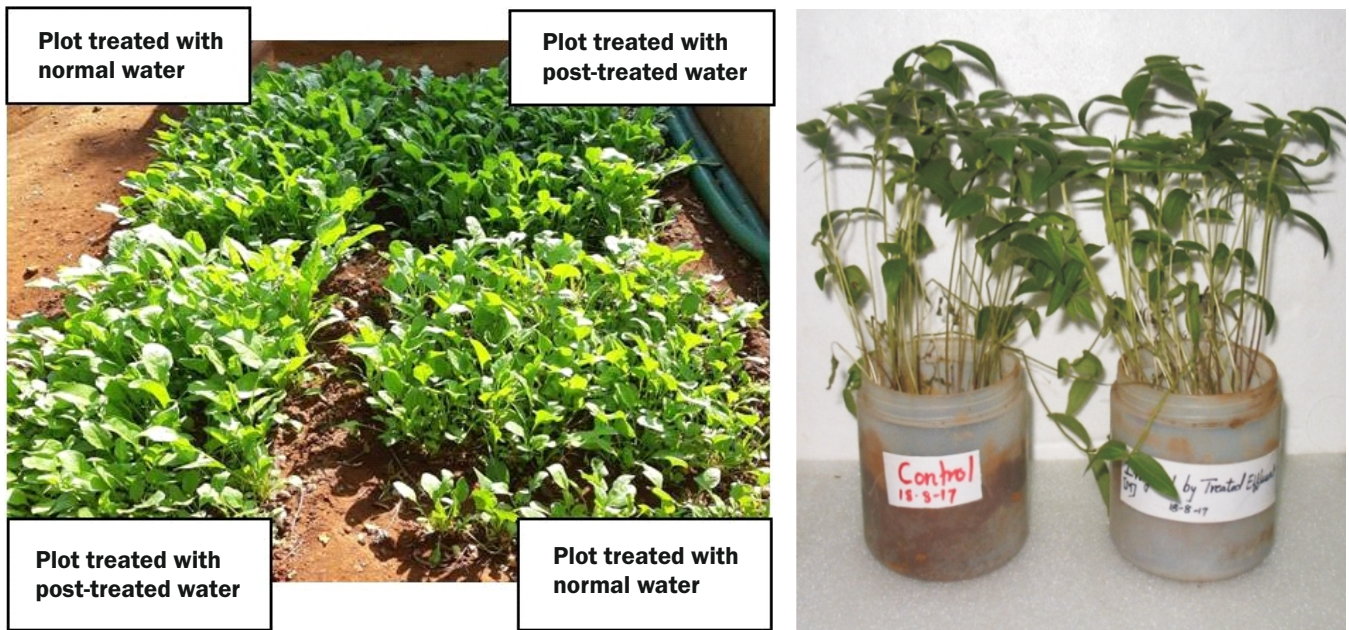


Fig.3: Effect of post-treated effluent water on the growth of Spinach and Mungbean.

technologies for treating the effluent is lacking either due to difficulties in implementation or in-efficiency of the technologies as reported by Padalkar and Rakesh Kumar [6]. In view of this, the system reported in the present study is highly efficient with a potential for deployment at higher scale. This system gainfully integrates the microbial, filtration and nanoparticle technologies in a coherent manner and thereby successfully reduces the toxic components of industrial effluent realizing thus a valuable nutrient enrichment of water for irrigation purpose. The key advantages of present system lie in its simplicity of design, economics, ease of operation, scalability and maintenance. Different components used during present study are available locally, inexpensive and furthermore possess the economically much desirable attribute namely the recyclability as and when called for.

Conclusion

Globally, industrial waste water treatment systems are facing enormous challenges due to water shortage and contamination of water resources. Due to this, there is a paradigm shift from waste water treatment to resource recovery and repurpose. In order to utilize the treated effluent for land applications, bringing the contaminants levels to the acceptable level is one part but it is also important to bring about the value addition in the post treated effluent in order to enhance its usability. Industrial waste water treatment system developed in the present study addresses both these important issues and makes water more suitable for irrigation purpose. Also, it offers the attractive possibility of in-situ processing of the waste water generated at source industry thereby is considered to be an important a major advance step towards achieving the goal of commercially attractive decentralized effluent treatment.

Thus, this three-stage effluent treatment system has served multiple roles in restoration of water quality, reduced water pollution and ensured a wholesome plant growth. Our studies clearly indicate that the industrial effluent waste water problems can gainfully be solved by this novel process. The present method represents new multi-faceted field deployable strategy towards securing a quality water supply for agricultural applications.

References

- [1] Shah M. P. "Industrial Wastewater Treatment: A Challenging Task in the Industrial Waste Management". *Advances Recycling and Waste Management*, 2016, 2, 115.
- [2] Pandey Gunjan, Jain Rakesh "Bacterial chemotaxis toward environmental pollutants: role in bioremediation". *Applied Environmental Microbiology*, 2002, 68, (12), 5789-95.
- [3] Kale Snehal D., Bandela N.N. "Study of Physico- Chemical Parameters of Waste Water Effluents from Waluj Industrial Area, Aurangabad". *Journal of Applicable Chemistry*, 2016, 5(6), 1 3 0 7 - 1314.
- [4] CPHEEO. "Manual on Sewerage and Sewage Treatment, Part A: Engineering Final Draft". Central Public Health and Environmental Engineering Organization, Ministry of Urban Development, New Delhi, 2012.
- [5] Kale Snehal, Bandela Narsingrao, Mehetre Sayaji. "Isolation, Screening and Characterization of heavy metal resistance bacteria for their potential use in Bioremediation of polluted water". *International Journal of Advance Research*, 2017, 5(12), 869-877.
- [6] Padalkar Ashwini V., Rakesh Kumar. "Common effluent treatment plant (CETP): Reliability analysis and performance evaluation". *Water Science and Engineering*, 2018, 11(3), 205-213.

Hot Cell Applications

Development and Installation of Remotely Operated Telescopic Camera System to View Pouring and Handling Operations

Rahul Tripathi^{1*}, B.N. Bhagyawant¹, S.R. Shendge¹, A.K. Gangyan¹, Jyoti Diwan¹, Sumnesh Wadhwa¹ and C.P. Kaushik^{2,3#}

¹Waste Management Division, Bhabha Atomic Research Centre, Mumbai-400085, INDIA

²Nuclear Recycle Group, Bhabha Atomic Research Centre, Mumbai-400085, INDIA

³Homi Bhabha National Institute, Anushaktinagar, Mumbai 400094, INDIA



Camera replacement underway in maintenance area

ABSTRACT

Indian Nuclear Power Programme has adopted a 'Closed Fuel Cycle' which involves reprocessing & recycling of Spent Nuclear Fuel and other wastes coming from nuclear reactors. This process involves use of special facilities, such as a 'Hot Cell', which is inaccessible to personnel due to the presence of high radiation levels. Any operation inside this cell is carried out in a remote manner by viewing through a Radiation Shielding Window (RSW) or a CCTV camera system. Exposure to high radiation fields causes browning of lenses and failure of camera electronics. To overcome this, a Telescopic Camera Assembly was designed & developed and subsequently installed inside the cell. This assembly includes a motorized rotating assembly for in-plane rotation and a motorized hoist assembly for vertical movement of CCTV camera pan-tilt assembly. This camera assembly will be exposed to radiation environment only during remote handling or vitrification operations in the Melter cell. This design minimizes radiation exposure by ensuring that the assembly will be rotated back into a lesser radioactive area (where fields are in mR) during the idle condition of the cell. This reduction in radiation exposure will ultimately enhance the life span, thus lowering the frequency of replacement of the camera assembly. Currently the system is being utilized in a campaign of vitrification operation of Waste Immobilization Plant (WIP), Trombay and is performing exceptionally well.

KEYWORDS: Hot cell, Melter cell, Remote viewing, Telescopic assembly, Vitrification, Planetary gearbox, CCTV camera

Introduction

Waste Immobilization Plant (WIP), Trombay, BARC [1] has been established with the mandate of liquid waste management generated by the Reprocessing Plant, which reprocesses the spent fuel discharged from Research Reactors. All remote handling gadgets inside the Hot Cell are operated by viewing through Radiation Shielding Window (RSW) or CCTV camera assisted monitors. A Telescopic Camera System was designed at WIP to view Melter cell operations. This motorized rotating telescopic assembly was primarily designed to view pouring operations and other remote handling activities inside the Melter cell. It was designed with two Degrees of Freedom (DOF) i.e. in-plane rotation (with fixed radius (r) & variable angle (θ) (i.e. polar motion) and vertical motion (tube-in-tube type motion in z direction). Additionally, a pan-tilt assembly (with two DOF) is also installed on the last tube, which holds a CCTV camera with connector assembly. This assembly has been installed on the partition wall between melter cell and maintenance area. Remote operations inside the cell using a commercially available camera is difficult because Charge

Coupled Devices (CCD) have limited radiation life. Exposure to high radiation fields causes browning of optics and failure of camera electronics including the CCD sensors. This limited life, has necessitated limited exposure of the CCTV camera system to high radiation fields. This issue was solved by rotating the camera assembly after use, towards the maintenance area (where radiation field is mini scale in comparison to the melter cell). The melter cell operations can be viewed as and when required by rotating the camera assembly towards the melter cell using in-plane rotation through a wall cut out of $2\text{m} \times 1.5\text{m}$. A schematic, showing the melter cell with telescope camera assembly has been shown in the Fig.1.

Design Philosophy

Special Features

This assembly was designed with several special design features which are listed below

- 1) Material of Construction to suit the Hot Cell environment.
- 2) Remotely operable from outside the cell by viewing through RSW and mounted on the partition wall between melter cell and Parking Area of Vitrification Bay.
- 3) Specially designed in-planeplanetary gearbox with inbuilt

*Author for Correspondence: Rahul Tripathi
E-mail: rtripathi@barc.gov.in



Fig.1: 3-D model of Melter Cell showing installation location of telescopic camera.

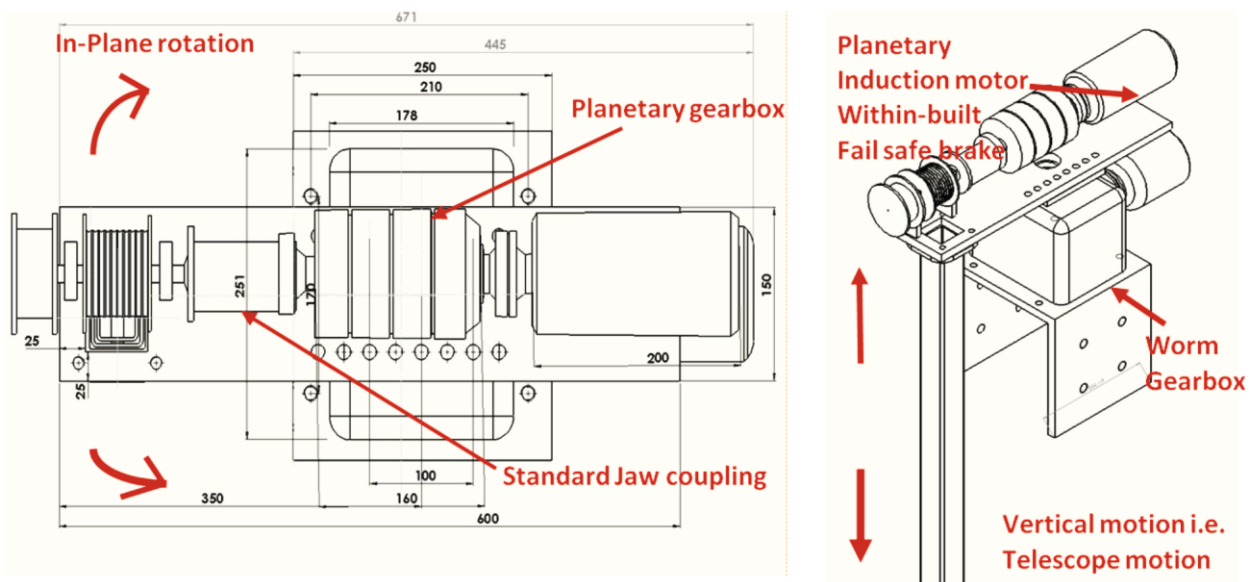


Fig.2: Telescope camera model with motions and major component.

AC Electromagnetic (ACEM) brake for vertical motion.

- 4) Telescopic vertical movement with adequate guiding supports and installation of limit switches to constrain all motion within required limits.
- 5) Specially designed vertical cable take up system to prevent cable entanglement.
- 6) Modular design and ease in replacement of cameras.
- 7) Material of Construction - Due to the highly radioactive & corrosive atmosphere within the cell, all structural & moving parts (sliding and rolling contacts) such as telescopic tubes, base plate, wire rope & rope drum are made of suitable grade of stainless steel (SS304). However, all gearbox units are housed in sealed enclosures to provide protection from contamination and corrosive environment.

Working Operation

The telescope consists of three tubes providing telescopic boom length of 4700mm and the collapsible length of 1700m. Tube size, limit switch and stopper location etc. are optimized

in such a way to achieve the complete range of motion, as stated above. Camera with pan-tilt assembly is mounted on the bottom square tube for viewing purpose. Simultaneous operation of polar motion at different values of angle can enable it to reach to any position. All motions of the camera assembly have been shown in the Fig.2.

Design Methodology

The system has been installed inside the Melter cell which is already in operation and has a high radioactive field. Additionally, it has been mounted on partition wall where it has to travel through a wall cut out of 2m × 1.5m. This has been considered for calculation of collapsible length.

The size of whole system was optimized in a way so that exiting crane and girder mounted servo manipulator can freely travel through the cut out and should have sufficient clearance between telescope system and girder of existing crane and servo manipulator assembly. Mounting location on the partition wall has been shown in Fig.3. For complete viewing of the Melter cell this assembly is designed with four motions which are described as below.

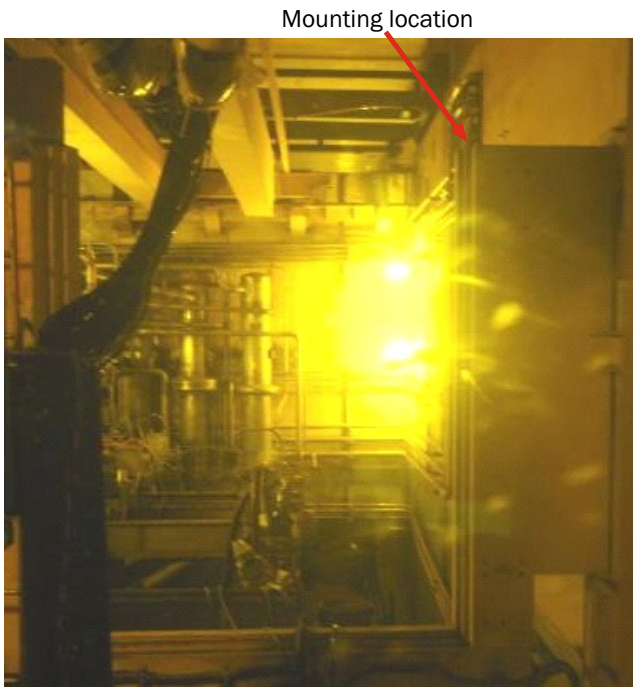


Fig.3: Mounting location inside the cell.

S.No.	Motion	Mechanism	
1.	In-plane rotation (with fixed radius (r) & variable angle (θ) polar motion)	Using Standard worm gearbox	200° (±100°) travel at 270mm radius
2.	Vertical (Telescopic motion)	Using customized In-planetary gearbox with flexible wire rope assembly	1.7m to 4.7m
3.	Pan & Tilt Motions	Standard pan-tilt Assembly	Pan=±180° & Rotation Tilt=±90

Telescopic Motion

Three square tubes of different sizes (were used for telescopic movement, where upper tube was fixed to upper rotating part as shown in the Fig.2 and lowest tube was tied to wire rope. Additionally, other arrangements were provided for precise linear motion in vertical direction and to avoid any unintentional rotation. Two turns will always be on the rope drum at maximum extension of the tubes. Minimum Length of wire rope required = extended length of tubes + distance between topmost tube and pulley + no. of turns on rope drum × circumference of rope drum = 5.17m

Minimum breaking load of wire rope as per IS 3177 (1999) = $S \times Z_p \times C_{df} = 10KN$; where S = Maximum rope tension, Z_p = Minimum practical coefficient of utilization, C_{df} = duty factor. SS304 wire rope having 4mm dia. with 6 x 19 construction has been selected with minimum breaking load of 38 KN.

Crushing Stress on Rope Drum =

$$\frac{\text{Total mass on rope drum including camera structure}}{\text{pitch} \times \text{thickness below the groove of rope drum}} \approx 340Kg/cm^2$$

For bending stress, it is assumed that the entire wire load would act on the center of rope drum. This would result in safer design. The rope drum is supported on two bearings at a distance of 60 mm. The bearings are symmetrically placed with respect to center line of rope drum.

Maximum Bending Moment on Rope Drum =

$$\frac{\text{load} \times \text{distance between bearing}}{4}$$

Calculated Bending Stress on the Rope Drum ≈ 75kg/cm²

Total stress generated on the rope drum ≈ 412 kg/cm²

Allowable Stresses on the rope drum as per IS3177

$$= \frac{\text{Ultimate stress of the material}}{C_{df} \times C_{bf} \times C_{sf}}$$

C_{df} = Duty factor, C_{bf} = Basic stress factor, C_{sf} = Safety factor

Allowable stresses = 1000Kg/cm² total stress generated on the rope drum, Hence design of rope drum was safe.

Planetary Gearbox

A specialized foot mounted in-plane planetary gear box has been designed and fabricated with four stage reduction for this assembly to overcome space restraints. This gearbox has been designed primarily on the basis of two requirement which are listed as follows:-

1. Torque (≈ 140kg-m)
2. High speed reduction (1:480) to achieve very low speeds

High torque was achieved in four stages using high grade material and spline shaped shafts instead of the usual key shapes. In every stage one sun gear was meshing with three planet gears mounted on the planet carrier which further meshes with another sun gear maintaining the same direction of rotation and this planet carrier will be connected to the output shaft of the gear unit. In the place of keys, splines in all shafts have been used so that high torque can be transmitted.

The Motor was designed as per IS 3177: 1999 as per following expression.

$$\text{Minimum hoisting kW required} = \frac{M \times V \times C_{df} \times C_v}{6.12E \times C_{amb}} = 131.55 \text{ Watt}$$

Hence 0.25 HP of motor was selected.

Where:

M = Mass of the rated load and the wire rope in tonnes

V = hoisting speed in m/min

E = Combined efficiency of gears and sheaves

Where n = no. of gear pairs and m= total no. of rotating sheaves

C_v = Service factor, C_{df} = Duty factor, C_{amb} = Derating factor

Needle bearings have been selected for planet gears while deep groove ball bearings have been used to drive shafts. Enclosed Gears and shafts are made from EN 8 and EN 9 respectively. Four stages of planetary gearbox (speed reduction ratio of 1:480) with 0.25HP customized three phase brake induction motor (with totally enclosed fan cooling and IP55 protection) have been used for achieving low speeds of 3m/minute. Standard Jaw coupling has been used for transmission of rotation motion from the motor to rope drum assembly.

In-plane Rotation

Worm gearbox belongs to the cross axis drives where a very high reduction ratio can be realized in one single stage.

Customized worm gearbox was used to achieve very high-speed reduction for in- plane rotation (speed of 1rpm). This gearbox was powered using 0.5HP three phase brake induction motor (with totally enclosed fan cooling and IP55protection).

Fail safe Brakes

Fail safe brakes have been used in all motions. The brakes are designed to exert a restraining torque of minimum 50% greater than the maximum torque transmitted to the brake from the suspended load as follows:

Torque transmitted to brake =

$$\frac{\text{Pitch circle trdia of rope drum} \times \text{suspended load}}{4 \times \text{speed reduction ratio}}$$

CCTV Camera Assembly

The camera system consists of a CCTV camera, control cable, monitoring device (CCTV Monitor) and recording device (VCR/DVR). The camera has been installed on a pan-tilt assembly. This camera and monitoring device are connected through a 40m long multi-core composite cable. This cable carries video signal and other electronic signals. It is a combination of different types of specialized cables such as coaxial cables and low voltage carrying cables bundled in a singles pool. The camera control unit gives two video outputs; one for connection to monitor for display of images captured by camera, and, the other for recording. Standard Digital Video Recorder (DVR) is being used here for recording purpose.

Safety Features

In all motions after limit switches have been provided and during failure of these limit switches, mechanical stoppers have been used to avoid any unwanted accident and after reaching this position, control panel of an electric motor will get tripped. In this way, full assembly will be safe from accidental point of view. In failure of any component, this system can be lifted using existing in-cell crane of Melter cell without any manual intervention and can be shifted in maintenance area.

Challenges during Fabrication and Installation

Hook Arrangement

The hook was remotely installed inside the cell on the partition wall using an in-cell crane. As per design the in-plane motor was placed on the south side (on one side of the assembly) and the other motor assembly was placed towards the east direction (installed on worm gearbox). It was a challenging task to calculate the centre of gravity of the assembly and was found to be in the south-east direction. These factors were considered in the design of the hook (using 10mm diameter of rod). Also, the lifting eye was also located eccentrically (south-east direction).

Vertical Cable take up Assembly

The Vertical Cable Take-up Assembly was a design challenge as it had to prevent cable entanglement. Here cables (of 700mm length) in a single spool were fixed & mounted on the first telescopic tube (i.e. first stage). A Flexible cable drag chain (of 1.6m length) was used for extension/opening of second tube. Cables were routed and mounted on cable tray for extension of the third telescopic tube (i.e. last stage).

Location of Limit Switches

The entire telescopic assembly was retrofitted in an existing Hot Cell environment, with several pre-existing path obstructions. Hence, two limit switches were located in the plane of rotation to restrict movement towards the melter cell

and parking area. Two limit switches were also installed in vertical direction for extreme up & down locations. Location of vertical limit switches were selected to enable the following functions.

1. Optimal view of pouring and other remote handling operations
2. When not in use, the assembly will be rotated back through partition wall cut-out (of 2m depth), for parking in the maintenance area. The upper limit switches are located to accommodate the telescope in a desired collapsible condition. Locations of all limit switches were decided after taking into consideration the feedback of the operator.

Installation and Commissioning of Telescopic Camera System inside the Cell

Pre-installation Challenges

Prior to installation of this system, it was imperative to know the condition of the melter cell with respect to its background radiation & contamination level. Thus, a radiation survey was carried out and a few radiation hot spots were identified.

To overcome these hotspots, the existing portable shielding was modified, fabricated and installed at the installation site (i.e. partition wall) to avoid any radiation streaming to the working area.

Installation and Commissioning of Telescopic Assembly

Installation of assembly was carried out, subsequent to the radiation survey and decontamination. Installation work was categorized in the following stages.

1. External/Outcell testing of assembly for readiness.



Fig.4: Camera installed on last tube of assembly.

Limit switch details: Plunger type limit switches with metallic rollers were used.

Make	Siemens
Operating Force	20N (max.)
Limit Switch Actuator	Plunger type
Degree of protection	IP65
Contact Voltage AC	230VAC

2. Modification in local portable shielding to reduce radiation background.
3. Shifting & Insertion of telescopic assembly inside the cell.
4. Installation of assembly on partition wall using existing in-cell crane.
5. Cable routing inside the parking area of HL bay.
6. Installation of control panel in operating area.
7. Remote operation of this assembly from a control panel (i.e. operating area).

Cable Routing

Cable routing (18m cabling) of this assembly was carried out inside the highly radioactive and contaminated environment of the cell. Hot cell cable routing was categorized in the following steps.

1. Cables (in PVC enclosure) were shifted inside the cell with Assembly.
2. Vertical routing of cables (for camera, pan-tilt assembly & bottom limit switch) on telescopic tubes using cable tray and cable drag chain.
3. Subsequent routing and mounting of all cables on the wall.
4. Removal of cables outside the cell through embedded plug and specially designed lead shielded plug (which was being used to avoid radiation streaming).

Commissioning

The Telescopic Based Camera System was subjected to rigorous testing by repeated remote operations from outside the cell, by viewing through RSW and CCTV camera monitors. All parameters for vertical motion and in-plan motion (including limit switches actuation etc.) were thoroughly checked. Subsequent to complete testing and commissioning activities, this assembly is currently being utilized in the ongoing campaign of vitrification operations.

Critical Operations Accomplished by Telescopic Based Camera System

The Telescopic based Camera System has been utilized for ten pouring campaigns where five no. of VWP canisters and one batch of vitrified product for Cesium pencil have been completed. Earlier, each camera life cycle was limited to a



Fig.5: Shifting and insertion of assembly inside the cell.

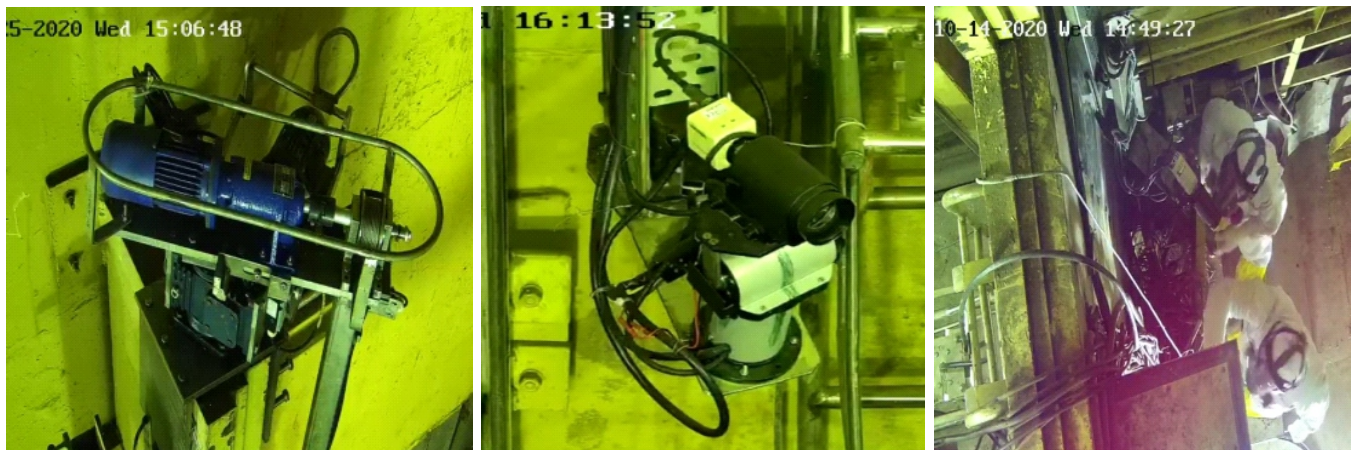


Fig.6: Telescope camera assembly inside the Melter cell.

single campaign. Other auxiliary operations such as weighing and several material handling activities were also completed using this system.

Conclusion

This system is nearing completion of almost 4 years of operating in a Hot Cell without any maintenance and high operational performance. It has been designed to enhance the life span of the conventional camera by taking into account several operational feedback and requirements of plant personnel involved in day to day operations of the Melter cell in the Vitrification bay of WIP, Trombay. This system has effectively increased efficiency of the camera life cycle by seven times. It has thus achieved several important targets of WIP, Trombay, by reducing man-rem exposure, giving cost benefits, lowered system down time by decreased frequency of change in cameras, and reduced disposal quantities of malfunctioned cameras thus decreasing radioactive waste.

Acknowledgements

Authors are extremely grateful to Director, Nuclear Recycle Group, for valuable support and motivation for entire work. The authors are also thankful to all staff of the Waste Immobilisation Plant at BARC Trombay for helping through out the development and installation of this assembly.

#Dr. C.P. Kaushik, Formerly Director of Nuclear Recycle Group, retired from service in February 2022.

References

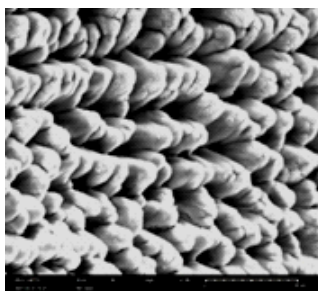
- [1] C.P. Kaushik, "Indian Program for Vitrification of High Level Radioactive Liquid Waste", Procedia Materials Science, 2014.
- [2] Waste Immobilization Plant, Safety Report and Technical Specification, 2011.
- [3] Waste Immobilization Plant, Remote Handling Standard Operating Procedure, 2011.
- [4] Standard Specification for heat resisting Cr and Cr-Ni Stainless steel plate, sheet & strip for pressure vessels and general applications, ASTM A-240, 2012.
- [5] Code of Practice for Electric Overhead Travelling Cranes and Gantry Cranes other than Steel Work Cranes [MED 14: Cranes, Lifting Chains and Related Equipment], IS 3177, 1999.
- [6] Design, erection and testing (structural portion) of cranes and hoists-Code of practice [MED 14: Cranes, Lifting Chains and Related Equipment], IS 807, 2006.
- [7] Three-phase induction motors [ETD15: Rotating Machinery], IS 325, 1996.
- [8] Mechanical Engineering Design Book, Richard G. Budynas and J. Keith Nisbett, Ninth Edition, 2011.

Improved Osseointegration

Influence of Picosecond Laser Induced Topographical Modification on *in-vitro* Osseointegration of Ti6Al4V Bio-alloy

Sunita Kedia* and J. Padma Nilaya

Laser and Plasma Technology Division, Beam Technology Development Group,
Bhabha Atomic Research Centre, Mumbai-400085, INDIA



Picosecond laser induced cones on Ti6Al4V bio-alloy

ABSTRACT

With increase in the demand for artificial body implants, efforts expended towards overcoming implant failure have also increased. Laser assisted surface micro structuring of biomaterials is known to increase their biofunctionality. This work is aimed to qualify the best suitable microstructure among six unique patterns generated on Ti6Al4V bio-alloy by employing a 30ps pulsed laser. Time dependent *in vitro* osseointegration was evaluated from the rate and quality of hydroxyapatite (HA) growth on the samples. The SEM and EDS analysis confirmed good quality of HA and micro-Raman analysis revealed ~4.6 fold enhancement in the growth of HA on one of the laser treated sample in comparison to pristine sample.

KEYWORDS: Osseointegration, Picosecond laser surface modification, Micro structuring, Cell and protein adhesion, HAP growth

Introduction

Equipped with unique combination of high strength and low density, grade-5 titanium alloy (Ti6Al4V) has been considered a suitable biomaterial for dental and orthopedic implants applications [1]. In spite of excellent biocompatibility and corrosion resistance, this material exhibits fatigue failure due to poor osseointegration in the body [2]. The osseointegration is a complex process [3] that begins with the growth of hydroxyapatite (HA: $\text{Ca}_{10}(\text{OH})_2(\text{PO}_4)_6$), a bone like material, on the surface of artificial implant that joins the implant to the body tissues. During interaction with blood plasma, dissociation of H_2O on the surface of implant leads to the formation of OH ions that subsequently stimulate absorption of Ca^{2+} ions and promote nucleation of HA. A mature HA layer is basically calcium orthophosphate salt with a Ca/P molar ratio about ~1.677 [4]. Growth of HA and further osseointegration is greatly influenced by the surface properties of the implant and hence suitable modification of the surface of an implant is a proven method to improve its biofunctionality.

Among various techniques such as texturing, coating, alloying, and oxidation, the laser surface texturing is attracting the attention of researchers for achieving the desired surface modification of biomaterials. This is because, laser assisted surface texturing is an easy and contamination free process involving minimum steps and can be achieved remotely [5]. The three factors that play a significant role here are the laser parameters, the substrate material properties and the experimental conditions. For a given material, change in laser power, wavelength, pulse duration and irradiation time can result in substantial topographical variation on the sample surface [6-7]. While absorption by the surface depends on its

roughness and the wavelength of the incident radiation, the rise in temperature depends also on the laser pulse duration, repetition rate and fluence. Menciet et al. reported effect of laser wavelength and pulse duration on the surface structure of β Ti-alloy [6]. Morales et al. discussed effect of change in laser fluence and irradiation time on surface structure of Ti6Al4V sample [7].

In this work, a picosecond pulsed Nd-YAG laser operating on 532 nm at 10Hz repetition rate was employed to irradiate the surface of Ti alloy biomaterial. The laser power and sample scan speeds (along x and y directions) were varied. Surface melting coupled with varying extent of overlap of successive pulses resulted in the generation of several unique patterns on Ti6Al4V bio-alloy. Of the many patterns thus generated, six unique ones with distinctly different microstructures were chosen for *in vitro* testing of HA growth. Laser textured and pristine samples were immersed in simulated body fluid (SBF) for 24 hrs, and the laser treated sample with maximum number of nucleation sites of HA as revealed by scanning electron microscope (SEM) image was chosen for further studies. The change in wettability of the samples was studied by water contact angle (WCA) measurement. Energy dispersive X-ray spectroscopy (EDS) and micro-Raman analysis were used to confirm growth of HA on the samples. The results revealed a significant improvement of about 4.6 folds in the growth of HA on laser treated sample in comparison to pristine sample.

Material and Methods

Ti6Al4V bio-alloy sheets (~1mm in thickness) were procured commercially and cut into square pieces of ~10 mm x 10 mm and were mechanically polished using 180, 400 and 800 grit papers in that sequence and ultrasonicated in acetone, ethanol and water in that order for 10 min.

*Author for Correspondence: Sunita Kedia
E-mail: skedia@barc.gov.in

Table 1. Samples and experimental parameters

Sample	Laser power (mW)	Scan speed ($\mu\text{m}/\text{sec}$)	Overlapping (μm)
S1	2	2.5	100
S2	10	2.5	20
S3	10	2.5	80
S4	10	10	20
S5	20	5	50
S6	20	50	50

For laser surface modification experiments, the second harmonic emission from a picosecond Nd:YAG laser (Model # N311, Ekspla make) with 30 ps pulse duration and 10 Hz pulse repetition rate was focused on to the surface of the sample with a 10 cm focal length lens and the focal spot was $\sim 30 \mu\text{m}$. Different combinations of laser power, sample scan speed and lateral overlapping were tried to generate a variety of microstructures on Ti6Al4V sample surface. Experimental parameters of six samples that were chosen based on their significantly different surface patterns are listed in Table-1. Topographical modification of the samples was studied using SEM (M/s. SEC Co.). For wettability, about 1 μL water drop was put on the sample using a computer controlled micro-syringe and photo of the drop was recorded for WCA estimation using an inbuilt CCD camera.

Table 2. Amount of reagents in the order they were used in the preparation of SBF

Order	Reagent	Amount in gm/L
1	NaCl	6.547
2	KCl	0.373
3	NaHCO_3	2.268
4	$\text{Na}_2\text{HPO}_4 \cdot 2\text{H}_2\text{O}$	0.178
5	$\text{MgCl}_2 \cdot 6\text{H}_2\text{O}$	0.305
6	$\text{CaCl}_2 \cdot 2\text{H}_2\text{O}$	0.368
7	Na_2SO_4	0.071
8	$\text{CNH}_3(\text{CH}_2\text{OH})_3$	6.057

To study *in vitro* osseointegration, pristine and laser treated samples were immersed in SBF which was prepared in-house by following a standard protocol [8]. To prepare 1 L of SBF, the reagents listed in Table-2 were dissolved in the mixture of de-ionized water (950 ml) and 1 M HCl (50 ml) on a magnetic stirrer. The pH of the fluid was maintained at 7.4 and each sample was immersed separately in 50 ml of SBF for 24 hrs and maintained at 37°C. The growth of HA on sample surface was analyzed using SEM, EDS and micro-Raman spectroscopy.

Results & Discussion

Fig. 1a and 1b are the SEM and WCA of pristine Ti6Al4V sample. Rough surface and hydrophilic nature with WCA of 68° were observed for this sample.

Laser surface treatment

Figs. 2a and 2b show SEM images of laser treated samples (S1 - S6) at two different scale bars of 30 μm and 5 μm . The laser treated area can be seen to contain micron size features covered with nanostructures, such hierarchy structures being very important for superior osseointegration, cell adhesion and bacterial inhibition [9-11]. The samples are significantly different from each other in sub-micron level and this is clearly visible in the magnified images. The WCA of laser treated samples increased in comparison to WCA of pristine

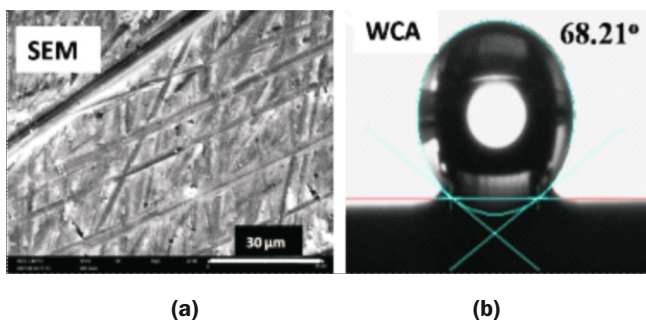


Fig.1: (a) SEM image and (b) WCA of pristine Ti6Al4V sample.

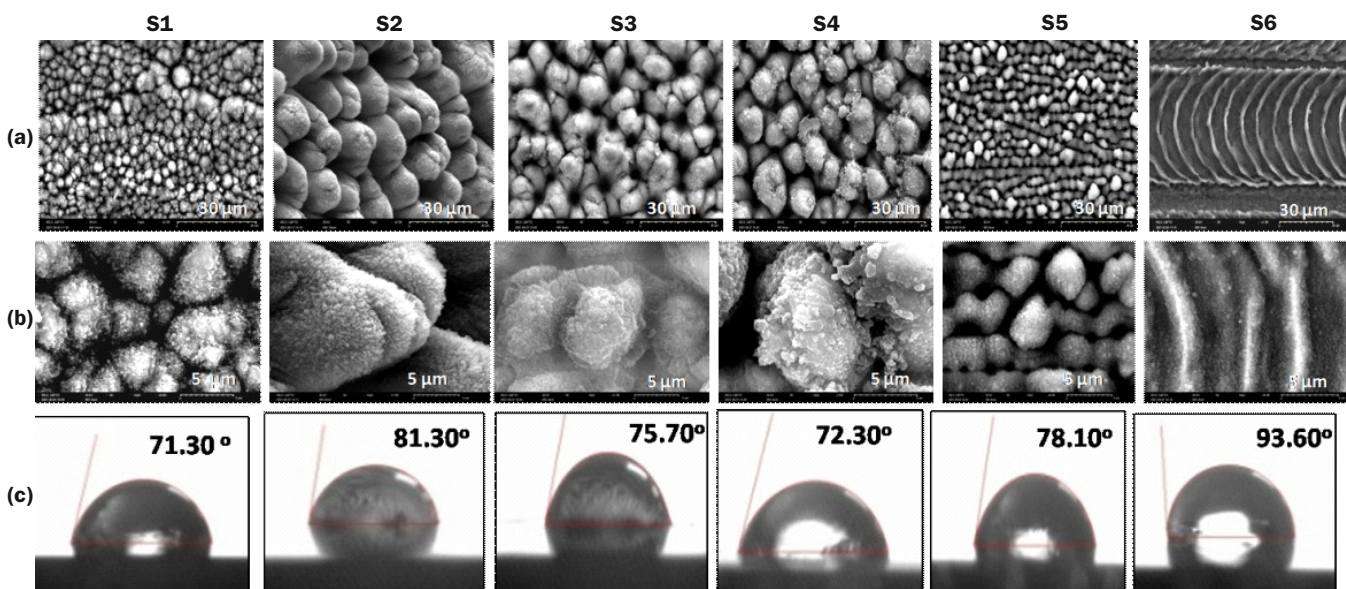


Fig.2: SEM images of laser treated samples at scale bar of (a) 30 μm and (b) 5 μm and (c) WCA of laser treated samples.

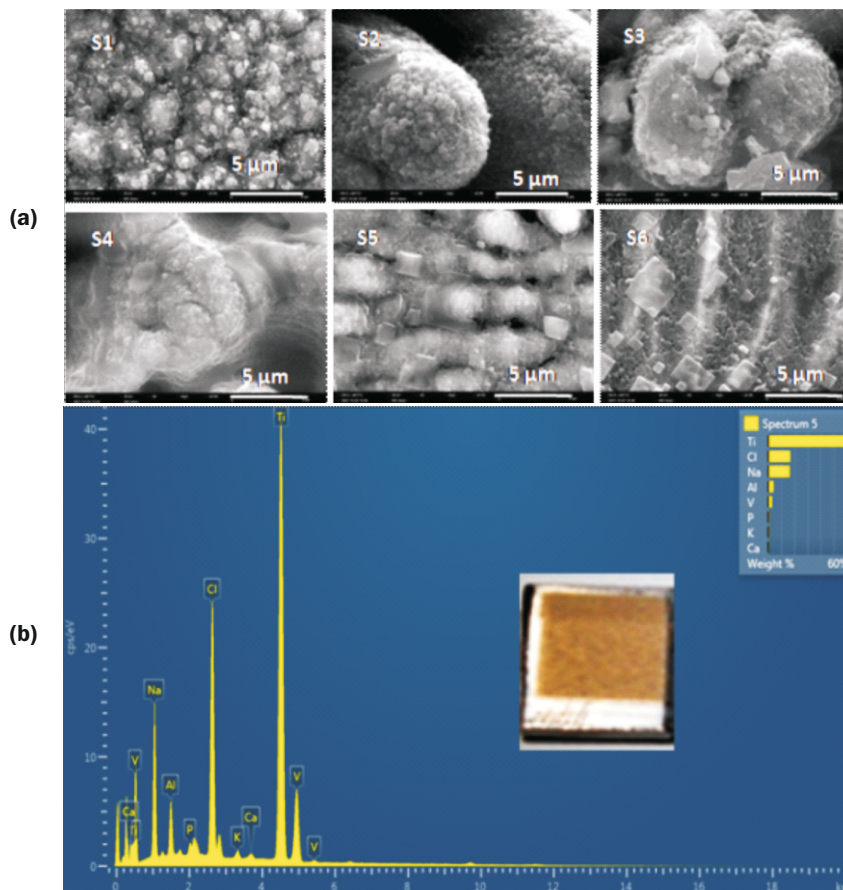


Fig.3: (a) SEM image of laser treated samples and (b) EDS of S6 sample after immersion in SBF for 24 hrs; inset is a photograph of S6 sample in which the golden part is laser treated region.

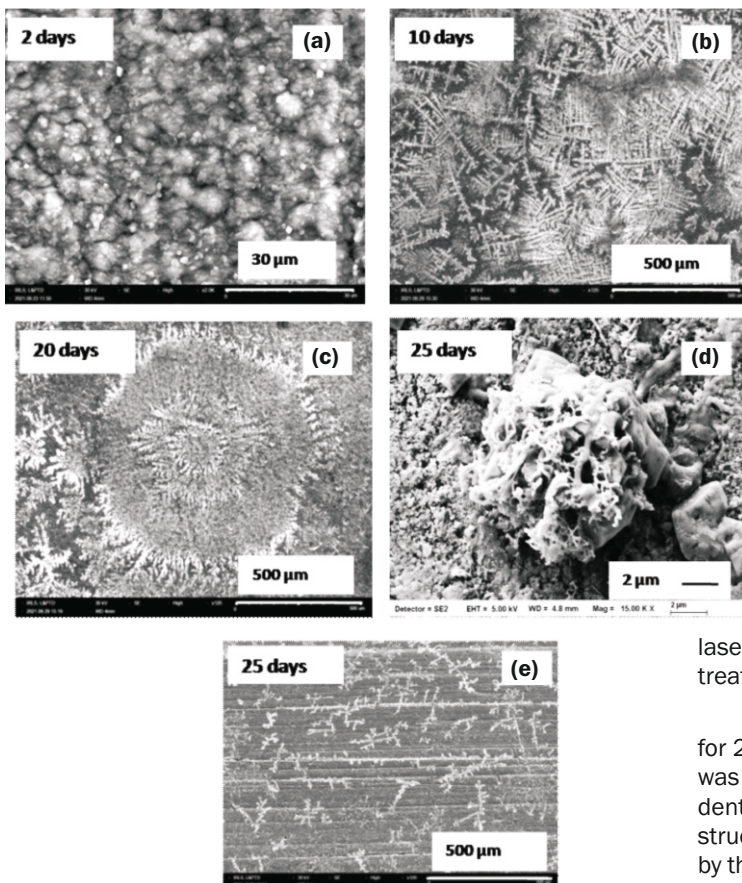


Fig.4: SEM image of S6 sample immersed in SBF for (a) 2 days, (b) 10 days, (c) 20 days, (d) 25 days and (e) Pristine sample immersed in SBF for 25 days.

Ti6Al4V and sample S6 showed hydrophobic nature. The decreased wettability is due to air that gets locked in the pockets of microstructures on laser treated samples that, in turn, restricts spreading of water on the surface of the sample.

Fig. 3(a) shows the SEM images of laser treated samples immersed in SBF for 24 hrs. Deposition of crystalline structures was observed on the surface of all samples. The EDS analysis of S6 sample shown in Fig. 3b revealed that the crystals were rich in sodium and chlorine; however calcium and phosphorus were also traced in small amount. Presence of Ca and P on the sample indicated initiation of osseointegration within 24 hrs. Density of the crystals and hence, the nucleation sites for growth of HA were highest on S6 sample as seen from SEM images and therefore, S6 was chosen for further study of day dependent growth of HA. For this, about four samples of S6 were made and immersed separately in SBF for pre-decided number of days viz., 2, 10, 20, and 25 days. Inset of Fig. 3b shows a photograph of S6 sample where golden region is the laser treated area. Growth of HA was compared on laser treated and untreated area for all cases.

Fig. 4a-4d shows the SEM images of S6 immersed in SBF for 2, 10, 20 and 25 days, respectively. Crystalline deposition was observed after 2 days and the morphology changed to long dendrite structures on the sample after 10 days. With time, the structure enlarged and took shape of concentric flowery circles by the end of 20 days (Fig. 4c). The Ca/P ratio of the structure was between 1.18 - 1.35 on this sample. After 25 days, spherical agglomerations were observed on surface of S6 sample (Fig. 4d) while HA growth in the form of linear structures was seen on the surface of pristine sample (Fig. 4e).

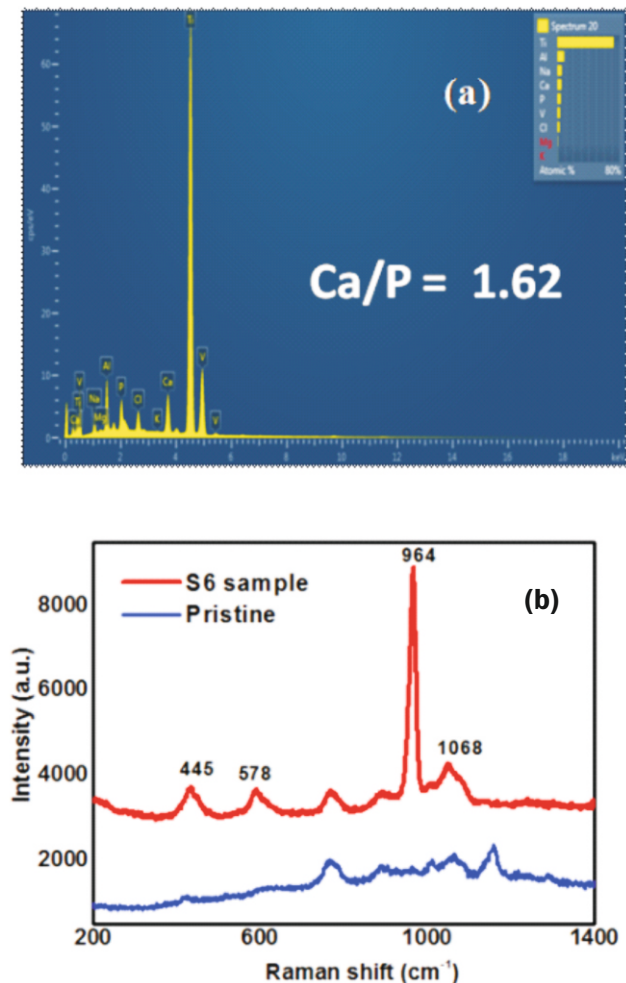


Fig.5: (a) EDS of HA grew on S6 sample and (b) Raman spectrum of HA grew on pristine and S6 sample after 25 days immersion in SBF.

Fig. 5a shows EDS analysis of HA grew on S6 sample after 25 days of immersion in SBF. The Ca/P ratio was found to be 1.62 which is close to the Ca/P ratio of matured HA [4]. For the same time interval the Ca/P on the pristine sample was about 1.22. This indicated the quality of HA grew on S6 sample was superior to HA on pristine sample. Fig 5b shows the Raman spectrum of HA on pristine and S6 samples after immersion in SBF for 25 days. The strongest peak at 964 cm^{-1} is attributed to the symmetric stretching mode of PO_4 tetrahedron and this is the characteristic peak of HA. The second peak at 1068 cm^{-1} can be assigned to the stretching vibration mode of CO_3^{2-} bond [12]. A significant improvement of ~ 4.6 fold in the intensity of characteristic peak of HA on S6 sample indicated faster and superior growth [12], that in turn, points to superior osseointegration. This can be attributed to the generated micro-nano structures on the surface of Ti6Al4V post laser treatment that increase the surface area, create nano voids, resulting in an increased interaction of the sample with body fluid.

Conclusions

A wide variety of micro-nano structures were generated on the surface of Ti6Al4V bio-alloy by controlling two experimental parameters viz., laser power and sample scan speed. The samples exhibited significant changes in the microstructure as revealed by SEM images and wettability as indicated by WCA measurements. More number of nucleation sites were observed on one of the laser treated sample (S6) within 24 hrs of immersion in SBF and ~ 4.6 fold improvement in the growth of HA was observed after 25 days as compared to the pristine

sample. Thus the study indicates that laser surface treatment, for judiciously chosen laser parameters, is a viable method for improving the osseointegration of biomaterials in human body.

Acknowledgement

The authors gratefully acknowledge the constant support and guidance of Group Director, BTDG and Head, L&PTD. They also acknowledge A.K. Sahu, G&AMD for EDS facility, Puspa Gaikwad for technical help.

References

- [1] D. Li, J. Zou, R. Xie, Z. Wang and B. Tang. Surface texture-Based surface treatments on Ti6Al4V titanium alloys for tribological and biological applications: A mini review. *Materials*, 2018, 487, 11, 1-28. <https://doi.org/10.3390/ma11040487>.
- [2] C. W. Lin, C. P. Ju, J. H. C. Lin. A comparison of the fatigue behavior of cast Ti-7.5Mo with c.p. titanium, Ti-6Al-4V and Ti-13Nb-13Zr alloys. *Biomaterials*, 2005, 26, 2899-2907. <http://doi.org/10.1016/j.biomaterials.2004.09.007>.
- [3] P. Vaidya, S. Mahale, S. Kale and A. Patil. Osseointegration-A review. *IOSR-JDMS*, 2017, 16, 45-48. DOI: 10.9790/0853-1601014548.
- [4] P. Prochor and Z. A. Mierzejewska, Bioactivity of PEEK GRF30 and Ti6Al4V SLM in simulated body fluid and Hank's balanced salt solution. *Materials*, 2021, 14, 2059-1-17. <http://doi.org/10.3390/ma14082059>.
- [5] S. Shaikh, S. Kedia, D Singh, M. Subramanian and S. Sinha, Surface texturing of Ti6Al4V alloy using femtosecond laser for superior antibacterial performance. *J. Laser Appl.*, 2019, 31, 022011, 1-10. <http://doi.org/10.2351/15081106>.
- [6] G. Menci, A. G. Demir, D. G. Waugh, J. Lawrence and B. Previtali, Laser surface texturing of β -Ti alloy for orthopedics: Effect of different wavelengths and pulse duration. *Appl. Surf. Sci.*, 2019, 489, 175-186. <http://doi.org/10.1016/j.apsusc.2019.05.111>.
- [7] A. I. A. Morales, S. Alamri, T. Kunze and A. F. Lasagni. Influence of processing parameters on surface texture homogeneity using direct laser interference patterning. *Opt. Laser Tech.*, 2018, 107, 216-227.
- [8] T. Kokubo and H. Takadama, How useful is SBF in predicting in vivo bone bioactivity. *Biomaterials*, 2006, 27, 2907-2915. <doi:10.1016/j.biomaterials.2006.01.017>.
- [9] N. Sirdeshmukh and G. Dongre. Laser micro & nano surface texturing for enhancing osseointegration and antimicrobial effect of biomaterials: A review. *Materials Today: Proceeding*, 2021, 44, 2348-2355. <http://doi.org/10.1016/j.matpr.2020.12.433>.
- [10] B. S. Moon, S. Kim, H. E. Kim and T. S. Jang. Hierarchical micro-nano structured Ti6Al4V surface topography via two-step etching process for enhanced hydrophilicity and osteoblastic responses. *Mat. Sci. Eng. C*, 2017, 73, 90-98. <http://doi.org/10.1016/msec.2016.12.064>.
- [11] D. J. Cohen, A. Cheng, K. Sahingur, R. M. Clohessy, L. B. Hopkins, B. D. Boyan and Z. Schwartz. Performance of laser sintered Ti-6Al-4V implants with bone-inspired porosity and micro/nanoscale surface roughness in the rabbit femur. *Biomed. Mater.*, 2017, 12, 025021. <https://doi.org/10.1088/1748-605X/aa6810>.
- [12] S. Shaikh, S. Kedia, A. K. Singh and S. Sinha, Surface treatment of 45S5 bioglass using femtosecond laser to achieve superior growth of hydroxyapatite. *J. Laser Appl.*, 2017, 29, 022004-1-8. <http://dx.doi.org/10.2351/14979304>.

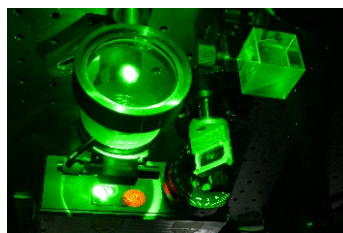
Tunable Cavity Parameters

Polarization-based Laser Resonator Cavity

Siba Prasad Sahoo^{1,2*}, V.S. Rawat^{1,2}, Jaya Mukherjee^{1,2} and Swarupananda Pradhan^{1,2}

¹Homi Bhabha National Institute, Anushaktinagar, Mumbai-400094, INDIA

²Beam Technology Development Group, Bhabha Atomic Research Centre, Mumbai-400085, INDIA



The setup assembled for the purpose of carrying out experiments on Polarization based Laser Resonator Cavity

ABSTRACT

We have developed a polarization-based laser resonator cavity which provides continuous tuning of various cavity parameters preserving the cavity alignment. The cavity houses intracavity polarization optics inside a confocal resonator. The resonator cavity facilitates continuous tuning of the output coupling and allows flexible optimization of various laser parameters like output energy, cavity buildup time, and laser pulse width at different pump pulse energies. The optimum output coupler reflectivity of a laser system can be accurately determined at different input pump power levels using this resonator configuration. The resonator cavity also allows accurate determination of the round trip resonator losses and small-signal gain coefficient of a laser system. This system can be useful for all-optical synchronization of multiple laser pulses as desired in many spectroscopic experiments.

KEYWORDS: Polarization-based resonator cavity, Variable output coupling, Gain coefficient, Round trip resonator losses, Gain-coefficient, Delay synchronization

Introduction

The extraction efficiency of a laser resonator cavity with fixed resonator losses depends on the total gain of the system and the reflectivity of the output coupler. The gain of the system is a function of the input pump power. Hence, it is a tedious task to optimize the output power of a given laser resonator cavity as the input pump power is changed. The optimum coupling from a particular gain medium is generally achieved by replacing several output couplers of different reflectivity [1-2]. Apart from being tedious, this methodology has limitation in respect to reproducibility and reliability. This is because each time after replacement of the output coupler, the resonator cavity has to be realigned. Various other techniques like a dielectric-coated tapered reflector, Gaussian reflectivity mirror, Michelson interferometer-based reflector, Fabry-Perot interferometer based reflector, Frustrated Total Internal Reflection (FTIR) based reflector, and anti-resonance ring interferometer have been tried for continuously varying the reflectivity of the output coupler with their trade-off [3-7].

We have designed and developed a polarization-based laser resonator that allows continuous tuning of the output coupler reflectivity without any misalignment to the cavity. The laser resonator cavity was developed and studied using Cr:forsterite as the gain medium. Various cavity parameters like output energy, intracavity energy, buildup time, laser pulse width, and threshold pump pulse energy are studied as a function of the output coupling at different pump pulse energies.

Experimental Setup

The schematic of the experimental setup of the polarization-based laser resonator cavity is shown in Fig. 1. A Cr:forsterite crystal having a dimension of 5 mm x 5mm x 12 mm is used as gain medium in this experiment. The crystal has

an absorption coefficient of 1.47 cm^{-1} at 1064 nm for polarization along *b*-axis (E || *b*) and a Figure Of Merit (FOM) of 17. The crystal is pumped by the fundamental frequency (1064 nm) of a Q-switched Nd:YAG laser having a pulse repetition rate of 10 Hz. The pump beam has a diameter of 8 mm and a divergence of 0.5 mrad. The pump beam is focused slightly away from the crystal to avoid damage, using a 1000 mm focal length lens (L). The intensity of the pump beam is varied using a half-wave plate and a polarizing beam splitter (PBS).

The laser resonator cavity consists of two high reflecting concave mirrors (M1 and M2) in confocal geometry, an intracavity polarizing beam splitter cube (I-PBS), and a retardation plate (RP). The high reflecting concave mirrors have a radius of curvature of 100 mm, the reflectivity of >99% at 1150 -1350 nm, and the transmission of ~ 98% at 1064 nm. The pump polarization is made collinear with *a*-axis of the crystal by using a half-wave plate ($\lambda/2$ plate) placed before the crystal and the beam emerging from the crystal is vertically polarized. The reflectivity of the output coupler is varied using the Retardation Plate (RP), placed in between the I-PBS and

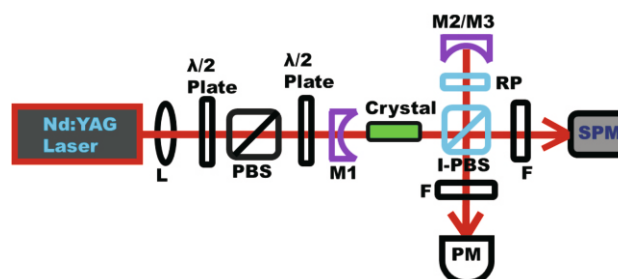


Fig.1: Schematic of the experimental setup of the polarization-based Cr:forsterite laser resonator cavity. L: 1000 mm focal length lens; PBS: polarizing beam splitter, M1, M2: concave mirrors, roc:100mm, R: 99% @1150-1350nm, T: 98% @1064nm; M3: concave partial reflecting mirror, roc:100 mm, R:95%@1150-1350 nm; I-PBS: intracavity polarizing beam splitter; RP: retardation plate; PM: power meter; F:1064 nm filter; SPM: spectrometer.

*Author for Correspondence: Siba Prasad Sahoo
E-mail: sibaps@barc.gov.in

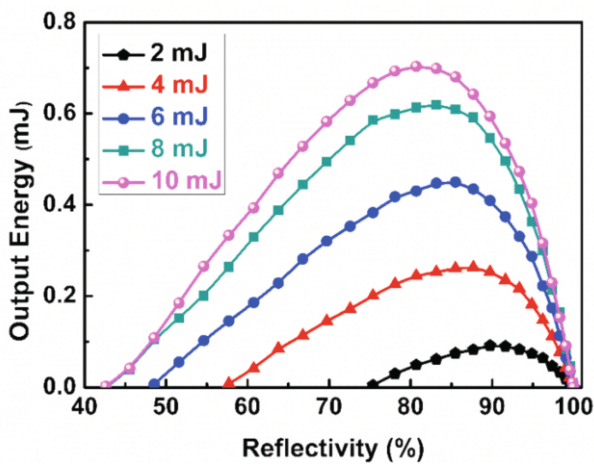


Fig.2: Variation of the output energy of the resonator cavity as a function of the output coupler reflectivity for different pump pulse energies.

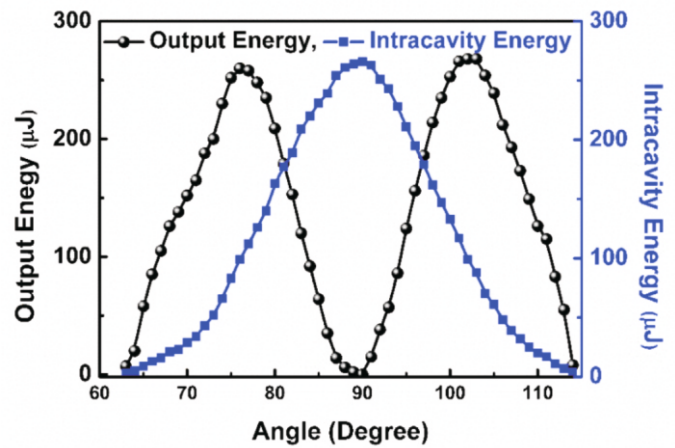


Fig.3: Variation of the intracavity energy and cavity output energy as a function of retardation plate angle.

mirror M2. The intracavity beam reflected from the I-PBS oscillates in between the resonator mirror M1 & M2 and the laser output is obtained through the transmission part of the I-PBS along the orthogonal direction. The state of polarization of the laser beam as well as the laser output energy can be controlled by changing the angle of the retardation plate.

The output coupler reflectivity is calculated from the angle of rotation of the retardation plate using the Jones matrix formalism and found to be varied from 100% to 13% at Cr:forsterite laser wavelength[8].

Results & Discussion

Study of Cavity Output Energy

The variation of the output energy of the resonator cavity with the reflectivity of the output coupler at different pump pulse energies is shown in Fig.2.

For a particular pump pulse energy, the output energy increases with an increase in the output coupler reflectivity becomes maximum and then decreases. The intracavity energy increases with an increase in the output coupler reflectivity which increases the output energy. The transmission of the output coupler decreases with an increase in the output coupler reflectivity which results in a decrease in the output energy. Hence, the output energy has an optimum value at certain reflectivity of the output coupler (for a fixed pump pulse energy and resonator losses). For a laser system, the value of optimum output coupler reflectivity will be different at different pump pulse energies. The polarization-based laser resonator provides optimization of the laser output energy at different pump pulse energies by simply rotating the retardation plate. This doesn't require a change in any other components of the laser system. From Fig.2 it can also be observed that the lasing output starts at a certain value of output coupler reflectivity known as the threshold output coupler reflectivity. Fig.2 shows that both the optimum and threshold output coupler reflectivity value is shifting towards the lower value with the increase in the pump pulse energy. The gain of the system increases with the pump pulse energy, hence even lower feedback from the output coupler can overcome the resonator losses. Therefore, the resonator threshold and the optimum output energy are achieved at a lower value of output coupler reflectivity. For lower pump energy, the gain is small, hence higher feedback is required to overcome the resonator losses. Therefore, the resonator

threshold, as well as the optimum output coupling occurs at higher a value of reflectivity. The polarization-based laser resonator cavity provides an accurate determination of the threshold and optimum output coupler reflectivity value of a laser system at different pump pulse energies.

Study of Intracavity Energy

The variation of intracavity energy of the resonator with the output coupler reflectivity is studied by replacing the high reflecting concave mirror M2 with a 95% reflecting concave mirror M3 and shown in Fig.3. The transmitted energy through M3 is proportional to the intracavity energy.

The intracavity energy is zero when the total gain of the system can not overcome the total resonator losses. This defines the lasing threshold and the corresponding reflectivity of the output coupler is the threshold output coupler reflectivity. The intracavity energy is maximum for retardation plate angle at 90°, which corresponds to output coupler reflectivity of 100%. Thus, the output energy of the resonator cavity is zero. As the retardation plate is further rotated beyond 90°, the intracavity energy decreases from its maximum value with a decrease in the output coupler reflectivity and becomes zero at the threshold reflectivity value.

Study of Buildup Time and Laser Pulse Width

The buildup time of a laser plays an important role in the temporal delay synchronization of multiple laser beams. For several laser spectroscopic experiments like resonance ionization spectroscopy, multiphoton absorption spectroscopy, coherent anti-stoke Raman spectroscopy (CARS), the delay of multiple laser beams needs to be synchronized. This is normally achieved either by electronic delay or by external optical delay. For this purpose, the polarization-based resonator cavity can be a good choice where the cavity buildup time, and hence the delay of the laser beam can be optically varied continuously. The variation of the cavity buildup time and laser pulse width (FWHM) is studied as a function of the output coupler for different pump pulse energies as shown in Fig.4.

The cavity buildup time decreases with an increase in the reflectivity of the output coupler for a fixed pump pulse energy. The cavity buildup time also decreases with an increase in the input pump energy as higher gain leads to faster growth of the signal with a fixed cavity loss. The cavity buildup time can be continuously tuned from a few tens of ns to a few hundred ns

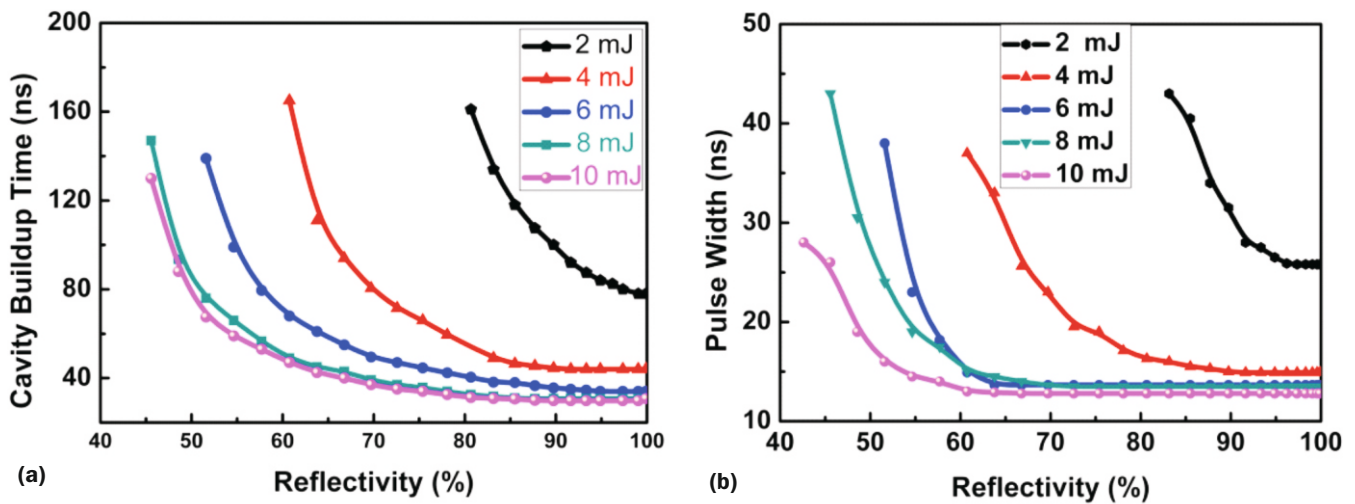


Fig.4: (a, b). Variation of cavity buildup time and laser pulse width with output coupler reflectivity for different input pump pulse energies.

and hence can be used to precisely control the delay of the laser beam. The laser pulse width decreases with an increase in the reflectivity of the output coupler and finally reaches a plateau. From Fig. 4(b), it can be observed that the laser pulse width remains constant over a wider range of reflectivity (~65-99%) at higher pump pulse energy (> 4mJ). In this range, the buildup time can be varied by simply rotating the retardation plate while maintaining the pulse width constant. Hence, the resonator cavity provides precise delay control of laser pulse which can be used in many spectroscopic applications delaysynchronization.

Study of Threshold Pump Pulse Energy

The polarization-based laser cavity provides an accurate method of measuring the threshold pump energy for different values of the output coupler reflectivity without disturbing the cavity alignment, unlike the conventional method of changing the output coupler. This allows the determination of round trip resonator losses and gain-coefficient of laser system using the Findlay-Clay analysis in which the threshold pump energy is measured as a function of output couplers reflectivity [9].

Fig. 5 shows the variation of the input threshold pump energy (E_{th}) versus output coupler reflectivity ($-\ln R$), from which the roundtrip resonator losses (δ) and the small-signal gain coefficient (g_0) of the system are determined using the laser threshold condition.

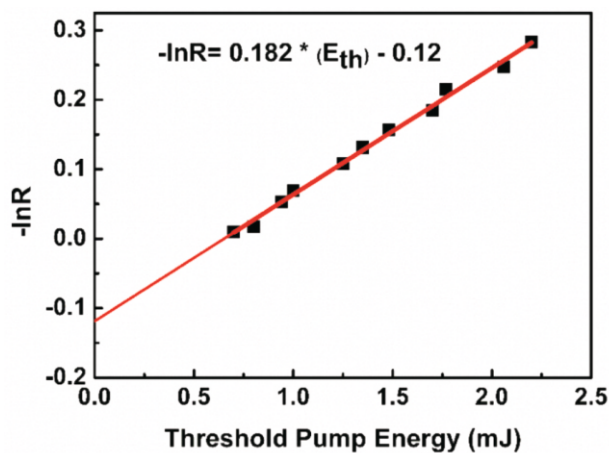


Fig.5: Threshold pump energy (E_{th}) as a function of the output coupler reflectivity ($-\ln R$).

$$2g_0l = \delta - \ln R \approx \delta + T, \text{ and } -\ln R = \frac{2\eta}{Al_s} E_{in} - \delta$$

where l , A , l_s and η are the length of the crystal, the effective cross-sectional area of the crystal, the energy density inside the laser resonator, and the total efficiency of the laser respectively [10]. Consequently, the δ and g_0 are found to be 12% and, $0.076 \times E_{in} \text{ (cm}^{-1}\text{)}$ respectively [11]. The small-signal gain coefficient (g_0) of the system at the threshold pump energy of 0.65 mJ is 0.045 cm^{-1} .

Conclusions

A polarization-based resonator cavity is developed using an intracavity polarization beam splitter cube, and a retardation plate inside a confocal resonator using Cr:forsterite crystal as the gain medium. The rotation of the retardation plate facilitates continuous tuning in the output coupling without disturbing the cavity alignment. The cavity output energy, cavity buildup time, laser pulse width, and the threshold pump energy are measured as a function of the output coupler reflectivity. The round trip resonator losses and small-signal gain coefficient of the system are determined using Findlay-Clay analysis at the laser threshold. The developed resonator cavity provides *in situ* control of the laser pulse delay without changing the laser pulse width which can be used in many spectroscopic experiments for delay synchronization. It also provides an ideal platform for the study of the basic mechanism associated with laser physics.

Acknowledgement

The authors would like to express their sincere gratitude to Archana Sharma, Director, BTDG for her interest and encouragement in this work.

References

[1] E. Georgiou, O. Musset, and J.P. Boquillon, High-efficiency and high-output pulse energy performance of a diode-pumped Er:Yb:glass 1:54 μm laser, *Appl. Phys. B.*, 2000, 70, 755–762.
 [2] Nickolay Zhavoronkov, Aleksander Avtukh, and Victor Mikhailov, Chromium-doped forsterite laser with 1.1 W of continuous-wave output power at room temperature, *App. Opt.*, 1997, 36, 8601-8605.
 [3] S. De Silvestri, P. Laporta, V. Magni, O. Svelto, C. Arnone, C. Cali, S. Sciortino and C. Zizzo, Nd:YAG laser with multi dielectric variable reflectivity output coupler, *Opt. Comm.*, 1988, 67, 229-232. Anthony W. Yu, S. Zhu, and Rajarshri Roy, *App. Opt.*, 1985, 24, 3610-3614.
 [4] Joseph F. Pinto and Leon Esterowitz, Unstable Cr:LiSAF laser resonator with a variable reflectivity output coupler, *App. Opt.*, 1998,

37, 3272-3275.

[5] S. De Silvestri, P. Laporta, V. Magni, and O. Svelto, Radially variable reflectivity output coupler of novel design for unstable resonators, *Opt. Lett.*, 1987, 12, 84-86.

[6] Anthony W. Yu, S. Zhu, and Rajarshri Roy, Variable transmission output coupler and tuner for ring laser systems, *App. Opt.*, 1985, 24, 3610-3614.

[7] U. U. Graf, A. I. Harris, J. Stutzki, and R. Genzel, A variable reflectivity output coupler for optically pumped far infrared lasers, *Int. J. of Inf. and Mil. Waves*, 1992, 13, 1313-1320.

[8] Siba Prasad Sahoo, S. Pradhan, Jaya Mukherjee, and V.S. Rawat, "investigation of a polarization-based Cr:forsterite laser resonator cavity", *J. of Modern Optics*, 2021, 68, 707-716.

[9] D. Findlay & R. A. Clay, The measurement of internal losses in 4 level lasers, *Phy. Lett.*, 1966, 20 277-278.

[10] Walter Koechner and Michael Bass, "Solid-State Lasers", Springer-Verlag New York Inc., 2003.

[11] Siba Prasad Sahoo, V.S. Rawat, Jaya Mukherjee, S. Pradhan, Determination of gain coefficient and roundtrip resonator losses of Cr:forsterite laser using a polarization resonator cavity, 29th DAE-BRNS national laser symposium (NLS-29) February 12-15, 2021.

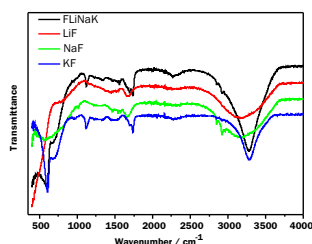
Indian Molten Salt Breeder Reactor

Thermophysical Properties of Frozen Coolant Salt

Rimpi Dawar^{1,2*}, S. Kolay¹, S. Phapale^{1,2} and R. Mishra^{1,2}

¹Chemistry Division, Bhabha Atomic Research Centre, Mumbai-400085, INDIA

²Homi Bhabha National Institute, Anushaktinagar, Mumbai-400094, INDIA



IR spectrum of
FLiNaK, LiF, NaF and KF

ABSTRACT

This report summarises experimental data on thermo physical properties of frozen coolant salt for high temperature Molten Salt Breeder Reactor (MSBR). Based on superior physical, nuclear and chemical properties, eutectic mixture containing 46.5 mol. % LiF, 11.5 mol. % NaF and 42.0 mol. % KF (FLiNaK) has been proposed as coolant salt for MSBR. In this report, thermo-physical data of frozen coolant salt such as melting point, latent heat of fusion, thermal conductivity, density, heat capacity, coefficient of thermal expansion etc. are presented which are required to calculate its heat transport properties. This data is necessary for the accurate design of freeze valve which is a key component of MSRs passive safety system.

KEYWORDS: Molten salt reactor, Coolant salt, FLiNaK, Freeze valve, Passive safety, Thermo-physical properties.

Introduction

Molten salt breeder reactor (MSBR) is one among the six innovative reactor concepts proposed by Generation IV international forum (GIF) to establish enhanced sustainability, feasibility, safety, high thermal efficiency and proliferation resistance[1-5]. At ORNL, from 1958 to 1976, molten salt reactor program was operated with the objective of development of fluid fuelled nuclear reactor[6]. In these reactors, fuel (fissile or fertile material dissolved in suitable carrier salt) is circulated through heat exchangers, hence these fluids act as both fuel (producing heat) and coolant (transferring the heat). As a part of three stage Indian nuclear power programme, for effective utilization of its large thorium reserves, MSRs are considered as long term sustainable solution for energy demand. For Indian molten salt breeder reactor (IMSBR) the proposed fuel (also primary coolant) is mixture of LiF-CaF₂-ThF₄-UF₄ (70:8:20.6:1.4 mol.%) and coolant (secondary) is eutectic mixture of LiF-NaF-KF (46.5:11.5:42 mol.%) i.e. FLiNaK. For enhanced safety in these Gen IV reactors, passive shut down system is key component. In MSRs, instead of relying only on traditional nuclear safety approach of inserting control rods to make nuclear reactor subcritical, self-draining (transfer) of molten salt into passively cooled subcritical tanks due to gravity in case of any power outage scenario, is efficient safe shut down mechanism. After draining, molten salt solidifies in drain tanks and hence trapping dangerous radioactive fission products. A critical component of the molten salt (fuel as well as coolant) circuit and the associated salt conditioning system is the freeze valve[7-10], where the flow of molten salt is prevented by freezing a section of the pipe (solid plug) during reactor normal operation. In the accidental scenario, when the reactor overheats due to failure of other active control systems, the

plug will melt. During any accidental scenario, failure of this freeze valve to thaw the molten salt poses a major safety concern regarding integrity of the fuel salt system. It could lead to release of hazardous material in the environment[11]. Hence the accuracy in the design of the freeze valve becomes very important in order to ensure more efficient passive shutdown system. In order to optimise its design, the freeze and thaw phenomena of the molten salt (fuel and coolant) needs to be modelled, for which the thermo-physical data of both fuel and coolant salt is required[10,12-16]. In the present study, data on thermo-physical parameters of frozen coolant salt are reported. These data are required to estimate the melting time for the frozen salt in the coolant salt drain tank when salt needs to be put back in reactor system after any necessary repairs (maintenance)/ trouble – shooting event.

Salt Preparation and Characterization

The sample was prepared by thoroughly mixing perfectly dried constituent fluoride salts i.e. LiF, NaF and KF of desired molar ratio in an agate mortar. As this salt mixture is highly hygroscopic, it was first heated at 473 K under dynamic vacuum (10⁻³ mbar) for 48 hours to remove the moisture. The sample was then melted at 823 K and homogenized for 10 hours at the same temperature under dynamic vacuum. The phase purity of thus prepared salt was ascertained using powder X-ray diffraction (XRD) technique. X-ray diffraction pattern of FLiNaK was recorded employing Cu K α radiation of PANalytical X-pert Pro diffractometer. Since FLiNaK is highly hygroscopic so perfectly dried FLiNaK was covered with kapton tape for recording its XRD pattern. Analysis of XRD pattern for phase identification was aided by the ICDD-PDF-2 database.

The observed reflections in the powder XRD data of FLiNaK are found to be in good agreement with reported XRD pattern[17]. XRD pattern of frozen FLiNaK shows peaks of starting compounds i.e. LiF(s), NaF(s) and KF(s). No peak due

*Author for Correspondence: Rimpi Dawar
E-mail address: rimpid@barc.gov.in

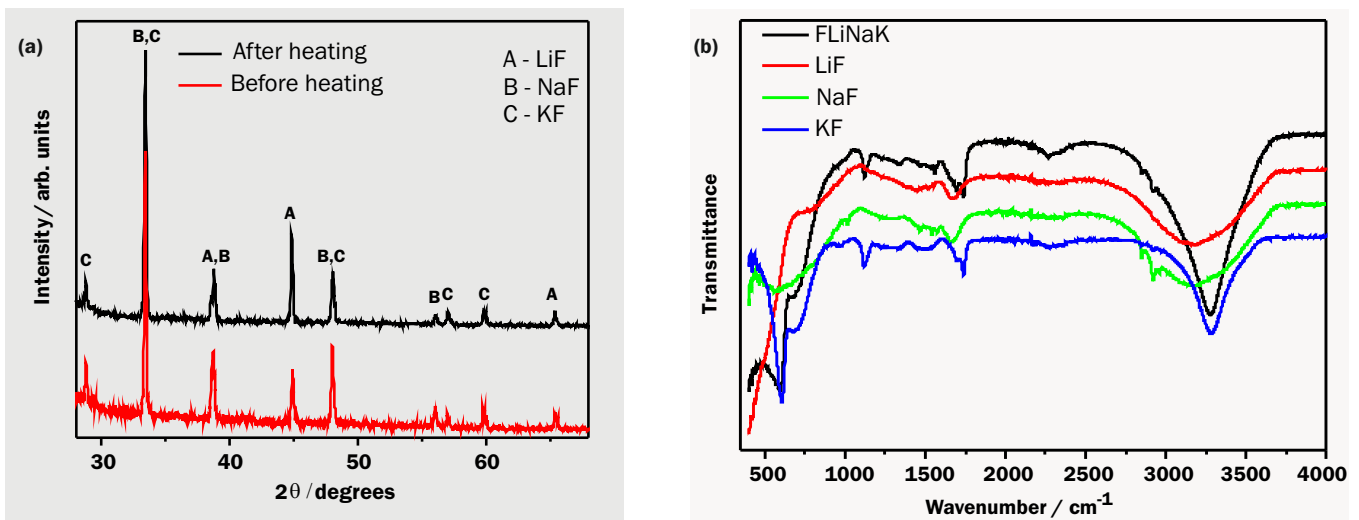


Fig.1: (a) XRD pattern of solidified FLiNaK, (b) IR spectrum of FLiNaK, LiF, NaF and KF.

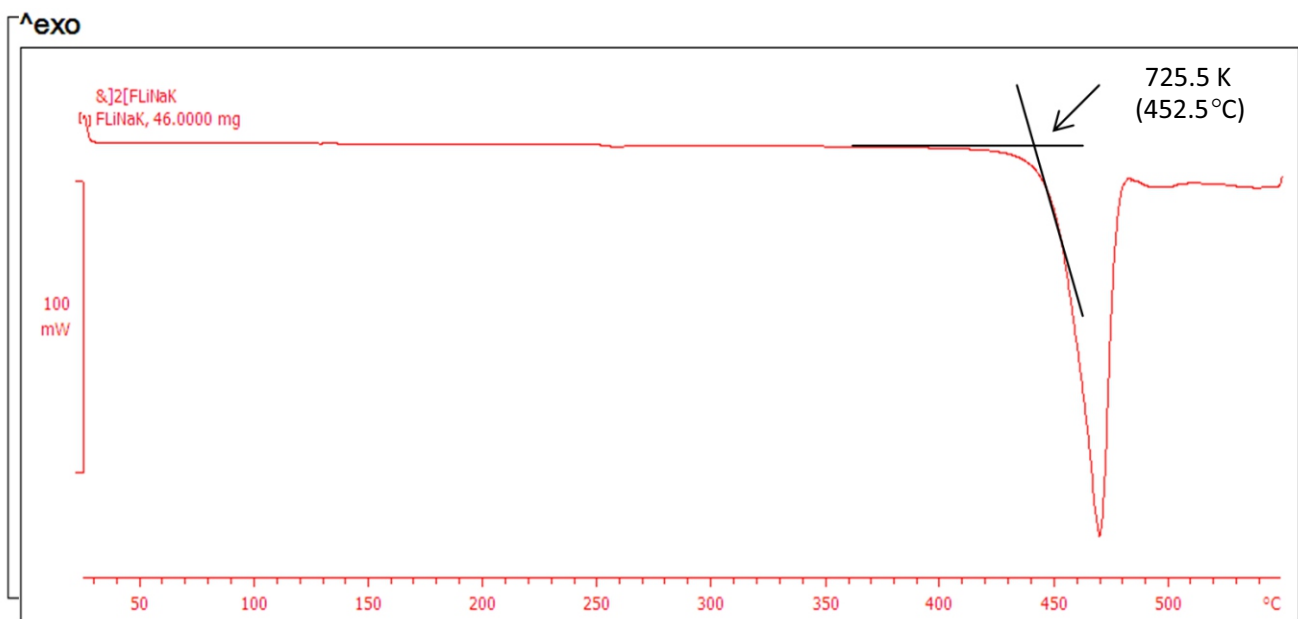


Fig.2: DSC plot for FLiNaK.

to any oxy-fluoride compounds was observed. The comparison of XRD peaks before and after heating of FLiNaK is shown in Fig. 1(a). The absence of any oxy-fluoride compound in FLiNaK was also confirmed using infrared spectroscopy. The FTIR spectra has been recorded using Alpha-II spectrophotometer (Bruker make) in attenuated total reflection (ATR) mode within the wavenumber region 400 to 4000 cm^{-1} . The infrared frequencies corresponding to molecular vibrations of sample get absorbed when infrared light interacts with sample. The IR spectrum of FLiNaK is shown in Fig. 1(b). All the peaks observed in FLiNaK were identified to be due to LiF, NaF and KF only.

Thermo-physical properties of frozen FLiNaK

After salt characterization, the following properties of frozen FLiNaK were measured and compared with literature.

- Melting point
- Density
- Heat capacity
- Thermal diffusivity
- Thermal expansion coefficient

Melting point

Melting point of coolant salt was determined employing a MettlerToledo DSC instrument (DSC1 Star^o system). This instrument was calibrated for temperature measurement using In, Sn, Zn as standards. In the present study, salt was sealed in aluminum crucible and the DSC run was recorded (Fig. 2) in the temperature range 298 to 823 K at a heating rate of 5K/min under high pure argon flow. The heat flux was recorded as function of temperature. The melting point was found to be 725.5 K against the reported value of 727 K [18,19].

Density

The density of the frozen FLiNaK at room temperature was determined using liquid immersion technique employing Archimedes Principle. Perfectly dried toluene was used as liquid in which FLiNaK pellet was immersed. As FLiNaK is highly hygroscopic so any liquid containing even trace amount of water cannot be used as it will lead to inaccuracy in weight measurement. In this procedure, the apparent weight loss suffered by the sample when immersed in liquid was measured using a sensitive single pan electronic balance. A density measurement accessory supplied along with this balance was

used for this purpose. This accessory consisted of a cradle for immersing the pellet into the liquid and a table for supporting a beaker containing the pellet. The density value reported is the arithmetic mean of the values measured with as many as five pellets. Before measuring the density of FLiNaK, equipment was first calibrated by measuring density of few standards e.g. gold, aluminium.

Equation for density measurement:

Vol. of the displaced liq. = mass of displaced liq./density of liq.
 = mass of displaced liq./0.87

(Density of toluene is 0.87 g/ml at 298K)

Mass of displaced liq. = mass of FLiNaK in air – mass of FLiNaK in liq.

Therefore,

$$\rho(\text{FLiNaK}) = \left[\frac{\text{weight of FLiNaK in air}}{\text{volume of displaced liq.}} \right] \quad (1)$$

The density of FLiNaK at 298 K was found to be 2.552±0.01 g/ml. The reported value of density of solid FLiNaK at 293 K is 2.56 g/ml[20].

Heat Capacity

Heat capacity $C_{p,m}^{\circ}(T)$ of solid FLiNaK was measured in the temperature range of 300-650 K with a heating rate of 5K min⁻¹ using a pre-calibrated Mettler Toledo Differential Scanning Calorimeter (DSC I) under the flow of high purity argon gas. Classical three-step method viz., blank, sapphire and sample runs in a step heating mode was employed for measuring the heat capacity. About 50 mg FLiNaK was taken in a sealed 40µl Al pan for the heat capacity measurement. The heat capacity of FLiNaK as a function of temperature could be expressed as:

$$C_{p,m}^{\circ} / \text{J mol}^{-1}\text{K}^{-1} = 25.1 + 0.037 * T + 703840 / T^2 \quad (2)$$

Fig.3 gives comparison of measured heat capacity of solid FLiNaK as a function of temperature with literature value[21]. The measured heat capacity values as a function of temperature were used for calculating thermal conductivity values of FLiNaK.

Coefficient of Thermal Expansion

Coefficient of thermal expansion of a material is a very important parameter in order to estimate extent of its swelling at a specified temperature. In the present study, thermal expansion coefficient of frozen FLiNaK was measured

employing Linseis Dilatometer in the temperature range 523 - 623 K. Sintered FLiNaK pellet (6mm dia) was loaded in the instrument and heated to 523 K under dynamic vacuum of 10⁻⁵ mbar to remove any adsorbed moisture. Then the change in length of pellet (ΔL) was measured under high pure argon gas at a heating rate of 6 K/min. The change in length per unit length ($\Delta L/L$) of FLiNaK sample can be expressed as

$$\Delta L/L = -0.01206 + 3.94 \times 10^{-5} T/K \quad (3)$$

The coefficient of average linear thermal expansion can be calculated as

$$\alpha_L = \frac{1}{L_0} \left(\frac{\Delta L}{\Delta T} \right) \quad (4)$$

Coefficient of thermal expansion of FLiNaK was found to be

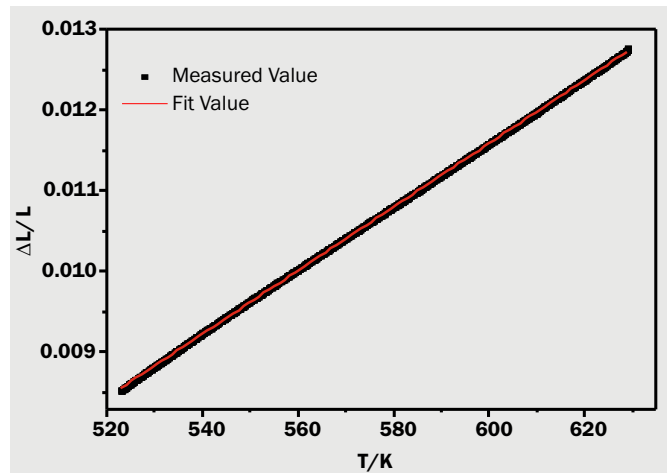


Fig.4: Thermal expansion of FLiNaK as a function of temperature.

3.84 x 10⁻⁵ / K. The plot of change in length per unit length ($\Delta L/L$) vs temperature is given in Fig. 4.

The data on thermal expansion of FLiNaK will be useful during optimization of the design parameters of freeze valve in order to avoid any mechanical interaction between salt and constituent material of freeze valve.

Thermal Conductivity

Determination of thermal conductivity of FLiNaK as a function of temperature is of great importance in order to predict its heat transport properties. Thermal diffusivity of frozen FLiNaK was measured employing laser flash technique

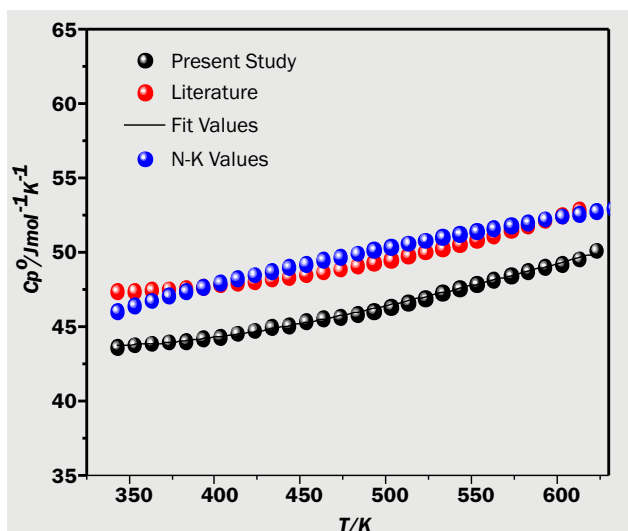


Fig.3: Heat capacity of solid FLiNaK as a function of temperature.

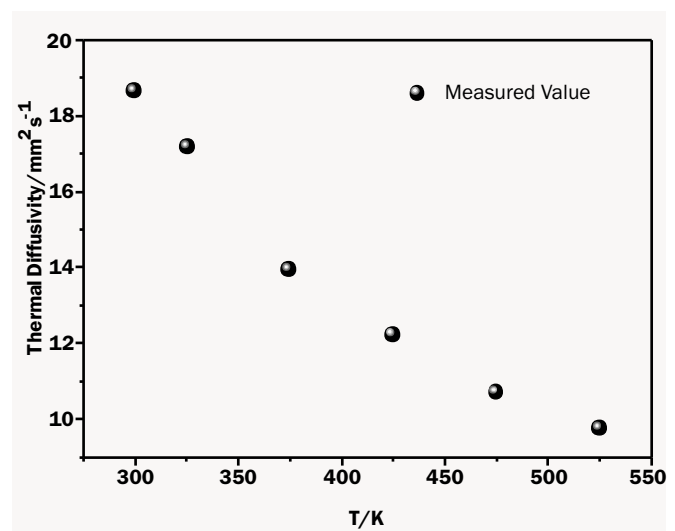


Fig.5: Thermal diffusivity of FLiNaK as a function of temperature.

(LFA 427, M/s. NetzschGmbH, Germany) using Nd-YAG Pulsed laser of duration 0.4 ms. The sample in the form of pellet (diameter 10 mm and thickness ~1 mm) was equilibrated at 298, 323, 373, 423, 473, 523 K under dynamic vacuum of 10^{-6} mbar. The temperature dependence of thermal diffusivity of FLiNaK is shown in Fig. 5. Thermal diffusivity of FLiNaK decreases with temperature and follow inverse temperature dependence behaviour. The temperature dependence of thermal diffusivity of FLiNaK can be expressed as following equation:

$$\frac{1}{\text{thermal diffusivity (FLiNaK)} / \text{mm}^2 \text{s}^{-1}} = -0.01213 + 2.20074 \times 10^{-4} T/K \quad (5)$$

Thermal conductivity (K) of the FLiNaK at above mentioned temperatures was calculated from the measured values of thermal diffusivity, heat capacity and density using the following relation.

$$K(T) = \text{Thermal diffusivity}(T) \times C_p(T) \times \rho(T) \quad (6)$$

Thermal diffusivity value taken for thermal conductivity calculation at each temperature is the arithmetic mean of three different measurements. The values of heat capacity as a function of temperature was calculated using equation 2 and temperature dependence of density was calculated using linear thermal expansion data measured using dilatometer. The values of thermal conductivity of FLiNaK as a function of temperature can be expressed in the form of following equation:

$$\frac{1}{K (\text{FLiNaK}) / \text{Wm}^{-1}\text{K}^{-1}} = -0.02322 + 8.2107 \times 10^{-4} T/K \quad (7)$$

The values of K as a function of temperature are given in Fig.6.

Summary

Coolant salt proposed for IMSBR i.e. FLiNaK was prepared and characterized. The thermo-physical properties of frozen FLiNaK were measured. These properties are required for modelling freezing and thaw phenomenon and hence for designing of freeze valve which is a key component of passive safety system of MSRs.

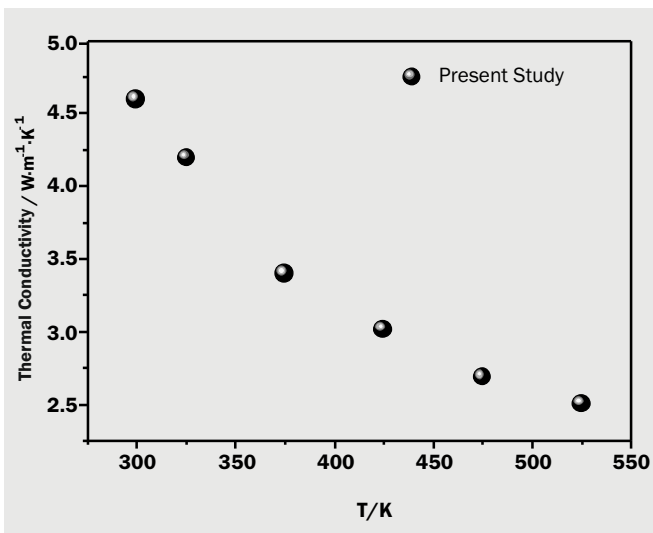


Fig.6: Temperature dependence of thermal conductivity of solid FLiNaK.

Acknowledgements

The authors of this manuscript sincerely thank Dheeraj Jain, Chemistry Division for thermal diffusivity measurements, Ashok Sahu, GAMD for thermal expansion measurements, Abhishek Basak, High Temperature Reactor Section for constant support and useful suggestions for the manuscript.

References

- [1] Serp J., Allibert M., Beneš O., Delpech S., Feynberg O., Ghetta V., Heuer D., Holcomb D., Ignatiev V., Kloosterman J. L., Luzzi L., Merle-Lucotte E., Uhlir J., Yoshioka R., Zhimin D. "The molten salt reactor (MSR) in generation IV: overview and perspective". Progress in Nuclear Energy, 2014, 77, 308-319.
- [2] Boussier H., Delpech S., Ghetta V., Heuer D., Holcomb D.E., Ignatiev V., Merle-Lucotte E., Serp J. "The molten salt reactor (MSR) in generation IV: overview and perspectives". GIF Symposium - San Diego (California), 2012, 77-91.
- [3] Ashraf. O, Smirnov. A. D, Tikhomirov. G. V. "Modeling and criticality calculation of the Molten Salt Fast Reactor using Serpent code", Journal of Physics: Conference Series, 2019, 1189.
- [4] Reinberger. D, Ajanovic. A, Haas. R. The technological and Economic Future of Nuclear Power. Energiepolitik und Klimaschutz. Energy Policy and Climate Protection; Springer VS: Wiesbaden, 2019.
- [5] Gougar. H. D, Bari R. A, Kim. T. K, Sowinski. T. E, Worrall. A. "Assessment of the technical maturity of Generation IV concepts for test or demonstration reactor applications" INL/EXT-15-36427 TRN: US1600272; Idaho National Lab. (INL), Idaho Falls, ID (United States): 2015-10-01, 2015.
- [6] Singh. V, Lish. M. R, Chvála. O, Upadhyaya. B. R. "Dynamics and control of molten-salt breeder reactor". Nuclear Engineering and Technology, 2017, 49, 887-895.
- [7] Chisholm. B. M, Krahn. S. L, Sowder. A. G. "A unique molten salt reactor feature - The freeze valve system: Design, operating experience, and reliability". Nuclear Engineering and Design, 368, 2020, 368.
- [8] Guymon. R. "MSRE systems and components performance; ed. and comp." Oak Ridge National Lab., Tenn.(USA): 1973.
- [9] Elsheikh. B. M. "Safety assessment of molten salt reactors in comparison with light water reactors". Journal of Radiation Research and Applied Sciences, 2013, 6, 63-70.
- [10] Richardson. M. "Development of freeze valve for use in the MSRE" ORNL-TM-128, Feb. 1962.
- [11] Beall. S. E., Haubenreich. P. N., Lindauer. R. B., Tallackson. J. R. "MSRE design and operations report". Part V. Reactor safety analysis report; Oak Ridge National Lab., ORNL-TM-732, August 1964.
- [12] Giraud. J, Ghetta. V, Rubiolo. P, Retamales. M. T. "Development of a cold plug valve with fluoride salt". EPJ Nuclear Sciences & Technologies, 2019, 5, 9.
- [13] Makkinje. A. Design of a freeze plug grate. TU Delft, 2017.
- [14] Shafer. D. Design and melting behavior of the MSFR freeze plug. 2018.
- [15] Swaroop. P, Rohde. M, Kloosterman. J. L. "Design of a freeze plug for the molten salt reactor (MSR)". Master's thesis, TU Delft, 2015.
- [16] van Tuyl. F. "A new design for the safety plug in a molten salt fast reactor". Bachelor's thesis, TU Delft, 2016.

- [17] An. X.-H, Cheng. -H, Su. T, Zhang. P. "Determination of thermal physical properties of alkali fluoride/carbonate eutectic molten salt". AIP Conference Proceedings, 2017, 1, 1850.
- [18] Williams. D. F., "Assessment of Candidate Molten Salt Coolants for the NNGP/NHI Heat-Transfer Loop".United States, 2006-06-30, 2006.
- [19] Lumsden. J., "Thermodynamics of molten mixtures of alkali-metal halides", Discussions of the Faraday Society, 1961, 32, 138-146.
- [20] Williams. D. F., "Additional Physical Property Measurements and Assessment of Salt Compositions Proposed for the Intermediate Heat Transfer Loop", September 2006.
- [21] Caraballo. A, Galán-Casado. S, Caballero. Á, Serena. S. "Molten Salts for Sensible Thermal Energy Storage: A Review and an Energy Performance Analysis". Energies, 2021, 4, 14.

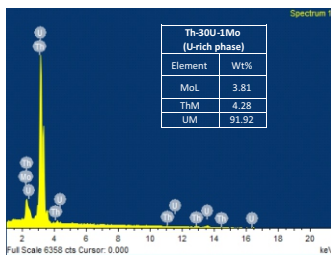
Metallic Fuels

Microstructural and Diffraction Studies on Th-U and Th-U-Mo Alloys

Raj Kumar^{1*}, Sourabh Wajhal², Sonal Gupta¹, A.B. Shinde², PSR Krishna², S.K. Satpati¹, M.L. Sahu¹

¹Uranium Extraction Division, Bhabha Atomic Research Centre, Mumbai-400085, INDIA

²Solid State Physics Division, Bhabha Atomic Research Centre, Mumbai-400085, INDIA



EDS of the alloys

ABSTRACT

The motivation behind the present study is the resurgence of interest in the metallic fuels and attractive nuclear properties of thorium metal/alloys. In the present study, microstructural and diffraction studies on Th-U-Mo alloys have been presented. Molybdenum was added to the alloys to stabilize uranium as isotropic γ -U phase, to increase fissile loading beyond 20wt% uranium. The microstructures of the alloys were studied using optical microscopy and SEM, and composition of the various phases was determined using EDS. The structural studies were carried out using X-ray and neutron diffraction, and the quantitative estimation of γ -U phase in Th-U-Mo alloys was done using Rietveld method on polycrystalline samples.

KEYWORDS: Metallic fuel, Thorium, Microstructure, X-ray diffraction, Neutron diffraction, Fissile loading, Gamma-Uranium phase

Introduction

Metallic fuels based on uranium were used in the early days of the nuclear energy programme, back in 1960s [1-3]. However, the focus gradually shifted towards ceramic fuels, mainly oxide (UO_2) owing to its higher melting point, fission product accommodation due to relatively open structure and thus higher burnup [2-5]. Recently, there has been resurgence in interest towards metallic fuels, since mid-1980s, owing to their numerous advantages e.g. higher fissile content, better thermal conductivity, ease of fabrication, higher breeding ratio, better inherent safety performance owing to its reduced Doppler reactivity mechanism[2-3, 6-8].

However, uranium based metallic fuels pose certain concerns for fuel designers, viz., irradiation growth, swelling, anisotropic crystal structure of the candidate fuel etc. [2-3, 9]. Metallic fuels based on thorium appear to be better in several aspects than the uranium based metallic fuels. Thorium has isotropic crystal structure, higher melting point, higher thermal conductivity and negligible fission gas swelling [2-3, 10-11]. However, the deployment of thorium based metallic fuels will need sufficient data in terms of their microstructure and phase stability, thermal properties, irradiation stability etc.

Preliminary work on Th-U alloys has been done in late 50s and early 60s. However, favorable properties of thorium based metallic fuels in terms of higher fissile content, higher thermal conductivity, higher breeding gain etc. compared to oxide fuels have gathered renewed research interest in it [2-3, 11-12].

Sustainability of the nuclear energy in the long term will need harnessing of more abundant fertile materials viz. ^{238}U and ^{232}Th in addition to the use of fissile ^{235}U [2, 11, 13-14]. Utilisation of thorium in Indian Nuclear Energy Programme was

envisaged in the very beginning itself. Thorium is 3-4 times more abundant than uranium[13-14]. In the context of Indian scenario, where thorium reserves are vast as compared to leaner reserves of uranium, makes it a strong case for development of thorium-based fuels and reactors. Thorium exists as ^{232}Th which is not fissile like ^{235}U , ^{239}Pu or ^{233}U , the fertile thorium needs to be converted into fissile ^{233}U before it can be used as a nuclear fuel. Thorium being fertile, needs to be combined with fissile material for conversion to fissile ^{233}U . ^{232}Th - ^{233}U fuel cycle can be used in thermal as well as in fast neutron spectrum in contrast to ^{238}U - ^{239}Pu fuel cycle which can be used only in the fast neutron spectrum [13, 15].

Uranium rich phase is finely dispersed in the f.c.c. thorium matrix in Th-($<20wt\%$)U alloys. With increase beyond 20wt%, uranium forms continuous metallic network at the grain boundaries and eventually becomes the continuous phase[12, 14, 16-18]. Microstructure of this kind is not favourable from radiation stability aspect as undesirable characteristics of α -U e.g. an isotropy, dimensional instability, swelling, thermal cycling growth etc. start dominating[17]. Fine uranium dispersion in the microstructure helps in (a) depositing the fission fragments outside uranium matrix directly in the thorium matrix, (b) anchoring gas filled pores and (c) lowering gas diffusion rates due to high melting point of thorium[17-18]. Excellent radiation stability was observed in Th-($<20wt\%$)U alloys in irradiation studies, corroborating the above fact [19]. To increase fissile loading beyond 20wt% in Th-U alloys, uranium should be stabilised as isotropic γ -U phase. Hence, uranium needs to be alloyed with gamma stabilizers e.g. Mo, Zr, Nb etc. Farkas et al. have reported few preliminary studies on the ternary additions of Mo, Nb and Zr in Th-U binary alloys. Molybdenum is one of the best stabilisers of γ -U at room temperature[20-22]. The aim of these studies is to improve the irradiation resistance by stabilizing the γ -U phase as well as enhancing the high temperature strength of the alloy [17].

*Author for Correspondence: Raj Kumar
E-mail: rajk@barc.gov.in

In the present work, microstructural and diffraction studies on the Th-U-Mo alloys have been carried out. The structural studies were carried out using X-ray and neutron diffraction, and the quantitative estimation of γ -U phase in Th-U-Mo alloys was done using Rietveld method on polycrystalline samples.

Experimental Details

The starting materials for the preparation of Th-U and Th-U-Mo alloys were thorium finger, uranium and molybdenum slugs. Thorium finger was prepared by consolidating thorium powder which was obtained by calciothermic reduction of thorium followed by leaching. Molybdenum was obtained from M/s Midhani, Hyderabad, India. Uranium slugs of nuclear purity were obtained from AFD, BARC. Details of the starting material are given in Table 1.

Table 1: Details of the starting materials.

Material	Assay (wt%)	Oxygen (wt%)	Nitrogen (wt%)	Carbon (wt%)
Thorium powder	99.5	0.117 ± 0.012	0.0050 ± 0.0005	0.016 ± 0.001
Uranium	99.9	-	0.0140 ± 0.0010	0.010 ± 0.001
Molybdenum slugs	>99.9	-	-	-

Alloys were prepared by melting the constituents in water cooled copper hearth in a non-consumable arc melting set-up. The chamber was evacuated three times and back filled with high purity argon, before proceeding for melting of the alloys. Further, zirconium sponge was melted first, to consume residual oxygen and nitrogen present in the melting chamber. Alloys were then re-melted five times in arc melting setup under inert atmosphere each time turning the alloy piece upside down to ensure homogeneity of the constituents in the alloys. Molten alloys were suction cast in to 5 mm diameter cylindrical rods.

Carbon, oxygen and nitrogen content were also determined in addition to the assay content of the metals and alloys. The principle of inert gas fusion and thermal conductivity detection was used for the determination of nitrogen. The principle of combustion of sample followed by infrared (IR) detection was used for determination carbon. Oxygen was determined based on the principles of inert gas fusion and infrared (IR) detection.

Optical microstructures of the alloys were observed in an inverted optical microscope (M/s Olympus, Japan; Model: GX-51). Halogen light source (100W) was used in combination with light filters according to the requirement. Micrographs were captured using digital camera (M/s Olympus; Color View 1) attached to it. Optical images were obtained in bright field mode. Controlled oxidation of the alloys gave the best contrast in the optical microscopy.

Alloy samples were encapsulated in quartz tubes under vacuum of 10^{-3} mbar and then homogenized at 1000 °C (γ -U phase region) for 24 hours. One set of alloys was water quenched (WQ) and one set of alloys was allowed to cool inside the furnace itself, i.e., slow cooling (SC). Th-30U-2Mo and Th-30U-3Mo were subsequently aged at 500 °C below the eutectoid decomposition temperature of γ -U (580 °C).

Phase characterizations were done using an XRD unit with curved position sensitive detector (M/s INEL, France, Model: Equinox 3000) at 40kV and 30mA with Cu K_{α} (1.54056 Å) radiation. The diffractometer is calibrated using standard yttria sample.

Scanning electron microscope (SEM) having secondary electron detector (SE, Everhart Thornley) and back scattered electron detector (BSE) was used for electron microscopy. The energy dispersive spectroscopy with Si(Li) detector was employed for qualitative elemental mapping.

Neutron diffraction experiment was performed at Powder Diffractometer 2 (PD-2) at Dhruva research reactor, BARC. The wavelength of monochromatic neutrons was 1.2443 Å. Data collections were performed in Debye-Scherrer geometry in the 2θ range 6° - 135° with a step size of 0.1° . The air background was subtracted from the collected data prior to analysis. The alloy samples were in rod/plate form and the samples were mounted on a rotating stage to avoid the preferred orientation effects in the diffraction pattern. As neutrons can penetrate deep in the sample so the bulk samples can be studied which is advantageous in obtaining correct quantitative phase analysis.

Results and Discussion

Chemical Analysis of Thorium Metal and Alloy

Chemical analyses of the starting thorium metal and alloy used in the present study and that used by previous investigators are presented in Table 2. Both thorium and uranium have got strong affinity for carbon, nitrogen and

Table 2: Chemical Analysis Results of Thorium Metal & Alloy used in the Present Work and by Previous Investigators.

Element (wt%)		Th	U	Mo	O	C	N
Sample							
Present Study	Th metal finger	99.5 ± 0.1	-	-	0.139 ± 0.014	0.041 ± 0.004	0.03 ± 0.003
	Th-30U-3Mo	64.1 ± 0.1	33.2 ± 0.1	2.7 ± 0.1	0.179 ± 0.018	0.047 ± 0.004	0.045 ± 0.004
Previous reported work	Th metal and alloys	Bentle[23](1958)			0.131	0.040	0.008
					0.029	0.005	0.001
		Bannister et al.[24] (1964)			0.2 - 0.3	0.001 - 0.015	-
		Hayward et al.[25] (1958)			0.1379	0.06 - 0.07	-

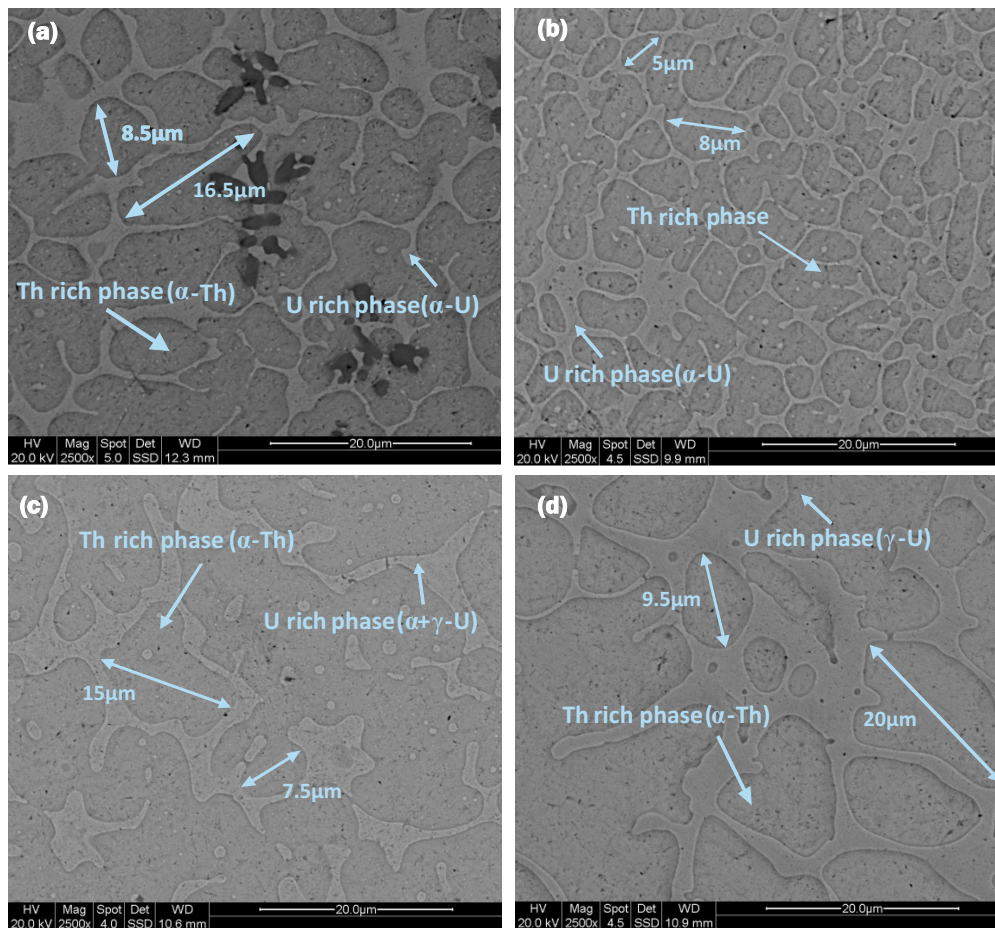


Fig.1: SEM Micrographs of the as-cast (a) Th-30U (b) Th-30U-1Mo (c) Th-30U-2Mo (d) Th-30U-3Mo.

oxygen. However, impurity content of this order does not have significant effect on the properties of thorium alloys. Carbon can significantly affect the mechanical properties of Thorium. Oxide inclusions as high as 3wt% do not seriously impair the mechanical fabrication. Homogeneity of the Th-U alloys depends on obtaining a reasonably fast cooling rate. Gravity segregation as well as carbon contamination from the graphite crucible are the major problems encountered in the induction melting of thorium. So, arc melting is better as it will offer faster cooling rate as well as the water-cooled copper crucible will avoid carbon contamination. The impurity content in the metal and alloys used in this study are comparable with that used by previous investigators.

Microstructures of the Alloys

The as-cast optical microstructures of the alloys are shown in Fig.1. The alloy microstructure is biphasic consisting of thorium rich and uranium rich phases. Interconnected network of uranium rich phase is present in a matrix of thorium rich phase. Uranium rich phase being the last to solidify, eventually solidifies in the grain boundary regions of the thorium rich phase and forms this kind of interconnected network upon solidification. The distribution of uranium in thorium matrix governs the irradiation behavior of Th-U alloys. Fine dispersion of uranium particles in the thorium matrix imparts dimensional stability and is favourable from fission gas retention point of view. Most of the fission fragments are deposited outside the uranium precipitate in the Th matrix and the fine dispersion of uranium particles helps to anchor the gas filled pores [13]. From the SEM images in Fig.1, it is quite evident that with addition of 1wt%Mo in the Th-30U alloy the grain structure becomes finer. With 2wt% Mo, however, the grain size increases and with further addition of 3wt% Mo the

grain size increases further. As the grain boundaries could not be revealed in all the grains, conventional grain size measurement techniques could not be employed to measure the grain size.

Composition of the Various Phases

The SEM-EDS analysis of the Th-U-Mo alloys is shown in Fig.2. The U-rich phase and Th-rich phase were identified. Mo has formed solid solution with uranium and Mo was not detected in the Th rich phase in all the alloys as seen in the EDS results. Molybdenum has got appreciable solid solubility in uranium but has negligible solid solubility in thorium [26-27]. In this case, molybdenum has distributed itself according to its solubility in the uranium rich phase and thorium rich phase. EDS results are in good agreement with the target composition. The overall alloy composition of the alloys has also been confirmed by XRF.

Heat Treatment of the Alloys

Heat treatment of the alloys was done to evaluate the stability of the microstructure and the various phases. Homogenization of the alloys was done at 1000 °C for 24 hours to ensure homogeneous distribution of molybdenum and to rule out any instability of the γ -U phase due to inhomogeneous distribution of molybdenum. One set of alloy was allowed to be cooled in the furnace itself i.e. slow cooling (SC) and the other set of alloy was water quenched (WQ) i.e. fast cooling. Stabilization of γ -U phase in U-Mo alloys depends on the molybdenum content and the rate of cooling [28]. Microstructures of these alloys after homogenization treatment are shown in Fig.3. Networks of interconnected uranium formed at grain boundaries, became discrete in both

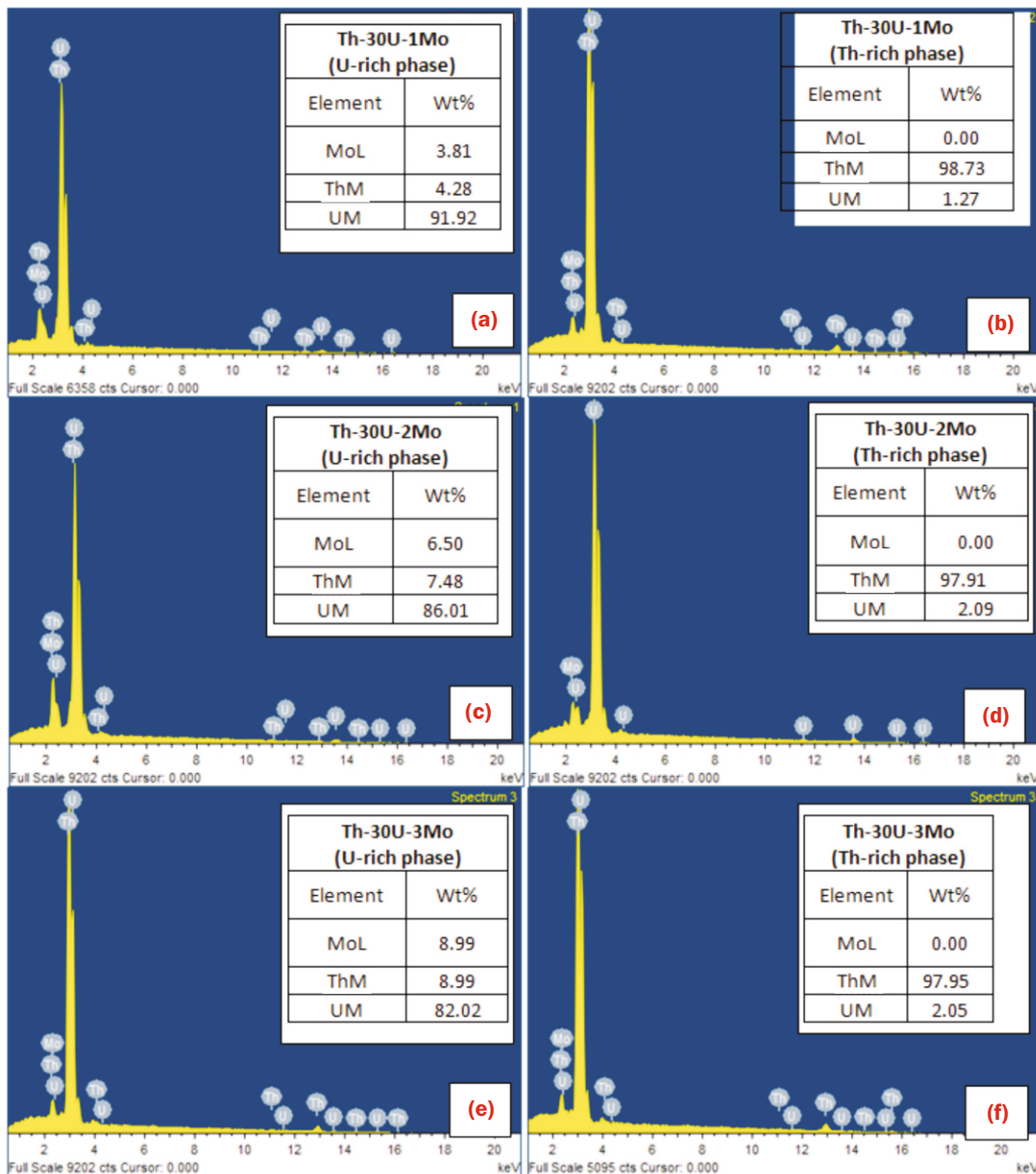


Fig.2: EDS of the alloys.

slow cooled as well as in water quenched condition. Dispersion of uranium in the form of globules from the interconnected network could be due to (i) minimization of surface energy and (ii) significant variation in the solid solubility of uranium in thorium with temperature. Studies by Bentley on the solid solubility of uranium in thorium from lattice parameter measurement has shown that solubility of uranium in thorium is less than 1 weight per cent at room temperature and increases to about 7 weight per cent at 1270 °C [26]. The increase in solubility of uranium at higher temperature possibly causes some amount of uranium to get dissolved in the thorium rich phase. This causes breaking of the interconnected network of uranium rich phase. While cooling, due to decrease in solubility, uranium reappears. Since everything is in solid state, smaller separated uranium globules are not able to coalesce with other particles and reappear as discrete globules. With faster cooling rate the globules are expected to be finer due to larger number of nucleation sites. Uranium dispersion was found to be finer under water quenched condition than that of slow cooled condition in the case of Th-30U-1Mo and Th-30U-2Mo alloys. However in case of Th-30U-3Mo, no major change in the microstructural features was observed, which needs further investigation.

Diffraction Studies

Room temperature x-ray and neutron diffraction patterns as shown in Fig.4 and Fig.5 confirms that γ -U phase is stabilized in Th-30U-2Mo and Th-30U-3Mo alloys. Th-30U and Th-30U-1Mo contained α -Th and α -U phases.

With higher molybdenum content the stability of the γ -U increases, which has been reported by several workers in binary U-Mo alloys [28-30]. The Th-30U-2Mo ternary alloy corresponds to a binary composition of U-6.25Mo.

With the addition of Mo in the system, the α -U changes to γ -U phase which exists in b.c.c. crystal structure and shows isotropic thermal expansion behaviour. With temperature the changes in the lattice are equal in all three directions and this is a desirable property to make nuclear fuel more stable. X-ray and neutron diffraction experiments were performed to quantify the phase fraction of γ -U with respect to Mo concentration.

a) Th-30U-3Mo: Neutron Diffraction

For Th-30U-3Mo system, most of the U was observed to be present in gamma phase. With incorporation of 3% Mo, complete γ -U phase stabilization was achieved.

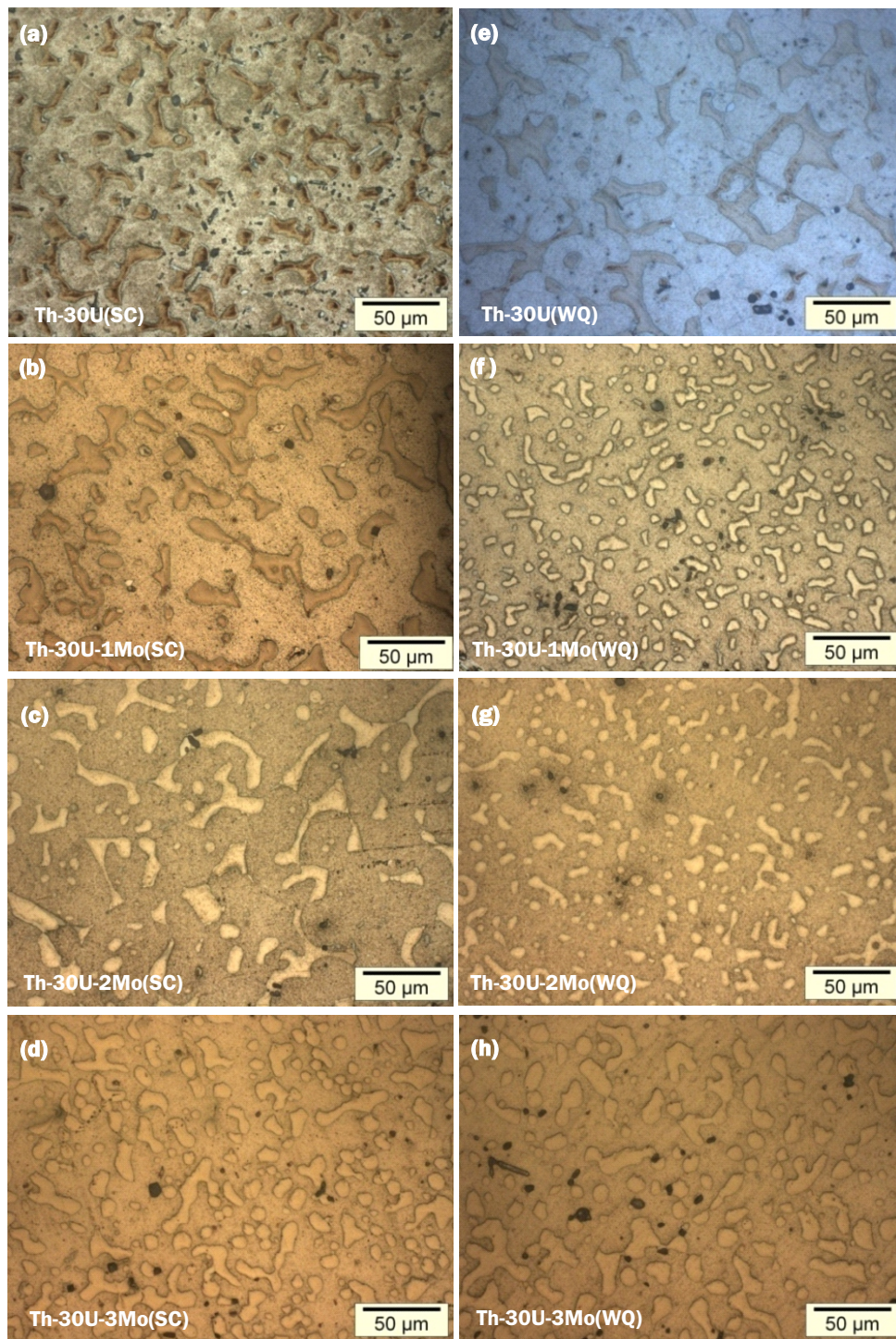


Fig.3: Optical Micrograph of Alloys Homogenised at 1000°C for 24 hours and slow cooled, SC (a-d) (a)Th-30U (b)Th-30U-1Mo (c)Th-30U-2Mo and (d) Th-30U-3Mo and water quenched, WQ (e-h)(e)Th-30U (f)Th-30U-1Mo (g)Th-30U-2Mo and (h) Th-30U-3Mo.

Table 3: Phase Fraction and Lattice Parameter data for Th-30U-3Mo (Neutron Diffraction) obtained by Rietveld method.

Weighted Average Bragg R-factor: 7.56

Rp: 4.46; Rwp: 5.63; Rexp: 3.39; Reduced Chi2: 2.75

b) Th-30U-3Mo: X-ray Diffraction

Weighted Average Bragg R-factor: 5.34

Rp: 11.5; Rwp: 14.7; Rexp: 9.55;

Reduced Chi2: 2.36

Phase	Space group	Phase fraction (%)	a (Å)	b (Å)	c (Å)	Angles
Th	F m - 3 m	68.28 ± 0.54	5.089(6)	5.089(6)	5.089(6)	$\alpha = 90^\circ;$ $\beta = 90^\circ; \gamma = 90^\circ$
U	I m - 3 m	28.56 ± 0.13	3.418(9)	3.418(9)	3.418(9)	$\alpha = 90^\circ;$ $\beta = 90^\circ; \gamma = 90^\circ$
ThO ₂	F m - 3 m	3.16 ± 0.01	5.600(7)	5.600(7)	5.600(7)	$\alpha = 90^\circ;$ $\beta = 90^\circ; \gamma = 90^\circ$

For Th-30U-3Mo system, different values of phase fraction and lattice parameter data for Th-30U-3Mo (X-ray diffraction) crystalline phase fraction was observed in X ray and neutron diffraction studies. As the oxidation of Th is more prominent on surface and Cu K- α X rays probe the high Z materials on the surface, so a larger fraction (15%) of ThO₂ phase was detected through XRD.

Whereas neutrons with comparatively larger penetration depth will give us the more accurate information of the bulk. From neutron diffraction the ThO₂ phase fraction was estimated to be around 3% and this is in agreement with chemical analytical techniques. The authors propose that for such materials, neutron diffraction can be utilized which is non-destructive in nature. The Rietveld refinement fits for X-ray and neutron diffraction data of Th-30U-3Mo are presented in Fig. 4.

c) Th-30U: X-ray Diffraction

Weighted Average Bragg R-factor: 12.39
Rp: 12.1; Rwp: 15.5; Rexp: 9.09; Reduced Chi2: 2.90

d) Th-30U-2Mo: X-ray Diffraction

Weighted Average Bragg R-factor: 11.54
Rp: 11.2; Rwp: 14.5; Rexp: 8.84; Reduced Chi2: 2.69

e) Th-30U-1Mo: X-ray Diffraction

Weighted Average Bragg R-factor: 7.38
Rp: 9.80; Rwp: 12.6; Rexp: 8.91; Reduced Chi2: 1.98

The Rietveld refinement fits for X-ray diffraction data of the four alloy samples is presented in Fig. 5. In Th-U-Mo alloys, γ -U phase fraction in Th-U-Mo alloys is found to increase with increase in the concentration of molybdenum, which is depicted in Fig. 6.

Summary and Conclusion

1. The microstructures of the binary Th-30U as well as the ternary Th-30U-Mo alloys show interconnected networks of U rich phase at the grain boundaries. With 1wt% Mo addition in the Th-30U alloy the grain structure becomes finer. However, with addition of 2wt% and 3wt% Mo progressive increase in grain size was observed.

2. From the SEM-EDS analysis it was seen that all the molybdenum has formed solid solution with the

Table 4: Phase fraction and lattice parameter data for Th-30U-3Mo (X-ray diffraction) obtained by Rietveld method.

Phase	Space group	Phase fraction (%)	a (Å)	b (Å)	c (Å)	Angles
Th	F m - 3 m	56.13 ± 1.74	5.066(9)	5.066(9)	5.066(9)	$\alpha = 90^\circ;$ $\beta = 90^\circ; \gamma = 90^\circ$
γ - U	I m - 3 m	28.30 ± 1.19	3.425(6)	3.425(6)	3.425(6)	$\alpha = 90^\circ;$ $\beta = 90^\circ; \gamma = 90^\circ$
ThO ₂	F m - 3 m	15.12 ± 1.46	5.577(13)	5.577(13)	5.577(13)	$\alpha = 90^\circ;$ $\beta = 90^\circ; \gamma = 90^\circ$

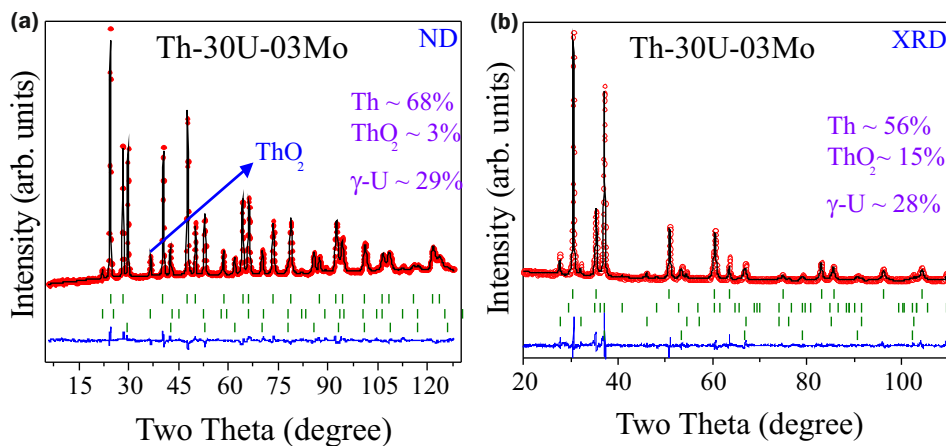


Fig.4: Rietveld refinement fit of Th-30U-3Mo sample : (a) Neutron Diffraction (b) X-ray Diffraction.

Table 5: Phase fraction and lattice parameter data for Th-30U (X-ray diffraction) obtained by Rietveld method.

Phase	Space group	Phase fraction (%)	a (Å)	b (Å)	c (Å)	Angles
Th	F m - 3 m	74.69 ± 3.01	5.086(14)	5.086(14)	5.086(14)	$\alpha = 90^\circ;$ $\beta = 90^\circ; \gamma = 90^\circ$
α - U	C m c m	23.73 ± 1.03	2.851(12)	5.875(12)	4.949(7)	$\alpha = 90^\circ;$ $\beta = 90^\circ; \gamma = 90^\circ$
ThO ₂	F m - 3 m	1.58 ± 0.35	5.592(8)	5.592(8)	5.592(8)	$\alpha = 90^\circ;$ $\beta = 90^\circ; \gamma = 90^\circ$

Table 6 : Phase fraction and lattice parameter data for Th-30U-2Mo (X-ray diffraction) obtained by Rietveld method.

Phase	Space group	Phase fraction (%)	a (Å)	b (Å)	c (Å)	Angles
Th	F m - 3 m	76.78 ± 2.38	5.085(5)	5.085(5)	5.085(5)	$\alpha = 90^\circ;$ $\beta = 90^\circ; \gamma = 90^\circ$
α - U	C m c m	11.90 ± 2.20	2.839(6)	6.054(8)	4.842(10)	$\alpha = 90^\circ;$ $\beta = 90^\circ; \gamma = 90^\circ$
ThO ₂	F m - 3 m	1.25 ± 0.29	5.576(7)	5.576(7)	5.576(7)	$\alpha = 90^\circ;$ $\beta = 90^\circ; \gamma = 90^\circ$
γ - U	I m - 3 m	10.08 ± 0.70	3.419(4)	3.419(4)	3.419(4)	$\alpha = 90^\circ;$ $\beta = 90^\circ; \gamma = 90^\circ$

uranium and negligible Mo was detected in the Th rich phase. The Mo concentration obtained as per the EDS results is in good agreement with the target alloy compositions.

3. It was observed that after the homogenization treatment at 1000 °C for 24 hours, the interconnected networks of the uranium formed at grain boundaries become discrete, which is favourable from irradiation stability point of view.

4. The microstructure and phase composition of Th-30U-3Mo alloy were observed to be quite stable after ageing at 500 °C for up to one month.

5. From the diffraction studies and Rietveld refinement, it is concluded that in Th-30U-2Mo, γ -U phase has been partially stabilized and in Th-30U-3Mo, it has been fully stabilized at room temperature. It has also been observed that for the quantification of thorium oxide phase, neutron diffraction is better than x-ray diffraction.

6. Th-30U-3Mo in as cast condition consists of uranium in isotropic gamma phase and is likely to be better than the corresponding binary Th-U as well as the other low Mo alloys provided other relevant parameters are evaluated and found favourable.

References

[1] G.L. Hofman, L.C. Walters, Metallic fast reactor fuels, Mater. Sci. Technol., 1994, 10A, 3.

[2] S. Das, et al., Characterisation of microstructural, mechanical and thermophysical properties of Th-52U alloy, J. Nucl. Mater., 2016, 480, 223-234.

[3] S. Das, et al., Characterisation of microstructural, mechanical and thermal properties and ageing study of the Th-3wt%U alloy, Nucl. Eng. Des. 282 (2015) 116-125.

[4] N. Clavier, R. Podor, L. Deliere, J. Ravoux, N. Dacheux. Combining in situ HT-ESEM observations and dilatometry: an original and fast way to the sintering map of ThO₂. Mater. Chem. Phys., 2013, 137, 3, 742-749.

[5] N. Hingant, N. Clavier, N., Dacheux, S. Hubert, N. Barre, R. Podor, L. Aranda, Preparation of morphology controlled Th_{1-x}U_xO₂ sintered pellets from low temperature precursors, Powder

Table 7 : Phase fraction and lattice parameter data for Th-30U-1Mo (X-ray diffraction) obtained by Rietveld method.

Phase	Space group	Phase fraction (%)	a (Å)	b (Å)	c (Å)	Angles
Th	F m - 3 m	77.48 ± 2.23	5.073(6)	5.073(6)	5.073(6)	$\alpha = 90^\circ$; $\beta = 90^\circ$; $\gamma = 90^\circ$
α -U	C m c m	8.59 ± 0.66	2.855(9)	5.952(5)	4.962(3)	$\alpha = 90^\circ$; $\beta = 90^\circ$; $\gamma = 90^\circ$
ThO ₂	F m - 3 m	13.93 ± 1.17	5.582(5)	5.582(5)	5.582(5)	$\alpha = 90^\circ$; $\beta = 90^\circ$; $\gamma = 90^\circ$

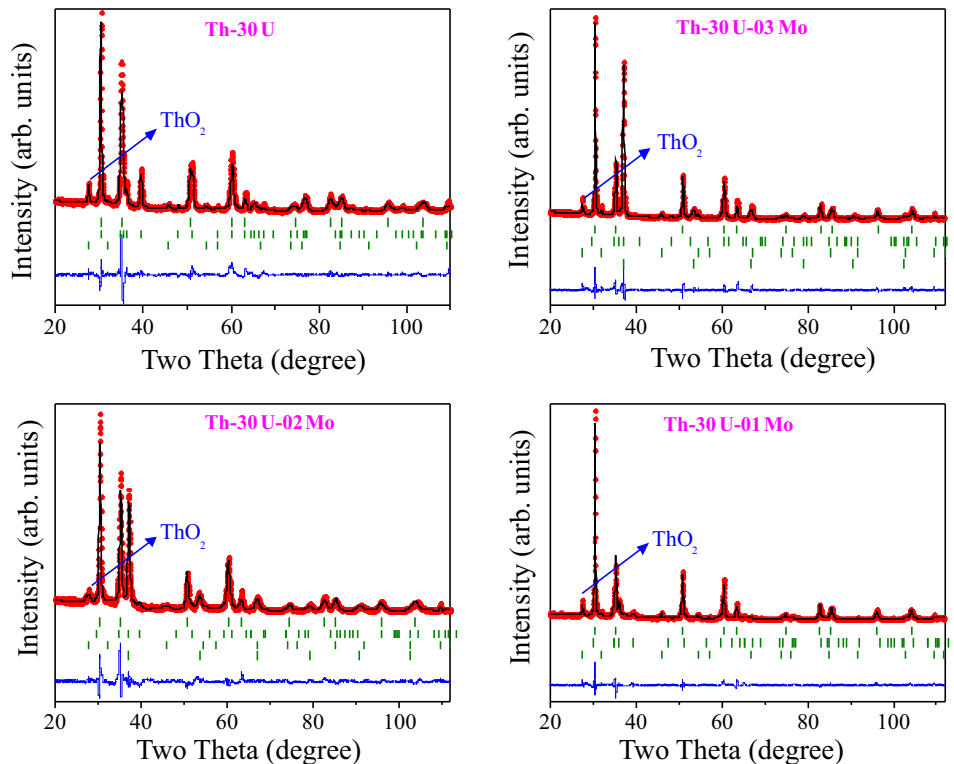


Fig.5: Rietveld refinement fit of Th-30U-Mo alloy samples : X-ray Diffraction.

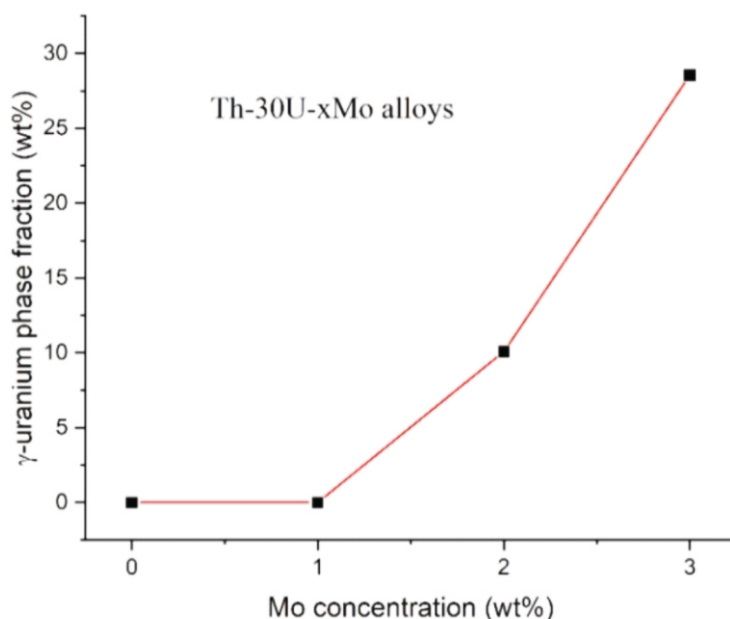


Fig.6: γ -U phase fraction in Th-30U-Mo alloy samples with respect to Mo concentration.

Technol., 2011, 208, 2, 454–460.

[6] W.J. Carmack, D.L. Porter, Y.I. Chang, S.L. Hayes, M.K. Meyer, D.E. Burkes, C.B. Lee, T. Mizuno, F. Delage, J. Somers, Metallic fuels for advanced reactors. *J. Nucl. Mater.*, 2009, 392, 2, 139–150.

[7] S. Kaity, J. Banerjee, M.R. Nair, K. Ravi, S. Dash, T.R.G. Kutty, A. Kumar R.P. Singh. Microstructural and thermophysical properties of U-6wt%Zr alloy for fast reactor application. *J. Nucl. Mater.*, 2012, 427, 1–11.

[8] O. Benes, D. Manara, R.J.M. Kornings. Thermodynamic assessment of the Th-U-Pu system. *J. Nucl. Mater.*, 2014, 449, 15–22.

[9] IAEA, Status and Trends of Nuclear Fuels for Sodium Cooled Fast Reactors, IAEA, Vienna, 2011.

[10] J.H. Kittel, J.A. Horak, W.F. Murphy, S.H. Paine, Effects of Irradiation on Thorium and Thorium-Uranium Alloys, USAEC, A N L - 4574, 1963.

[11] S. Das, S. Kaity, R. Kumar, J. Banerjee, S.B. Roy, G.P. Chaudhari, B.S.S. Daniel, Determination of Room Temperature Thermal Conductivity of Thorium-Uranium Alloys. In *Thorium—Energy for the Future*. Springer, Singapore, 2019, 277–286.

[12] S. Das, S.B. Roy, G.P. Chaudhari, B.S.S. Daniel, Microstructural evolution of as-cast Th-U alloys, *Prog. Nucl. Energy*, 2016, 88, 285–296.

[13] Thorium Fuel Cycle-Potential Benefits and Challenges, IAEA, Vienna, 2005. IAEA-TECDOC-1450 ISSN1011-4289.

[14] R. Kumar, S. Das, S.B. Roy, R. Agarwal, J. Banerjee, & S.K. Satpati, Effect of Mo addition on the microstructural evolution and γ -U stability in Th-U alloys. *Journal of Nuclear Materials*, 2020, 539, 152317.

[15] P. Rodriguez and C. V. Sundaram, Nuclear and Material Aspects of The Thorium Fuel Cycle, *Journal of Nuclear Materials*, 1981, 100 227–249.

[16] G.L. Copeland, Evaluation of thorium-uranium alloys for the unclad metal breeder reactor, ORNL, Oak Ridge, ORNL-4557, 1970.

[17] M.S. Farkas, A.A. Bauer, R.F. Dickerson, Development of Th-U Base Fuel Alloys, BMI, Ohio, 1960, BMI-1428.

[18] A.E. Walter, D.R. Todd, P.V. Tsvetkov, *Fast Spectrum Reactors*, 14419957 14th ed., Springer Science Business Media LLC, USA, 2012.

[19] J.H. Kittel, J.A. Horak, W.F. Murphy, J.H. Paine, Effects of Irradiation on Thorium and Thorium Alloys, ANL, Illinois, 1963, A N L - 5674.

[20] R. Prabhakaran, D.E. Burkes, D.M. Wachs, J.I. Cole, I. Charit, Small Scale Specimen Testing of Monolithic U-Mo Fuel Foils, Idaho National Laboratory, Washington, D.C, RERTR, 2008, Meeting INL/CON-08-14612.

[21] A. Landa, P. Soderlind, P.E.A. Turchi, Density Functional Study of U-Mo and UZr Alloys, Lawrence Livermore National Laboratory, US, 2010, LLNL-JRNL-461538.

[22] S. Jana, et al., Kinetics of cellular transformation and competing precipitation mechanisms during sub-eutectoid annealing of U10Mo alloys, *J. Alloys Compd.*, 2017, 723, 757–771.

[23] G.G. Bentle, Study of the Thorium-Uranium alloy system, in: IAEA Conference Paper, Geneva, 1958, pp. 706.

[24] G.H. Bannister, J.R. Thomson, The bcc to fcc phase transformation in thorium and some thorium rich alloys, *J. Nucl. Mater.*, 1964, 12, 1, 16–23.

[25] B.R. Hayward, P. Corzine, Thorium-uranium fuel elements for SRE, in: 2nd International Conference on the Peaceful Uses of Atomic Energy, Geneva, 1958, pp. 785.

[26] M.A. Steiner, E. Garlea, S.R. Agnew, Modeling solute segregation during the solidification of γ -phase U-Mo alloys, *J. Nucl. Mater.*, 2016, 474, 105–112.

[27] O.D. McMasters, P.E. Palmer, W.L. Larsen, Th-Mo Phase diagram, *J. Nucl. Mater.*, 1964, 7, 3, 151–156.

[28] S. Neogy, et al., Microstructural study of gamma phase stability in U-9wt%Mo alloy, *J. Nucl. Mater.*, 2012, 422, 77–85.

[29] J.P. Hammond, Review of information on U-Mo alloys and U-Mo-UO₂ dispersion fuels, ORNL, ORNL60-6-L22, 1960.

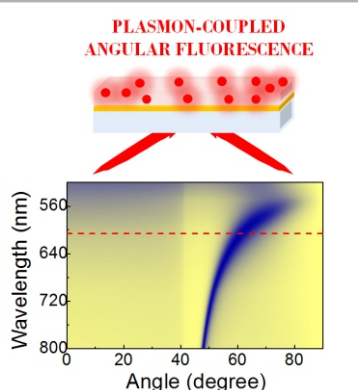
[30] N.-T.H. Kim-Ngan, I. Tkatch, S. Maskova, A.P. Goncalves, L. Havela, Study of decomposition and stabilisation of splat-cooled cubic gamma phase U-Mo alloys, *J. Alloys Compd.*, 2013, 580, 223–231.

Fluorescence based Techniques

Studies on Surface Plasmon Coupled Fluorescence With a Custom-made Optical Setup for Measuring Angle-resolved Emission Spectra

S. Dutta Choudhury*

Radiation & Photochemistry Division,
Bhabha Atomic Research Centre, Mumbai-400085, INDIA
Homi Bhabha National Institute, Anushaktinagar, Mumbai 400094, INDIA



Plasmon-coupled angular fluorescence

ABSTRACT

Many applications in the chemical and biochemical sciences, like, sensing, imaging, or medical diagnostics, rely on fluorescence-based techniques. During the past decade, it has been realised that the near-field coupling of fluorescence with surface electromagnetic waves and guided electromagnetic modes in suitably designed plasmonic or photonic substrates can lead to interesting effects such as, increased brightness, collimation of the emission over a narrow angular range, colour routing, and selective emission polarization. Understanding these phenomena is of immense interest for improving the scope of fluorescence in practical applications. As the commercially available fluorescence spectrometers are not suitable for carrying out studies on plasmonic or photonic substrate coupled emission, a simple home built optical setup has been developed in Radiation & Photochemistry Division, BARC, which is compatible for investigations on surface wave coupled emission. In this setup, the excitation can be carried out in both the Kretschmann as well as the reverse Kretschmann configurations, and emission spectra can be recorded over a wide range of angles (~ 0 - 360°). This article describes the newly developed setup, as well as the observation of angle and polarization-resolved emission from fluorescent dyes that are coupled with surface plasmons and guided electromagnetic modes on Ag and Au thin film substrates.

KEYWORDS: Fluorescence, Surface plasmon, Kretschmann, Reverse Kretschmann, Directional emission

Introduction

Fluorescence is the phenomenon of light emission due to radiative relaxation of electronically excited species from their first singlet state to the ground state [1,2]. It is widely used in chemical sensing, optical devices, microscope imaging, biological research, and medical diagnosis. Traditional fluorescence applications rely on the spontaneous emission of fluorophores in an optically transparent medium and detection of emitted light in the far-field. In homogeneous solutions fluorescence is omnidirectional. Accordingly, conventional fluorescence spectrometers are designed to collect the emitted light perpendicular to the angle of excitation to avoid interference from the excitation source. This arrangement can typically collect about 1% of the total emitted light [3]. Novel methodologies are thus very much desirable to increase fluorescence collection efficiencies. The conversion of the usual isotropic emission into collimated emission over a narrow angular range that can be directly focused into the fluorescence detector is conceived to be one of the possible approaches. Directional emission is also desirable for optical devices, communications and single molecule detection [4,5].

The technique of surface enhanced fluorescence provides interesting opportunities for improvements in

fluorescence detection efficiency through modification and control of the local electromagnetic environment in the vicinity of the emitter [3,6,7]. Different kinds of plasmonic nanostructures are investigated as nanoantennas for directional light scattering and emission [8-12]. The nanoantennas basically act as transducers between far- and near-field light signals. Some varieties of plasmonic nanostructures that have been studied include Au V-antennas, aperture antennas, Yagi-Uda nanoantennas, Ag/Au nanowire junctions and nanohole arrays. The localized surface plasmon resonances that arise from the nonpropagating collective oscillations of free charge carriers in metal nanoparticles, and the propagating surface plasmons in metallic nanowires, nanoslits, and nanogaps, enable confinement of light in the nanoscale region and realization of directional light emission [8-12]. Compared to plasmonic nanostructures, dielectric nanostructures show very low dissipative loss and are emerging as an alternative approach for light manipulation at nanoscale [13].

Apart from the nanoantenna structures, large area planar plasmonic and dielectric structures, that support surface waves or internal electromagnetic modes, are also capable of influencing the spontaneous emission rate and the angular patterns of emission by modifying the fluorophore surroundings [14-20]. The most commonly investigated structures in this regard are, thin metal films (mostly of Ag and

*Author for Correspondence: S. Dutta Choudhury
E-mail: sharmidc@barc.gov.in

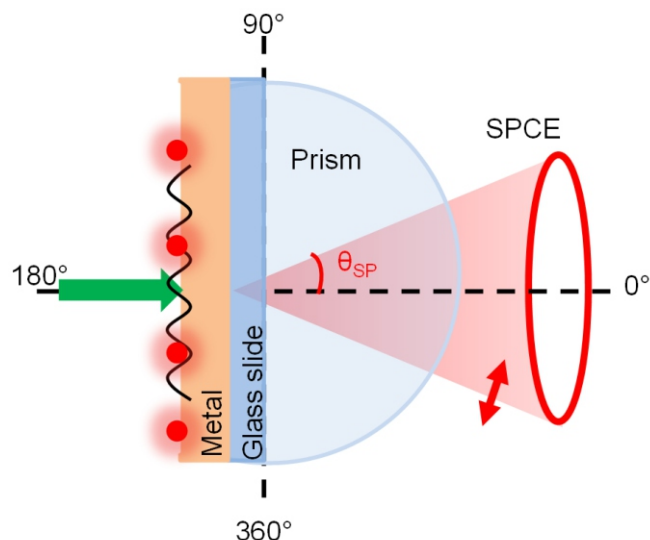


Fig.1: Schematic of surface plasmon coupled emission (SPCE) from fluorophores on a thin metal film (Ag/Au). The fluorophores (shown as red spheres) are directly excited from the air side (Reverse Kretschmann configuration). The fluorescence couples with surface plasmons on the metal/dielectric interface and appears toward the higher refractive index medium (prism side) as P-polarized emission at a characteristic angle (θ_{SP}).

Au) that support surface plasmon polaritons, 1D photonic crystals that support Bloch surface waves, and hybrid metal film/photonic crystal structures that can support Tamm plasmon polaritons.¹⁴⁻²⁰

Fig.1 shows a schematic representation of surface plasmon coupled emission (SPCE) for fluorophores placed on the surface of a thin metal film (Ag or Au) deposited on a glass slide. Excited fluorophores create surface plasmon oscillations on the metal film due to near-field interactions. The fluorescence couples with the plasmon mode, and radiates into the substrate at a characteristic angle, θ_{SP} , depending on the emission wavelength and the resonance condition of the surface plasmons. In order to extract the emission from the substrate, it is necessary to couple the substrate to a high refractive index medium like a glass prism, for wavevector matching [3,6,15]. In this schematic, the illumination geometry is in the Reverse Kretschmann (RK) configuration, where the fluorophores are excited directly by light incident from the air side. Alternatively, the fluorophores can also be excited by the evanescent field of the surface plasmons created by light incident through the glass prism at a definite angle that is proportional to the wavevector of the surface plasmon polaritons (Kretschmann configuration, KR) [3].

Since surface-plasmon resonance occurs exclusively for P-polarized light, it implies that SPCE is also P-polarized irrespective of the nature or orientation of fluorophores. Thus,



Fig.2: Optical setup for angle-resolved emission studies.

SPCE converts the isotropic fluorescence into a thin cone of P-polarized emission. SPCE has also been extended to include metal films coated with thick dielectric layers that support other electromagnetic waveguide modes in addition to the surface plasmon mode. This leads to the appearance of coupled emission at multiple angles, and with both S- and P-polarizations [21,22]. This article describes the SPCE from standard fluorescent dyes coupled to Ag and Au thin film substrates, recorded with the newly developed optical setup for angle-resolved emission studies in our laboratory.

Experimental Setup

The optical setup for recording angle-resolved emission spectra has been installed in room B-137, Mod Lab, RPCD (Fig.2). This custom made arrangement consists of a planoconvex cylindrical BK7 glass lens mounted on a height adjustable, precise rotational stage. The substrate containing the fluorescent material can be attached to the glass lens using a refractive index matching fluid. Excitation and observation of emission can be carried out at any angle relative to the vertical axis of the rotational stage. The emitted light after passing through suitable emission filters and polarizer, is collected with an optical fiber (core: 600 μm , NA: 0.22, wavelength: 400-2100 nm, from Ocean Optics) that is fixed on a holder at an adjustable distance from the substrate. The output of the fiber is connected to a miniature spectrometer (Ocean Optics, FLAME-S-XR1-ES, having wavelength range: 200-1025 nm, entrance slit: 50 μm , resolution (FWHM) \sim 2.0 nm), for recording the emission spectra. Analysis of the spectra is carried out with OceanView Cross platform spectroscopy operating software. Presently, the setup is equipped with two laser sources for excitation at 470 nm and 532 nm.

For the present SPCE studies, Ag and Au films (\sim 50 nm thick) were deposited on cleaned glass slides by vacuum evaporation. The surfaces of the films were then spin coated with poly vinyl alcohol (PVA) or poly methyl methacrylate (PMMA) solutions, containing the fluorescent dyes. The weight percent of PVA/PMMA in the solutions was varied to obtain PVA/PMMA films of different thicknesses. To correlate the observed emission patterns of the fluorophores with the surface plasmon mode and other waveguide modes present in the substrates, reflectivity calculations for the respective substrate geometries were carried out with TF Calc software package (Software Spectra, Inc., Portland, Oregon). The reflectivity plots correspond to energy conversion from far-field light to the optical modes present in the plasmonic structure, while the coupled emission is the conversion of near-field optical energy from the emitting molecules to the far-field, through these optical modes [4,23,24]. So essentially, the reflectivity plot simulates the expected angular distribution of the coupled emission.

SPCE with Au and Ag Thin Film Substrates

Fig.3A depicts the angle-dependent variation in the emission intensity of the fluorescent dye Nile Red embedded in a PMMA (0.5% PMMA) layer above an Au film deposited on glass slide. The excitation has been carried out in the RK configuration. The angular emission pattern shows that most of the emission from the fluorophore is channelized within a small angular range with the maximum at an angle of about 72° (and also 288° due to symmetry) from the normal. Furthermore, the emission is observed to be completely P-polarised. This is evident from the representative emission spectra of the dye (Fig.3B) recorded at an angle of 72°, but with two different orientations of the emission polarizer (S and P). The significantly weak fluorescence intensity of the dye when the polarizer is in the S-orientation clearly indicates

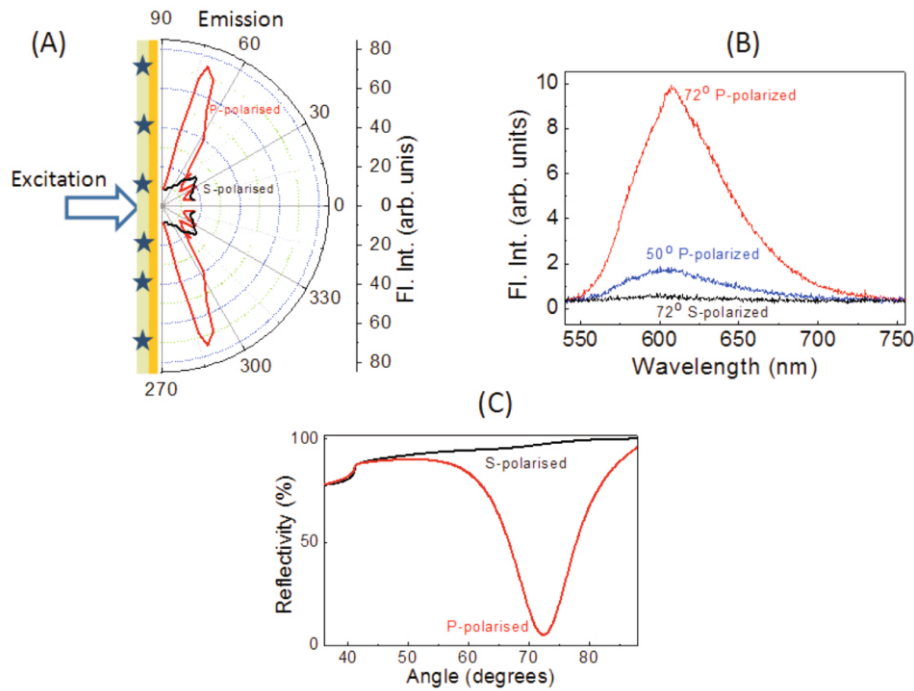


Fig.3: (A) Angular emission pattern of Nile Red on Au-PMMA substrate on excitation with a 532 nm laser; PMMA thickness ~70 nm. (B) Representative emission spectra of Nile Red on the Au-PMMA substrate at different angles and polarizer orientations. © Calculated reflectivity spectra for 605 nm light incident on the Au-PMMA substrate through a high refractive index medium (glass).

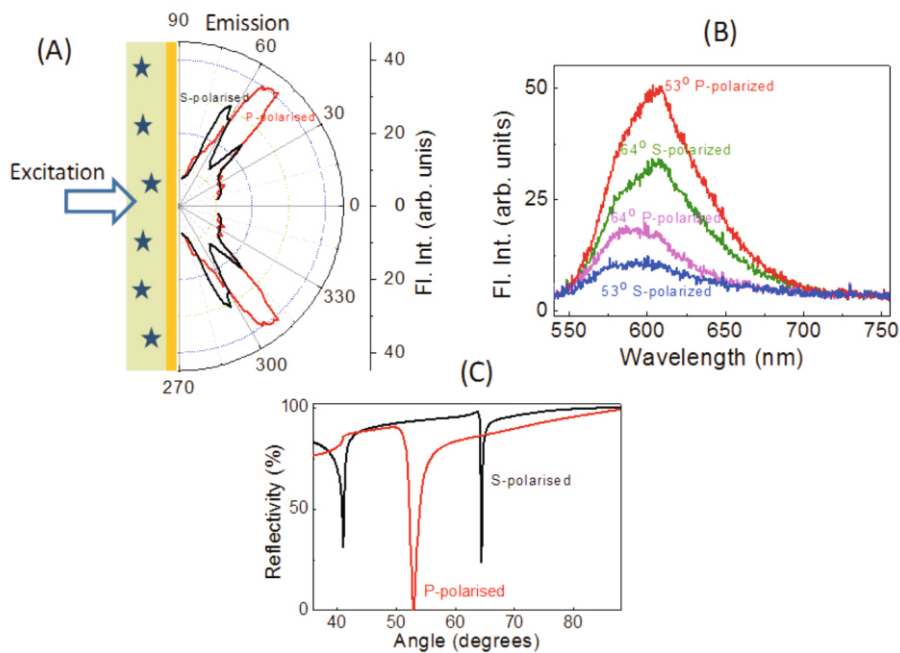


Fig.4: (A) Angular emission pattern of Nile Red coupled with Au-PMMA substrate, on excitation with a 532 nm laser; PMMA thickness ~375 nm. (B) Representative emission spectra of Nile Red on the Au-PMMA substrate at different angles and polarizer orientations. (C) Calculated reflectivity spectra for 605 nm light incident on the Au-PMMA substrate through a high refractive index medium (glass).

that the coupled emission from Nile Red is P-polarized. The emission spectra at two different angles (72° and 50°) are also shown in Fig.3B to highlight the variation in the emission intensity with respect to the observation angle. The appearance of P-polarized emission from Nile Red at specific angles is characteristic of the surface plasmon coupling effect. To further emphasize this aspect, the calculated reflectivity spectra of light having a wavelength of 605 nm (corresponding to the emission maximum of Nile Red) and incident on the Ag-PVA substrate at different angles through a high refractive index medium (glass) is shown in Fig.3C. A dip in the reflectivity is observed for a PMMA thickness of about 70 nm when the

incident angle is 72°. Further, the reflectivity dip appears for P-polarized light but not for S-polarized light. This suggests that incident light of wavelength 605 nm is capable of exciting surface plasmon oscillations in the Ag-PMMA substrate under certain incidence angle and polarization conditions. Accordingly, the emission from Nile Red dye (having emission maximum at 605 nm) that is coupled with the surface plasmon mode appears as P-polarized light at an angle of 72°.

The angular emission pattern of Nile red on the Au-PMMA substrate changes when the thickness of the PMMA layer is increased (Fig.4A). For a PMMA layer thickness of about 375 nm (2% PMMA solution), the P-polarized emission from Nile

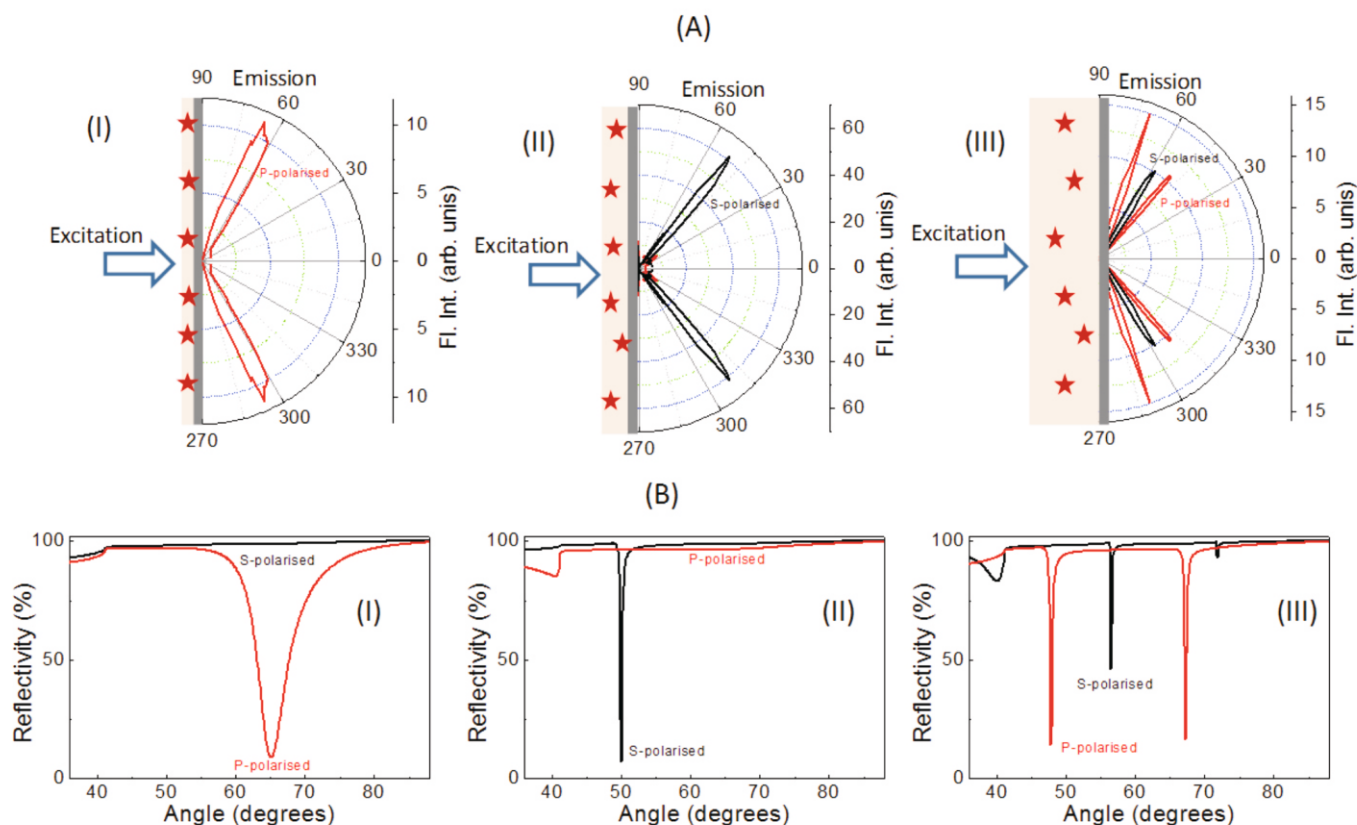


Fig.5: (A) Observed angular emission patterns of Fluorescein dye coupled with Ag-PVA substrates having different PVA thickness; excitation is with a 470 nm laser. (B) Calculated reflectivity spectra for 520 nm light incident on Ag-PVA substrates through a high refractive index medium (glass); PVA thicknesses are 50 nm (I), 160 nm (II) and 540 nm (III).

Red appears at have maximum intensity at an angle of 53° (and 307°), whereas the S-polarized emission appears to have maximum intensity at 42° and 64° (318° and 296°). The emission of Nile Red at multiple angles and having different polarizations arise due to the coupling of the fluorescence with the surface plasmon mode as well as the waveguide modes that are present in the Au-PMMA substrate with thick PMMA film. Representative emission spectra of Nile Red dye on the Au-PMMA substrates at different observation angles and polarizer orientations are depicted in Fig. 4B. The calculated reflectivity spectra (Fig. 4C) for 605 nm light incident on the Au-PMMA substrate with PMMA thickness of 375 nm shows reflectivity dips at 53° (for P-polarization), and around 42° and 64° for S-polarization) which nicely corresponds with the observed SPCE for Nile red on the studied substrate.

The observed angle-resolved emission patterns of the dye Fluorescein (emission maximum 520 nm) coupled with Ag-PVA substrates with different PVA thicknesses, on excitation with a 470 nm laser source are shown in Fig.5A. For PVA concentration $\sim 1.5\%$ w/v, the emission is completely P-polarized and appears at an angle of around 65° . When the PVA concentration is increased to 5% w/v, the emission from Fluorescein is completely S-polarized and appears at about 65° . With further increase in the PVA concentration to $\sim 7\%$ w/v, the emission from Fluorescein is channelized at multiple angles and with both S- and P-polarizations.

The experimentally observed results correlate well with the calculated reflectivity patterns (Fig.5B) for light having wavelength of 520 nm that is incident on Ag-PVA substrates having PVA thicknesses about 50 nm, 160 nm and 540 nm, respectively. This clearly suggests the occurrence of SPCE from the fluorescence in dyes coupled with the Ag-PVA substrates.

Overall, our study demonstrates the capability of the developed optical setup to measure angle and polarization resolved emission spectra of fluorophores coupled with different metal-dielectric layered substrates. Studies on SPCE are important not only for a fundamental understanding of light manipulation in the nanoscale but also for their prospects in efficient fluorescence sensing applications. The developed setup is compatible for fluorescence studies with many types of photonic and plasmonic substrates and can also be upgraded for fluorescence lifetime measurements.

Acknowledgements

I gratefully acknowledge the SERB Women Excellence Award Grant, SB/WEA-010/2013, that enabled me to initiate this work. I thank Dr. K. G. Girija, Chemistry Division, BARC, and Dr. S. Bhattacharya, TPD, BARC, for helping with the thin film depositions. I thank Dr. A. C. Bhasikuttan, Head, Molecular Photochemistry Section, Radiation & Photochemistry Division, BARC, Dr. A. Kumar, Head RPCD, BARC, and Dr. A. K. Tyagi, Associate Director, Chemistry Group, BARC, for their constant support and encouragement. I also thank Dr. P. D. Naik, Dean, HBNI, for his support in commencing this setup in our Division.

References

- [1] J. R. Lakowicz, Principles of Fluorescence Spectroscopy, Springer, 2006.
- [2] B. Valeur, Molecular Fluorescence: Principles and Applications, Wiley-VCH, 2001.
- [3] J.R. Lakowicz, Anal. Biochem., 2004, 324, 153.
- [4] S. Dutta Choudhury, R. Badugu, J. R. Lakowicz, Acc. Chem. Res., 2015, 48, 2171.

- [5] N. Li, Y. Lai, S. H. Lam, H. Bai, L. Shao, J. Wang, *Adv. Optical Mater.*, 2021, 9, 2001081.
- [6] E. Fort, S. Grésillon, *J. Phys. D: Appl. Phys.*, 2007, 41, 013001.
- [7] A. Sinibaldi, N. Danz, E. Descrovi, P. Munzert, U. Schulz, F. Sonntag, L. Dominici, F. Michelotti, *Sensors and Actuators B*, 2012, 174, 292.
- [8] H. Aouani, O. Mahboub, E. Devaux, H. Rigneault, T. W. Ebbesen, J. Wenger, *Nano Lett.*, 2011, 11, 2400.
- [9] A. Dasgupta, D. Singh, R. P. N. Tripathi, G. V. P. Kumar, *J. Phys. Chem. C*, 2016, 120, 17692.
- [10] V. Giannini, A. I. Fernandez-Dominguez, S. C. Heck, S. A. Maier, *Chem. Rev.*, 2011, 111, 3888.
- [11] Y. Wang, L. Wu, T. I. Wong, M. Bauch, Q. W. Zhang, J. L. Zhang, X. H. Liu, X. D. Zhou, P. Bai, J. Dostalek, B. Liedberg, *Nanoscale*, 2016, 8, 8008.
- [12] H. M. Shen, R. Y. Chou, Y. Y. Hui, Y. B. He, Y. Q. Cheng, H.-C. Chang, L. M. Tong, Q. H. Gong, G. W. Lu, *Laser Photonics Rev.*, 2016, 10, 647.
- [13] A. Vaskin, J. Bohn, K. E. Chong, T. Bucher, M. Zilk, D.-Y. Choi, D. N. Neshev, Y. S. Kivshar, T. Pertsch, I. Staude, *ACS Photonics*, 2018, 5, 1359.
- [14] J. A. Polo, A. Lakhtakia, *Laser Photonics Rev.*, 2011, 5, 234.
- [15] I. Gryczynski, J. Malicka, Z. Gryczynski, J. R. Lakowicz, *Anal. Biochem.*, 2004, 324, 170.
- [16] R. Badugu, K. Nowaczyk, E. Descrovi, J. R. Lakowicz, *Anal. Biochem.*, 2013, 442, 83.
- [17] S.-H. Cao, W.-P. Cai, Q. Liu, Y.-Q. Li, , *Annu. Rev. Anal. Chem.*, 2012, 5, 317.
- [18] R. Badugu, E. Descrovi, J. R. Lakowicz, *Anal. Biochem.*, 2014, 445, 1.
- [19] Y. Chen, D. Zhang, L. Zhu, Q. Fu, R. Wang, P. Wang, H. Ming, R. Badugu, J. R. Lakowicz, *Phys. Chem. Chem. Phys.*, 2014, 6, 25523.
- [20] S. Dutta Choudhury, Y. Xiang, D. Zhang, E. Descrovi, R. Badugu, J. R. Lakowicz, *J. Opt.*, 2021, 23, 035001.
- [21] I. Gryczynski, J. Malicka, K. Nowaczyk, Z. Gryczynski, J. R. Lakowicz, *J. Phys. Chem. B*, 2004, 108, 12073.
- [22] S. Dutta Choudhury, R. Badugu, K. Ray, J. R. Lakowicz, *Chem. Commun.*, 2014, 50, 9010.
- [23] J. Enderlein, T. Ruckstuhl, S. Seeger, *Appl. Opt.*, 1999, 38, 724.
- [24] N. Calander, *J. Phys. Chem. B.*, 2005, 109, 13957.

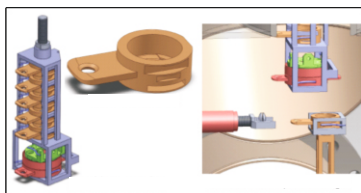
Automation

Remotely Operated UHV Compatible Sample Manipulator for Spectroscopy Synchrotron Beamline at Indus-2

A.D. Patil^{1*}, S. Bhatt¹, P.K. Biswas¹, R.K. Gupta¹, V. Bhardwaj¹, and S. Jagannath²

¹Center for Design and Manufacturing, Bhabha Atomic Research Centre, Mumbai-400085, INDIA

²Technical Physics Division, Bhabha Atomic Research Centre, Mumbai-400085, INDIA



Sample Cartridge, Picking tool and Magazine of the Sample Manipulator

ABSTRACT

Remotely operated UHV compatible Automated Precision Sample Manipulator assembly is an import substitute and has been developed indigenously for Angle Resolved Photo Emission Spectroscopy (ARPES) synchrotron beam-line (B.L.) at INDUS-2, RRCAT, Indore. Various samples, with the help of fully automated sequential mechanism can be loaded, transferred, coated and stored in a UHV (10^{-8} mbar) for further experimentation in Energy Analyzer of Beamline. Indigenous development of fully automated sample manipulator proved to be more compact and user friendly. Innovative design concepts are implemented for sample holding cartridge, sample picking adapter tool & cartridge magazine for precise pick up and transfer of the sample. The working principle, basic design features and remote operation of Sample Manipulator are discussed in this article.

KEYWORDS: UHV, Indus-2, Beamline, Automation, Precision Sample Manipulator Assembly, Energy Analyzer, Hybrid manipulators

Introduction

Remotely operated UHV compatible Sample Manipulator is one of the critical equipment of ARPES beam-line of INDUS-2, Raja Ramanna Centre for Advanced Technology (RRCAT). It is developed indigenously to prepare samples for ARPES experiments. ARPES is “Angle Resolved Photo Emission Spectroscopy” in which synchrotron radiation is focused on the sample inside the Toroidal Analyzer to study energy and momentum distribution of photo electrons. It is an import substitute for the scientific instruments such as imported thin film deposition manipulator by SVTA Associates, USA, Analytical & preparation manipulator by PREVAC, Poland, Toroidal spectrometer by La Trobe University, Australia.

Sample Manipulator is a fully automated sequential mechanism to load the sample, transferring the sample, coating the sample and storing it in a magazine inside the UHV (10^{-8} mbar) to pick it up as and when required for spectroscopy in the analyzer.

The assembly consist of load lock chamber, sample preparation chamber, stacking chamber, and manipulators for loading/unloading, pick up and transferring the sample. Manipulators are magnetic coupler remotely operated feed-throughs to actuate desired movements.

Prepared Sample is comprises of substrate material with coating of material to be analyzed for ARPES study. Substrate of glass, stainless steel or Si crystal of size 10 x 10 x 1mm thick will be used as base material and then coated with material of U, Ti, Zr etc. as thin film & single crystal for sample preparation.

Specifications of Sample Manipulator

- Fully automated transferring system
- Accommodate maximum 5 nos. of sample holders with maximum 5mm thickness
- Ultra High Vacuum (UHV: 10^{-8} mbar) compatible system
- Backlash free Magnetic coupler remotely operated feed-throughs manipulators
- Resolution: 2 microns
- Positional accuracy: 10 microns
- 7-axes manipulation for sample transfer (by 4 nos. of manipulators to feed motion from outside and 1 no. inside U H V chamber)

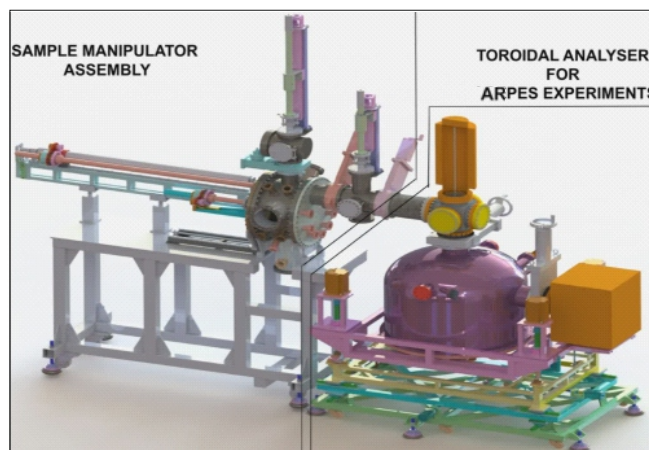


Fig.1: Sample Manipulator for ARPES B.L.

*Author for Correspondence: A.D. Patil
E-mail: adpatil@barc.gov.in

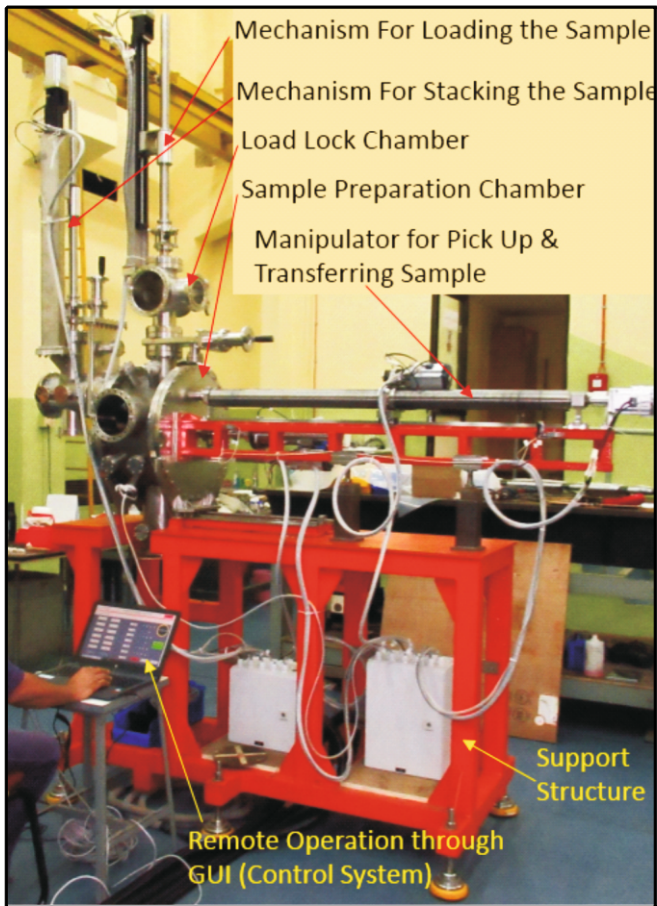


Fig.2: Sample Manipulator developed in CDM.

magazine inside the UHV compatible load lock chamber. The sample is then transferred to the preparation chamber by means of UHV compatible manipulator. It is then loaded on R-θ manipulator by means of transfer manipulator of the preparation chamber. By R-θ manipulator the sample can be radially as well as angularly positioned to respective ports of preparation chamber. Sample treatment, preparation and inspection are carried out inside the preparation chamber. Manipulator transfers and maneuvers the sample inside the preparation chamber for cleaning by Argon ion bombardment and then coating it with required ion deposition from respective gun port of preparation chamber. Quality checks are carried out by bringing the coated sample towards ports having requisite instruments. Prepared samples are then transferred and stored in cartridge magazine of stacking chamber for future use of spectroscopy inside the Toroidal analyzer. All the functions i.e. sample transfer, sample preparation and sample stacking are fully automated sequential operation and controlled through GUI based control system.

Design Features

Critical design features includes manipulation of sample at different stages, positional accuracy, sequential mechanism, UHV compatibility, remote operation & compactness of the equipment. Advanced UHV compatible remotely operated feed-throughs with linear as well as rotary mechanism are developed to manoeuvre samples inside the vacuum between predetermined stages. Such Hybrid manipulators are used in load lock chamber, preparation chamber and stacking chamber.

Innovative design is incorporated for holding sample cartridges, sample pick up adapter tool and cartridge magazine for precise maneuver of the sample. Cartridge magazine can house five sample cartridges and one thermal cartridge. It permits 1mm pick up and placement positional inaccuracy of sample cartridges inside magazine and is interchangeable.

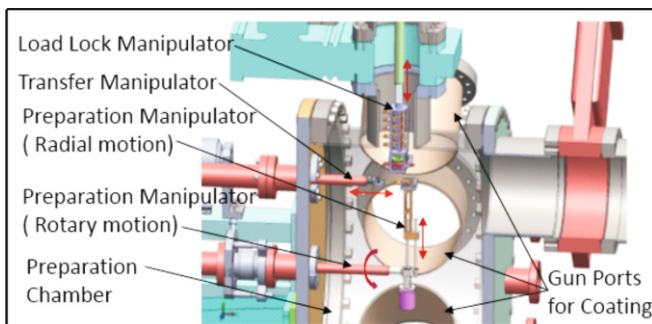


Fig.3: Sample manipulation carried using the manipulator.

- Manipulator-1 ('X' = 1200 mm & $\theta_x = 360^\circ$)
- Manipulator-2 ('X' = 300 mm & $\theta_x = 360^\circ$)
- Manipulator-3 ('Y' = 600 mm)
- Manipulator-4 ('Z' = 60mm- inside chamber)
- Manipulator-5 ('Y' = 600 mm)

- Interchangeability between sample holders
- Compact and user-friendly.

Sample Manipulator is a fully automated sequential mechanism to load the sample, transferring the sample, coating the sample and storing it in a magazine inside the UHV (10^{-8} mbar) to pick it up as and when required for spectroscopy in the analyzer.

Working Principle

Firstly samples substrates are arranged in cartridge

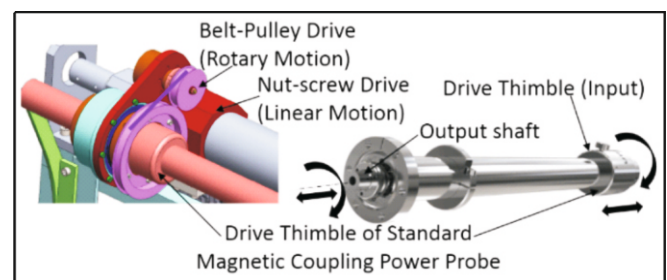


Fig.4: UHV compatible hybrid feed-throughs.

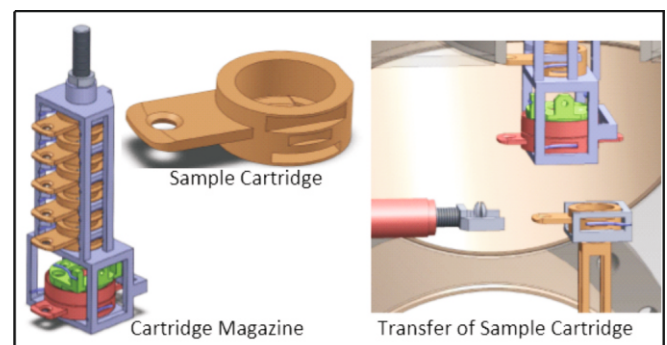


Fig.5: Sample cartridge, picking tool, Magazine.

GUI of control system will ensure sequential operation of hybrid manipulators with interlock between stages and also allows manual override or jog mode to bypass sequential stages.

Equipment Validation

The Sample manipulator assembly was manufactured with quality control and vacuum components were tested successfully for Helium leak test for allowable leak rate (10^{-9} mbarlit/sec). All the manipulators are individually tested

for functionality and positional accuracies of 10 microns. The system is then checked for errors cumulative in nature. The manipulators have been calibrated to achieve intended requirement of the system inside UHV of 10^{-8} mbar. Indigenously developed fully automated sample manipulator has proved to be more compact and user-friendly.

Bibliography

- [1] O&M of Toroidal spectrometer by La Trobe University, Australia.
- [2] Power probe manual by UHV Design, UK.

Civil Structures & Foundations

Special Design Considerations Applicable for Civil Structures and Foundations for Electrical Substations of Nuclear Facilities

Saha Dauji^{1,2} and Kapilesh Bhargava^{3,2,*}

¹Integrated Nuclear Recycle Plant-Equipment Design Division, Nuclear Recycle Board, Bhabha Atomic Research Centre, Mumbai-400085, INDIA

²Homi Bhabha National Institute, Anushaktinagar, Mumbai 400094, INDIA

³Engineering Services Group, Bhabha Atomic Research Centre, Mumbai-400085, INDIA



Typical Electrical Substation of a Nuclear Facility

ABSTRACT

Nuclear Fuel Cycle Facilities require electrical power from grid, and generally captive substations are preferred to distribute and/or step down the supply to the specific requirements of the plants. Though made of structural steel, the design considerations for these structures are different from the regular industrial steel structures. Several considerations are derived from the provisions of transmission line towers, though the sub-station structures are relatively simple. This paper discusses the general and special considerations for substation structures for ready reference of practicing engineers.

KEYWORDS: Substation structures, Steel structures, Foundation

Introduction

All large industrial installations require electrical power and the nuclear fuel cycle facilities (NFCF) are no exception. The power for NFCF is tapped from nearby grids, and subsequently distributed and/or stepped down for the specific needs of the industrial plant. Generally captive substations are preferred for NFCF, a typical example depicted in Fig. 1. This would consist of one or more transformers (generally two parallel lines are preferred for redundancy), potential transformer, current transformer, along with protective items such as circuit breakers and lightning arrestors. The aforementioned electrical equipment would require structural supporting system and traditionally substation structural supports are provided with a combination of concrete and structural steel. The loads from the electrical equipment and electrical lines (wire/cables) are transferred to the supporting structures at various levels, and the support configuration has to be accordingly designed, sometimes with provisions of future expansion. These structures could include trussed towers (similar to electrical transmission towers, but smaller in height) for supporting conductors/insulators/ground wires and/or beams; trusses beams (between towers) for supporting conductors/insulators/ground wires; and other smaller trussed supports for the equipment. Thus the configurations of these steel structures differ from the conventional industrial steel structures.

Owing to the special nature of functionality, the provisions for analysis and design of substation structures are different from the regular conventional/industrial steel structures, and the design provisions for the foundations are also slightly typical for substations. Therefore, though simpler than the

transmission line towers, the analysis and design of substation structures are performed in line with those of the transmission towers. The design provisions of transmission line towers are quite different from conventional industrial steel structures and therefore, entail different Indian design codes. The differences primarily occur due to the nature of load and therefore the loading calculations for substation structures are also different. There are some special provisions for the design conditions of transmission line towers which include reliability, security and safety considerations for all types of loads. Needless to mention that as a result of the differences in loading definition and design considerations, the load combinations applicable for the substation structures are different from the conventional industrial steel structures.

A brief note was presented earlier [1]. This article presents an expanded version and highlights the salient features for analysis and design of civil structures and foundations for substations. The information presented here would be useful as introduction to civil engineers involved in design and construction of substation structures and foundations.

Components of Substation Structures

The typical components of an electrical substation would include the following:

- Main Towers and Main Beams (MT / MB);
- Current Transformer structure (CT);
- Potential Transformer structure (PT);
- Lightning Arrester structure (LA);
- Bus Post Insulator structure (BPI);
- Circuit breaker (CB);

*Author for Correspondence: Kapilesh Bhargava
E-mail: kapil_66@barc.gov.in



Fig.1: Some components of a typical electrical substation.

Other structures such as fire wall, diesel storage tank, cable trenches, transformer oil tank & burnt oil tank (depending on the type of equipment).

The photograph in Fig. 1 depicts some salient structures of a typical electrical substation.

Applicable Indian Codes

The substation structures are generally made of structural steel, with concrete foundations. These steel structures consist of trusses – in the form of towers or beams, grids, or simple vertical supports. However, the analysis and design of these steel structures differ from the conventional/industrial steel structures and require some special design provisions. Particularly, there are differences in the imposed loading coming on the structure (specifically the load/s from the conductors, insulators, ground wires etc.), load combinations, and design considerations. Actually, the materials and loads for substation structures would be in line with the transmission tower requirements, and would be according to IS 802 (Part 1 / Sec 1) [2]; similarly, the design provisions are provided in IS 802 (Part 1 / Sec 2) [3]; and the foundation design and construction would be according to IS 4091 [4], for which a revision is under process [5]. But of course, the substation structures, even the tower-beam systems, would be much simpler in arrangement, analysis and design as compared to the transmission towers owing to the limited plan area covered by substation(s) as well as the generally orthogonal orientation of the conductors/ground wires/etc. in the substation enclosure.

It may be hereby noted that for other general provisions for concrete, steel, and foundation design and construction those are not covered in the aforementioned codes, the appropriate Indian standards would be applicable. For example, the steel design would be governed by IS 800 [6] and the concrete design would be governed by IS 456 [7].

Statutory Requirements for Substation Structures

A significant difference in substation steel structures from conventional/industrial design would be that in addition to the aforementioned codes, there are statutory requirements to be

fulfilled for sub-station structures, as enumerated in the prevalent latest version of the code [1], including the following:

- Indian Electricity Rules, 2005;
- Local and provincial byelaws;
- Fire and safety laws including IS 5613 [8];
- Civil aviation requirements/electricity rules;

Special Design Requirements for Substation Structures

The calculation of the various loads, both transverse and longitudinal, needs to fulfill three design requirements:

* **Reliability Requirements:** There are three Reliability levels specified in the code [2], according to which the structures should be analyzed and designed.

- *Reliability level 1:* This is adopted for lines up to 400 kV class, and corresponds to a return period of loads equal to 50 years;
- *Reliability level 2:* This is adopted for lines above 400 kV class, and corresponds to a return period of loads equal to 150 years;
- *Reliability level 3:* This is adopted for special lines or for river crossing cases, and corresponds to a return period of loads equal to 500 years.

Guidelines for determination of loads and the combinations for Reliability levels 1 and 2 are stipulated in the code [2]. However, this code [2] does not cover the requirements pertaining to the analysis for *Reliability level 3*.

* **Security Requirements:** There are two categories of Security requirements specified in the code [1] for loading and analysis of these structures.

- Security requirements under *Broken Wire conditions*;
- Security requirements under *Narrow Front Wind conditions*;

* **Safety Requirements:** These requirements arise from the operation and maintenance loading on the structures, which might be incidental and transient in nature. The code [2]

stipulates the various loads and their points of application for different members supporting various types of wires (conductor/insulator/ground wire/etc.), for *Normal* and *Broken Wire* conditions.

Typical Loads for Substation Structures

The loads coming on the substation structures are analyzed in three major categories, according to the special design requirements discussed in the preceding section, and these are elaborated below.

* **Gravity loads:** This is the most basic load on any structure and includes the self-weight of the tower/ beam/components of the structure along with the additional weight of the cables/wires/conductors/etc. applied at the respective nodes of the structure.

* **Climatic loads:** The climatic loads considered for substation structures are related to the reliability requirement of the structure. The major types of climatic loads would be:

- **Wind loads:** The wind loads are imposed on tower beam, insulators, conductor and ground wires, etc. and are random in nature. This load is not continuous over time. The calculation of wind load for substation structures would be according to this code [2], and this is different from the national code for calculation of wind load [9]. However, it is highlighted that the cyclone factor introduced in the latest revision of the general wind load code [9] has not yet been incorporated in the code [2] for wind load on the substation (transmission line) structures. Therefore, it is recommended that the cyclone factor (k_4) as incorporated in general IS code [9] must be adopted for all substation structures, as applicable according to the code [9], over and above the wind speed calculated according to the code for substations [2].

- **Temperature loads:** The temperatures in different localities in India are different and further, temperature in the same locality has diurnal and seasonal variations. Maximum and minimum temperatures at the specific site, including diurnal and seasonal fluctuations can be ascertained from historical records. In case such records are not available, the code [2] provides the absolute maximum and absolute minimum temperatures expected across the country, as air temperature in shade. For sites falling between two isopleths, the higher (lower) value may be adopted for absolute maximum (minimum) temperature. Average everyday temperature might be taken as 32 °C across the country, except for the regions with minimum temperature less than or equal to -5 °C, where the average temperature may be taken as 15 °C. The radiation and heating effects of current passing through the conductors also need to be considered for calculating the maximum temperature of the conductor. In lieu of exact calculations, a maximum temperature of 85 °C (95 °C) may be assumed for the ACSR: aluminium conductor steel reinforced (AAAC: all aluminium alloy conductor). For the ground wire/s, the maximum temperature may be assumed as 53 °C for wires exposed to sun.

- Substation structures are light structures, and therefore design is generally governed by the maximum wind pressure. Seismic event and maximum wind pressure happening concurrently is unlikely to occur and therefore not considered in design. However, in earthquake-prone areas, the substation structures should be checked for earthquake load according to the applicable IS code [10], along with zero wind and minimum temperature, as stipulated in [2].

The climatic loads would be considered for the most severe of the following conditions:

- 100 per cent design wind pressure at everyday temperature;
- 75 per cent design wind pressure at everyday temperature: generally applicable for *Security requirements*;

- 36 per cent design wind pressure at minimum temperature: could be crucial particularly for short span between towers/beams;

* **Failure containment loads:** These are the loads related to the security requirement of the structure. The major types of *failure containment loads* would be:

- **Anti-cascading loads:** These provisions are incorporated to prevent the cascading failure of the system. For example, sequential failure of minor components such as insulators, hardware, joints—leading to failures of major components such as towers, foundations, conductors, etc. would be a cascading failure case. The structure would have to be checked for all conductors/ground wires intact on only one side of the structure.

- **Torsional / longitudinal loads:** These loads occur due to breakages of wires (conductors, ground wires, etc.) and each component should be designed for breakages of one/more of the wires connected to the structure.

- **Narrow front wind loads:** This load is applicable for suspension towers only – for a special case when higher wind velocity active over a narrow width acts on the tower and insulator/s but no wind is there on the wires. This is generally not applicable for substation structure, except for large switchyards.

* **Construction and maintenance loads:** As the name implies, these are the postulated loads coming on the structures during operations and maintenance of the structures and this generally consist of forces, for which the magnitudes and the locations of applications have been enumerated in the code [2] for different types of members.

The loads from electrical components or their failures could be normal tension force, sag tension force, short circuit force, and broken wire force—for the different conductors, ground wires, etc. and must be provided by the electrical team for analysis. For further elaboration of the loading calculations readers are directed to the IS code [2] for general guidelines or specialist literature for special components.

Once the various loads coming on the substation structures are determined and the structure is analyzed for individual loads, the design would be performed for appropriate load combinations, and these are also elucidated in the code [2]. Broadly speaking, these are performed for fulfilling the special design requirements described above, namely, *Reliability requirements*, *Security requirements*, *Safety requirements*, and *Anti-cascading checks*. In each case, the climatic loads are specified in the load combination table (Cl. 13 [2])—whether wind pressure would be 100%, 75%, or 36%; whether wind angle would be 0°, 30°, 45°, or 90°; whether temperature would be everyday temperature, maximum temperature or minimum temperature. For each case, again, the longitudinal, transverse and vertical loading effects should be calculated for combination.

Design of Substation Structures

After the loads and the combinations are finalized, the analysis of the substation structures is performed according to the general principles of structural mechanics. Further, the general design philosophies of concrete and steel components

are applicable according to the national codes [6, 7]. The design is performed for strength, serviceability, stability, and durability.

However, there exist some special provisions for design of substation (transmission line) structures as well. These

include the calculation of the slenderness ratios of members that need to be performed according to the Table 6.1 / Cl. 6 [3] and the limiting values are also provided. Because of the typical nature, detailed cases are exemplified in Annex B of the code [3], which include leg member using symmetrical bracing;

Table 1: Comparison of salient design considerations for industrial steel structures and substation steel structures.

	Design consideration	Industrial steel structure	Substation steel structure
1.	Applicable wind code	IS 875 (Part 3) [9].	IS 802 (Part 1/Section 1) [2] (with cyclonic factor from [9], as applicable).
2.	Return period for wind loads	50 years (IS 875 Part 3) [9].	50 years (reliability level 1: up to 400 kV class); 150 years (reliability level 2: above 400 kV class); (IS 802, Part 1 / Section 1) [2].
3.	Wind load consideration in load combinations	100% (IS 800; IS 875 Part 3) [6, 9].	36%, 75%, OR 100% (as applicable according to load combination in IS 802 (Part 1 / Section 1) [2].
4.	Applicable seismic code	IS 1893 (Part 4) [20].	IS1893 (Part 1) [10].
5.	Applicable material properties and design code	IS 800 [6].	Material: IS 802 (Part 1/ Section 1) [2]; Design provisions: IS 802 (Part 1/Section 2) [3].
6.	Limiting width to thickness ratio for compression members	Table 2 (IS 800) [6]; Maximum value (Fe 250): 15.7 [6].	IS 802 (Part 1/Section 2) [3]; Maximum value (any steel): 25 [3].
7.	Limiting slenderness ratio	IS 800 [6]: Compression members: 180; Tension member with stress reversal (other than EL/WL): 180; Compression member only under EL/WL: 250; Tie member in truss / bracing system: 350; Axial tension only: 400.	IS 802 (Part 1/Section 2) [3]: Compression members: 150; Other members:150; Redundant members / members carrying nominal stresses: 250; Axial tension only: 400.
8.	Effective length calculation	Based on rotational and relative translational boundary conditions at the ends of the member (Clause 7.2, IS 800 [6])	Based on rotational and relative translational boundary conditions at the ends of the member, ratio of length between supports and the radius of gyration, method of loading /rigidity of joints (Clause 6.1, IS 802, Part 1 / Section 2 [3])
9.	Special loading consideration	Generally not applicable, except special structures such as nuclear, radiochemical, or hazardous facilities.	IS 802 Part 1/Section 1 [2] Broken wire condition; Anti-cascading.
10.	Design considerations	IS 800 [6] Strength; Serviceability; Stability; Durability.	IS 802 Part 1/Section 2 [3] Strength; Serviceability; Stability; Durability; Reliability; Safety; Security.
11.	Applicable foundation design code	IS 1904 [13].	IS 4091 [4, 5].
12.	Statutory requirements	Generally not applicable, except special structures such as nuclear, radiochemical, or hazardous facilities.	<ul style="list-style-type: none"> • Indian Electricity Rules, 2005; • Local and provincial byelaws; • Fire and safety laws including IS 5613 [8]; • Civil aviation requirements/ electricity rules.

leg member using staggered bracing; effect of end connection; bracings with and without secondary members; k-bracings with and without secondary members; among others.

For compression members of the substation steel structures, the width-to-thickness ratio limit has been specified and accordingly the allowable stresses in compression for the members must be calculated [3]. These provisions are typical to substation steel structures (transmission line structures) and dissimilar when compared to those for conventional industrial steel structures/members [6].

Design and Construction of Foundations for Substation Structures

As mentioned for the member design, foundation design and construction are governed by the national codes, unless specially provided for in this code [4, 5]. Foundation design for substation structures are performed for two conditions:

- Normal conditions;
- Broken-wire condition (all postulated combinations).

The loading information required for analysis and design of foundations are:

- Downward load: this would include the gravity loads, and downward reaction due to the climatic loads, imposed loads, etc., and construction & maintenance loads;
- Uplift load: though this is called uplift load, it is not limited to the uplift per se, but includes the lift-off caused by the upward reaction generated in one/more footing/s in the group of footings; this lift-off could occur in one/more footings to resist the high moments generated due to the action of climatic loads, imposed loads, etc., with or without construction & maintenance loads;
- Transverse load (orthogonal directions): transverse loads would be generated due to the climatic loads, imposed loads, etc., and construction & maintenance loads in both orthogonal direction in different combinations;
- Overturning moments (orthogonal directions): the moments would be generated due to the eccentric action of the resultant vertical and transverse loads on each structure for each load combination;

As required for any other foundation, foundations of substation structures must be safe against sliding, overturning, uplift, and bearing for each load combination. The safe bearing capacity of soil/rock may be estimated according to the guidelines given in the code [4, 5] or the regular Indian standard/s – but after requisite site explorations to determine the soil/rock properties at the site [11 – 13].

For foundations in soil, there are detailed guidelines [4, 5] for calculation of uplift resistance for shallow foundations. Generally, the uplift forces on the foundation would be resisted by the self-weight of the footing and the weight of a frustum of the soil in the shape of an inverted pyramid with a wedge at 30° (cohesive) and 20° (cohesion-less) with vertical, as applicable.

For foundations on rock, the uplift forces may be resisted by the rock anchors, and the following are stipulated for the same in the code [4, 5]:

- Minimum depth of embedment below footing bottom: 45 times the diameter of the anchor rod;
- Minimum spacing of rod: 22.5 times the diameter of the anchor rod;
- The diameter of the anchor rod must be determined such that the combined stresses in the anchor rods do not exceed

the permissible limits;

In case of pile foundations, uplift would be resisted by the under-reamed piles. Safe loads are provided for a few salient combinations of diameters of pile/under-reams and reinforcement details in Table 2 [3, 4] for minimum pile length of 3.5 m, with increments specified for each 30 cm increase in length. These values of safe loads are applicable for sandy soil ($10 \leq N \leq 30$) and clayey soil ($4 \leq N \leq 8$). Below (above) the limit, a 25% reduction (increase) in the safe load of the pile is suggested. For other cases, reference may be made to the regular Indian standard applicable for the pile design [14 – 19].

A summary of the salient points of comparison between industrial steel structures and substation steel structures are provided in Table 1 for ready reference.

Summary

In summary, the article introduced the various components of the civil structures of electrical substations for NFCFs. The analyses of these structures are performed by the general principles of structural mechanics. However, the loads on these structures vary from the conventional industrial steel structures, along with the design considerations, design load combinations, and some design provisions as well [2, 3]. Particularly, the loads occurring due to the conductor/ground wires, and considerations of the narrow front wind load, cascading failure, broken wire conditions, short circuit forces, sag tension forces in wires make analysis of such structures typical. The design is governed by three considerations, namely, Reliability requirements, Security requirements, and Safety requirements. Foundation design is more or less similar to the conventional structures, except that the substation towers would have substantial uplift force, horizontal loads and overturning moments due to the loads coming from the conductor/ground wires, and the broken wire/ short circuit/ anti-cascading conditions. Passive resistance of soil or under-reamed piles for foundations on soil and anchor rods for foundations on rock – are recommended in the Indian codes [4, 5]. The salient features of analysis and design of the civil structures in electrical substation have been elucidated in this article with reference to the applicable Indian codes of practice. Readers may refer the cited codes and/or specialist literature for further information on the topic.

Acknowledgements

Authors wish to acknowledge Desalination Division, BARC for presenting them with this opportunity during OSCOM project work, when design for sub-station structures were undertaken for the first time in BARC.

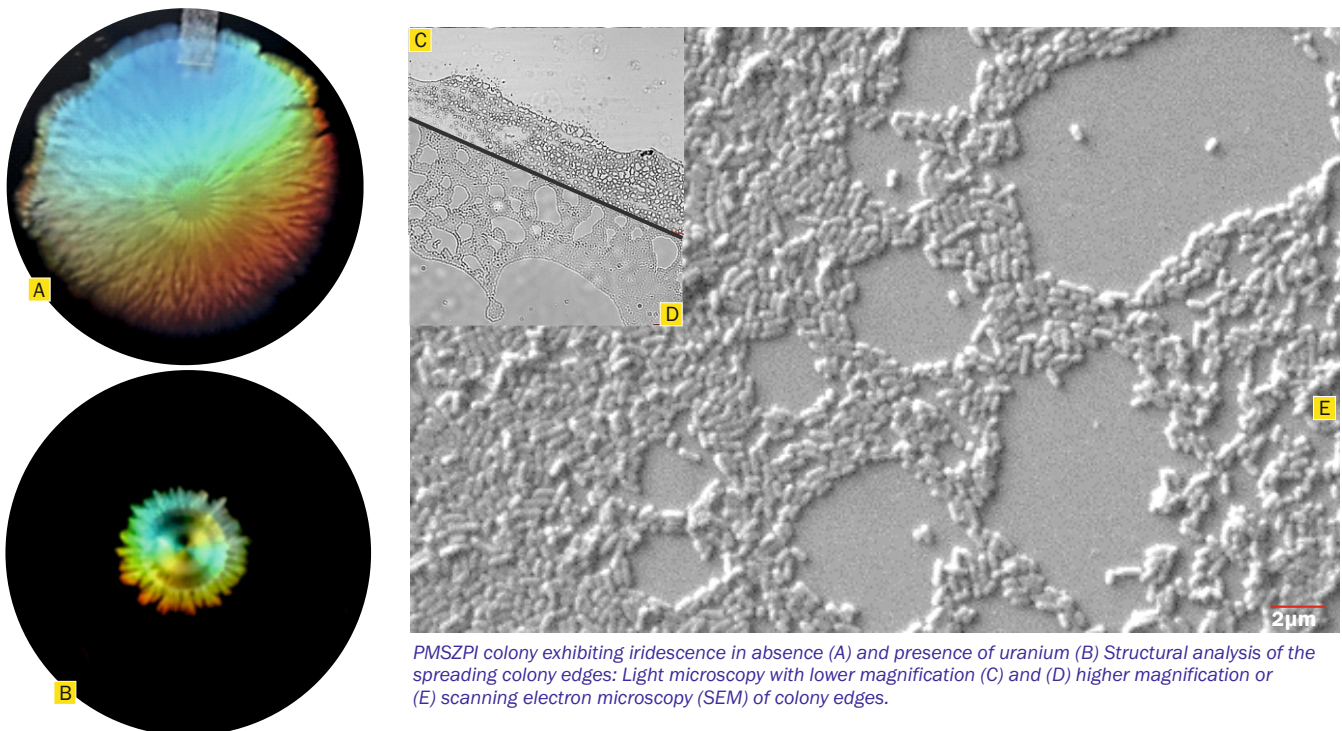
References

- [1] Dauji S and Bhargava K (2022) Civil Design Considerations for Electrical Substation Structures and Foundations, Proceedings of Third DAE-BRNS Symposium on Recent Advances in Nuclear Fuel Cycle Activities NUFUC 2022, pp. 162 – 164, 20-21 May, 2022, Tarapur, Maharashtra, INDIA.
- [2] Bureau of Indian Standards (BIS) Use of Structural Steel in Overhead Transmission Line Towers – Code of Practice, Part 1: Materials, Loads, and Design Strengths, Section 1: Materials and Loads, IS 802 (Part 1 / Sec 1): 2015 (Fourth Revision), New Delhi, India (2015).
- [3] Bureau of Indian Standards (BIS) Use of Structural Steel in Overhead Transmission Line Towers – Code of Practice, Part 1: Materials, Loads, and Design Strengths, Section 2: Design Strengths, IS 802 (Part 1 / Sec 2): 2016 (Fourth Revision), New Delhi, India (2016).

- [4] Bureau of Indian Standards (BIS) Code of Practice for Design and Construction of Foundations for Transmission Line Towers and Poles, IS 4091: 1979 (First Revision) (Reaffirmed 2010), New Delhi, India (1979).
- [5] Bureau of Indian Standards (BIS) Code of Practice for Design and Construction of Foundations for Transmission Line Towers and Poles, IS 4091: 2019 (Second Revision – Draft), New Delhi, India (2019).
- [6] Bureau of Indian Standards (BIS) General Construction in Steel – Code of Practice, IS 800: 2007 (Third Revision), New Delhi, India (2007).
- [7] Bureau of Indian Standards (BIS) Plain and Reinforced Concrete – Code of Practice, IS 456: 2000 (Reaffirmed 2005) (Fourth Revision), New Delhi, India (2000).
- [8] Bureau of Indian Standards (BIS) Code of Practice for Design, Installation and Maintenance for Overhead Power Lines – Part 3: 400 kV Lines – Section 1: Design, IS 5613: 1989 (Reaffirmed 2019), New Delhi, India (1989).
- [9] Bureau of Indian Standards (BIS) Design Loads (Other than Earthquake) for Buildings and Structures – Code of Practice, Part 3: Wind Loads, IS 875 (Part 3): 2015 (Incorporating Amendment No. 1 dated April 2016), (Third Revision), New Delhi, India (2015).
- [10] Bureau of Indian Standards (BIS) Criteria for Earthquake Resistant Design of Structures, Part 1: General Provisions and Buildings, IS 1893 (Part 1): 2016, (Sixth Revision), New Delhi, India (2016).
- [11] Bureau of Indian Standards (BIS) Method of load test on soils (second revision), IS 1888: 1982, New Delhi, India (1982).
- [12] Bureau of Indian Standards (BIS) Code of Practice for Subsurface Investigation for Foundations, IS 1892: 1979, (First Revision), New Delhi, India (1979).
- [13] Bureau of Indian Standards (BIS) Code of Practice for Design and Construction of Foundations in Soils: General Requirements, IS 1904: 1986, (Third Revision), New Delhi, India (1986).
- [14] Bureau of Indian Standards (BIS) Design and Construction of Pile Foundations – Code of practice: Part 1 Concrete piles: Section 1 Driven Cast In-situ Concrete Piles, IS 2911 (Part 1/Sec 1): 2010, (Second Revision), New Delhi, India (2010).
- [15] Bureau of Indian Standards (BIS) Design and Construction of Pile Foundations – Code of practice: Part 1 Concrete piles: Section 2 Bored Cast In-situ Concrete Piles, IS 2911 (Part 1/Sec 2): 2010, (Second Revision), New Delhi, India (2010).
- [16] Bureau of Indian Standards (BIS) Design and Construction of Pile Foundations – Code of practice: Part 1 Concrete piles: Section 3 Driven Precast Concrete Piles, IS 2911 (Part 1/Sec 3): 2010, (Second Revision), New Delhi, India (2010).
- [17] Bureau of Indian Standards (BIS) Design and Construction of Pile Foundations – Code of practice: Part 1 Concrete piles: Section 4 Precast Concrete Piles in Pre-bored Holes, IS 2911 (Part 1/Sec 4): 2010, (First Revision), New Delhi, India (2010).
- [18] Bureau of Indian Standards (BIS) Design and Construction of Pile Foundations – Code of practice: Part 3 Under-reamed Piles, IS 2911 (Part 3): 2010, (Second Revision Under Preparation), New Delhi, India (2010).
- [19] Bureau of Indian Standards (BIS) Design and Construction of Pile Foundations – Code of practice: Part 4 Load Test on Piles, IS 2911 (Part 4): 2013, (Second Revision), New Delhi, India (2013).
- [20] Bureau of Indian Standards (BIS) Criteria for Earthquake Resistant Design of Structures, Part 4: Industrial Structures Including Stack-like Structures, IS 1893 (Part 4): 2015, (First Revision), New Delhi, India (2015).

Microbial Iridescence

An interesting feature in a Uranium Tolerant Bacterium Chryseobacterium...



PMSZPI colony exhibiting iridescence in absence (A) and presence of uranium (B) Structural analysis of the spreading colony edges: Light microscopy with lower magnification (C) and (D) higher magnification or (E) scanning electron microscopy (SEM) of colony edges.

The spreading colonies of the gliding bacterium *Chryseobacterium* sp. strain PMSZPI displayed self assembly of cells into highly ordered structures which on illumination with natural light exhibited bright iridescent colours.

*Celin Acharya

It has been over a decade that our laboratory is actively engaged in investigating the mechanisms of uranyl interactions with microbes that are important for uranium bioremediation. In that context, we demonstrated the notable tolerance of a bacterium, *Chryseobacterium* sp. strain PMSZPI, isolated from the subsurface soil of Domiasiat uranium (U) ore deposit in Northeast India to uranium and other heavy metals. The genome of PMSZPI was sequenced and the first draft sequence was released in 2017 with NCBI Genbank Accession No. PIZV000000000.

Recently, we reported the interesting phenomenon of iridescence in PMSZPI that was found to be associated with its gliding motility (D. Khare *et al.*, 2022, *Gliding motility of a uranium-tolerant Bacteroidetes bacterium Chryseobacterium* sp. strain PMSZPI: insights into the architecture of spreading colonies, Environmental Microbiology Reports, Cover page article). The word 'iris' derived from the Greek meaning rainbow, is an optical effect attributed to the surfaces that change in colour and intensity with the viewing angle. The strain PMSZPI harbored majority of the Bacteroidetes gliding motility genes and formed spreading colonies as a result of gliding on agar surfaces. Such colonies were intensely coloured when observed under trans-illumination with natural light. *In-situ* structural analysis of the spreading colony edges revealed the self assembly of the cells that are periodically arranged in lattice-like structures which possibly diffracted the incident light causing angle dependent iridescent appearance of the colonies. It was observed that uranium negatively affected the colony spreading although the periodicity within the cellular population at colony edges was found to be intact displaying iridescence. Bacterial iridescence has been reported under stressful conditions. It could possibly provide novel bio-material for photonic applications like paints and coatings.

*Molecular Biology Division
Bio-science Group
Bhabha Atomic Research Centre
Mumbai- 400085, India



Pipes manufactured by Nuclear Fuel Complex from the UNS N06690 billets supplied by M/s. Midhani

Road Through Indigenization

A new milestone in vitrification of nuclear waste

Subrat Kaushik*, Ved Singh, K.V. Ravi

Nuclear Recycle Board (NRB) uses a special material viz. UNS N06690/ N06600 for waste management plants (Joule Melter for vitrification of High Level Wastes (HLW)). The Melter used for vitrification operates at a temperature of around 1050°C and the environment is extremely corrosive besides high radiation field. High Ni-Cr based alloy pipes and other fabricated items as per ASTM B-167 e.g. alloy UNS N06690 & UNS N6600 are the suitable materials used for such high temperature and highly corrosive application for immobilization of high level active wastes. These special grade material items used to be imported to meet the department requirement. Since, this is a regular requirement and in order to reduce the level of dependency on imports, a thrust was provided to manufacture them locally.

NRB has now successfully developed and manufactured for the first time the raw material (UNS N06690 ingots) & pipes to meet the existing requirement and the requirement of upcoming waste management plants under Atmanirbhar Bharat scheme. There were three major steps in this work:

- Preparation of technical specifications
- Development, manufacturing and characterization of UNS N06690 billets as raw material manufactured by M/s Mishra Dhatu Nigam Ltd (Midhani).
- Conversion of raw developed material (billets) into tubular products by Nuclear Fuel Complex, a constituent unit of DAE.

Technical Specifications of Product and Challenges

The chemical composition was as per ASTM B-167 with restricted Nitrogen & Titanium content. The mechanical and physical properties conformed to ASTM B-167. The test for

stress corrosion cracking was specified as per ASTM G 28. Specific emphasis was paid to grain size and inclusion rating as the application requires working at 1050 °C. Creep tests as well as stress rupture tests were specified as per ASTM E139-11. For the final products, non-destructive tests (NDT) e.g. ultrasonic test and eddy current tests were specified in addition to specified dimensions and tolerance as per ASTM A-312.

Manufacturing

The billets were manufactured by M/s Midhani in a timely manner for delivery to NFC as per prescribed NRB requirements and specifications. NFC has developed new tooling systems for manufacturing of different pipe sizes, which was a very exhaustive exercise due to multiple attempts for finalizing the tooling design and its manufacturing. The requirement of special testing at elevated temperature (1095 °C) for creep and stress rupture tests for billets and pipes were carried out. It is extremely difficult to conduct these tests for 100 hours as the associated instrumentation and fixtures may malfunction at such elevated temperature. Timely execution for this order was crucial as it was urgently required for ongoing NRB Projects/ Plants.

Testing and Results

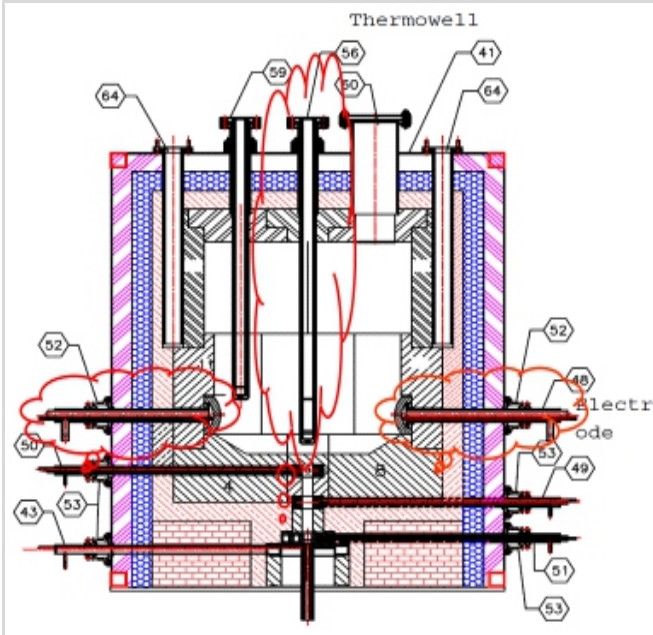
The material was thoroughly tested for quality standards at BARC, NFC, Midhani and at a NABL Lab for raw material as well as for finished pipes. The test results were found within the requirement of the technical specification limits for chemical, mechanical, creep, stress rupture, NDT and corrosion tests.

Significant Achievement

It may be seen that the results of UNS N06690 pipes manufactured for NRB meet the codal requirement of ASTM

B167 and have passed all the special tests such as creep, stress-rupture and SCC to meet the operating requirement of Joule Melters of NRB for immobilization of High Level Wastes.

The total weight of the billets supplied by M/s. Midhani to NFC was 11.4 MTe and the total weight of finished pipes was 7.57 MTe. The expected recovery/ yield in the form of finished pipes (weight) was better than the expected levels and was approximately 66% of the weight of the raw material. The cost of development and manufacturing indigenously is significantly lower than the previous quotations received from foreign bidders for UNS N06690 pipes.



A schematic of Joule Melter.

Acknowledgements

The exercise involving manufacturing of UNS N06690 pipes is comprehensive and at the same time challenging too. NRB received requisite help from various experts and agencies to accomplish the mandate.

Authors wish to acknowledge K.V. Ravi, Chief Executive, NRB, for his guidance and encouragement which made possible this remarkably special achievement; Vivekanand Kain, Director, Materials Group, BARC and his team for providing valuable inputs in preparation of technical specifications; Arbind Kumar, QAD, BARC for special NDT Tests; Dinesh Srivastava, CE, NFC; Komal Kapoor, Dy. CE, NFC & the team responsible for manufacturing of UNS N06690 pipes, S.K. Jha, CMD, Midhani and the team involved in the manufacturing of raw material (Billets).



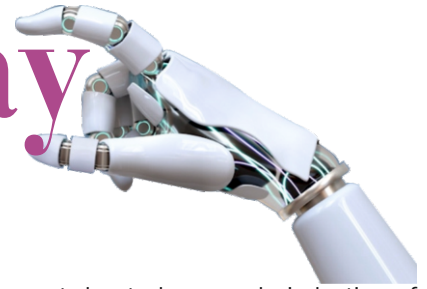
Inconel 690 billet produced by M/s MIDHANI.



The initiation of supply of alloy 690 products. These high value products of strategic importance were produced at Nuclear Fuel Complex facility in Hyderabad.

The authors are from Nuclear Recycle Board, Bhabha Atomic Research Centre, Mumbai.
*Author for Correspondence: Subrat Kaushik
E-mail: subratk@barc.gov.in

Smarting Energy Systems The IIoT Way



Dr. A. K. Bhattacharjee*

Energy management is becoming smart due to large scale induction of Industrial Internet of Things (IIoT) as a way of physical measurements, control, edge computing, connecting to clouds and interfacing to computational platforms. The smartness of the system as a whole emanates from the fact it can sense occupational loads, thermal comforts, ambient lighting, use energy mix from local sources such as solar panels and interface with load dispatch centres and tries to achieve energy consumption in a near optimal manner.

I guess that energy mix with physical measurements and control with traditional power system stability analysis are what were the core competency of power system design till recently. However, with introduction of edge computing, cloud computing and algorithmic techniques brought in the era of smart energy management. The monograph by the authors covers the algorithmic techniques in details.

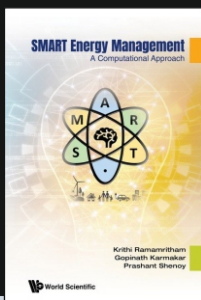
The monograph starts with an introduction to Smart Electricity Grid identifying Advanced Edge Metering, Monitoring, Control Infrastructure (AMI) in residential and industrial facilities. The reader will get adequate understanding of Phasor Management Units (PMU), Phasor Data Concentrators (PDC), communication protocols and the hierarchical control in smart grids. The next chapter introduces the key ideas behind Energy Management Systems for Buildings and brings out need for sensors sense, analysis tools and control actions as part of sense, analyze and respond. It introduces the notion of observability. Practitioners would find this chapter very interesting as it would bring out interfacing IIoTs with data collection, analysis for observability. Authors then introduce the concept of thermal comfort in a very systematic way with an overview of Building Management System and the concept of TCBM scheduling. It emphasizes a great deal on modeling aspects of Building space, HVAC systems and heat balance from physics principles.

An important learning in this chapter is the analysis aspects of feasibility of maintaining thermal comfort with TCBM scheduling of AC plants optimizing energy usage. Authors use a number of case studies to demonstrate how these concepts can be realized. The book is quite self-contained as it provides other reading materials to cover Grid Management techniques, Power System Stability Analysis and Thermal Modeling fundamentals.

Overall a good technical treatise on smart energy and must read for students in energy studies and engineering, AI specialists in using IIoTs for designing Building Management Systems and even policy makers. The book is even good for architects planning and designing electrical energy system for industry and cities; data collection through edge devices, energy consumption in building, industrial houses, locality and pushing these data through the cloud for an in-depth assessment of utilization of energy, predicting future energy requirements and energy mix for keeping the greenhouse effect under control. Of course privacy of individual and cyber security concern must be addressed.

IMPRESSIONS

- A good technical treatise on smart energy.
- A must read for AI specialists using Industrial Internet of Things (IIoT) for designing Building Management Systems.



**Smart Energy Management
- A Computational Approach
By Krithi Ramamritham,
Gopinath Karmakar and
Prashant Shenoy**

World Scientific Publishing Co. Pte Ltd.,
Singapore

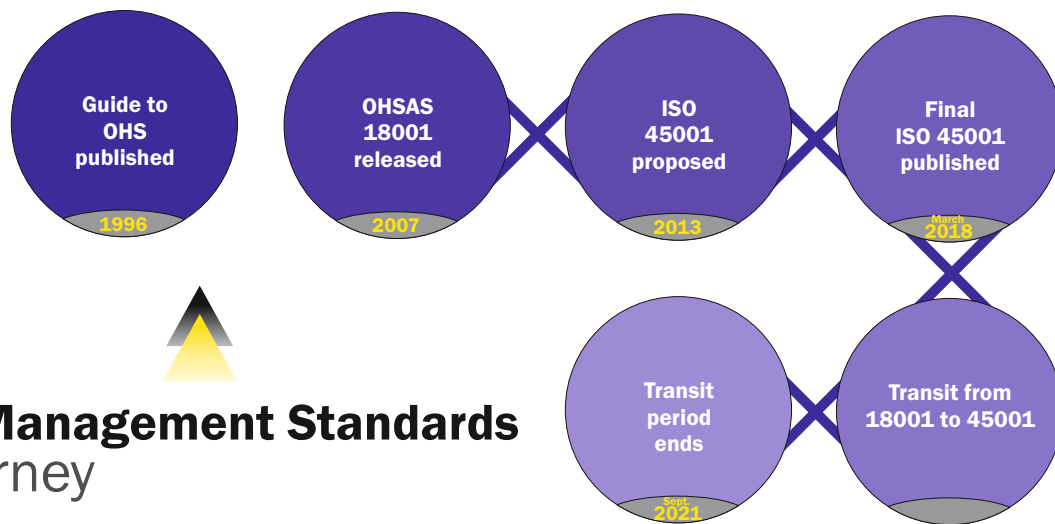
(The author is affiliated to BARC Electronics and Instrumentation Group. He's currently heading the Security Electronics and Software Systems Division)*



The New Occupational Health & Safety Management System

ISO
45001:2018

Photo © ISO official website



OHS Management Standards A journey

Vyom Saxena
IHSS, BARC
(vsaxena@barc.gov.in)

ISO or the International Organization for Standardization is an organisation that helps to establish various international standards and corresponding certifications which are globally accepted. It is an independent, non-governmental organization, the members of which are the organizations dealing with the standards of the 165 countries[1]. It is the world's major creator of voluntary international standards facilitating world trade through common standards among nations. ISO Standards ensure that products, services, procedures are safe, reliable and of good quality. Application of ISO standards reduces costs by minimizing waste and errors and increasing productivity.

The first systemic efforts that were made at international level to standardise Occupational Health and Safety (OHS) management began in early nineties and the guide to OHS was out in 1996 and OHSAS (Occupational Health and Safety Assessment Series) 18001 released in 2007 was the first international standard for occupational health and safety management systems which was later adopted as a British Standard. The rise and journey of OHS standardization process is depicted in the form of an illustration given above.

ISO 45001:2018 is an International Standard Occupational Health and Safety Management System based on the OHSAS 18001, conventions and guidelines of the International Labour Organization including ILO OSH 2001, and other national standards that specify the requirements of an Occupational Health and Safety (OHS) management system. This standard intends to improve organization's OHS performance proactively. Since it follows the High-Level Structure of other ISO standards, an organization can easily integrate all these standards just by adopting ISO 45001 certification. The ISO 45001:2018 standard came into being on 12th March 2018 after the acceptance of the second draft in 2017 (the first draft of 2016 was rejected)[2]. ISO 45001 is now a recognized international standard for Occupational Health and Safety (OH&S) Management Systems and it has entirely replaced the BS OHSAS 18001 post September 2021. The replacement deadline was initially for exact three years, i.e., March 2021, but it was extended by six months due to Covid-19 pandemic. Certification to ISO 45001 is not an aim of the standard but can be a useful tool to demonstrate the compliance with the objectives of the certificate.

Structure

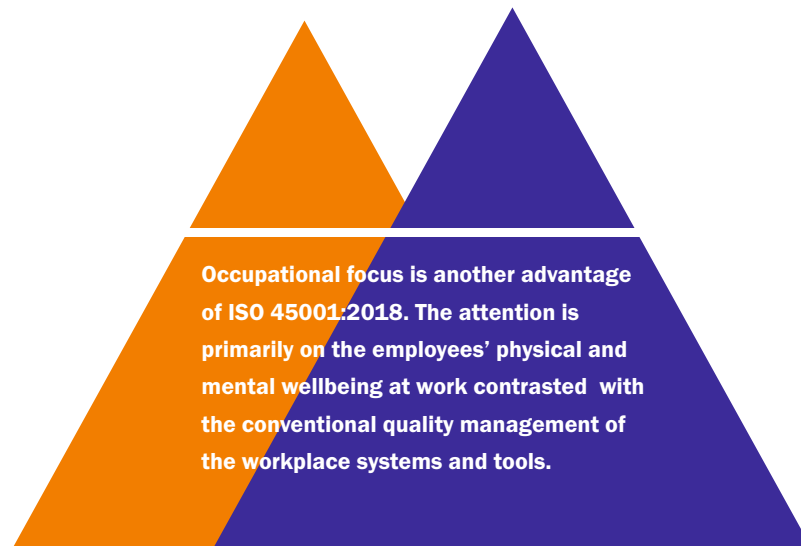
ISO 45001 uses the Annex SL process and structure, easing the use and integration of multiple ISO management system standards for employment by a single organization. It entails an increased focus on the context of the organization and a stronger role of its top management and leadership. The structure has 10 clauses, namely:

- Scope
- Normative references
- Terms and definitions
- Context of the organization
- Leadership
- Planning
- Support
- Operation
- Performance evaluation
- Improvement

ISO 45001 has adopted the four stage Plan-Do-Check-Act (PDCA) cycle for achieving constant improvement. It adopts a systematic approach to determine workable solutions, assessing the results, and implementing those solutions that have been shown to work.

Applicability, Scope and Objectives

ISO 45001:2018 is most suitable for any organization that wants to establish, implement and maintain an OHS management system to improve occupational health and safety, eradicate hazards and minimize OHS risks (including system deficiencies), take advantage of OHS opportunities, and tackle OHS management system nonconformities associated with its activities. This standard is applicable to all types of organizations regardless of their size, nature, location, type and activities and may include medical facilities, manufacturing industries, service organizations or other industries and workplaces. It is designed to be integrated into an organization's existing management processes and follows the same high-level structure as other ISO management system standards, such as ISO 9001 (quality management)



and ISO 14001 (environmental management).

ISO 45001:2018 intends to enable organizations in providing safe and healthy workplaces by preventing work-related injury and ill health, besides proactively improving its OHS performance. The objectives of ISO 45001:2018 include

- * Continual improvement of OHS performance
- * Fulfilment of legal and other requirements
- * Achievement of OHS goals

ISO 45001:2018 applies to the OHS risks under the organization's control, taking into account factors such as the context in which the organization operates and the needs and expectations of its workers and other interested parties. It enables an organization, through its OHS management system, to integrate other aspects of health and safety, such as worker wellness or wellbeing. However, it does not state specific criteria for OHS performance, nor does it prescribe any design of OHS management system. It also does not address issues such as product safety, property damage or environmental impacts, beyond the risks to workers and other relevant interested parties.

ISO 45001:2018 can be used wholly or partly but one cannot claim compliance with this certification unless all its requirements are incorporated into the organization's OHS management system and implemented without any exception.

Advantages

ISO 45001 enables organizations to put in place an occupational health and safety (OHS) management system. This will help them manage their OHS risks and improve their OHS performance by developing and implementing effective policies and objectives.

The salient potential benefits from the use of this standard include:

i. It enhances safety due to reduction in unsafe conditions and workplace incidents. Another feature responsible for enhanced safety is preventative risk and hazard assessment. Implementing ISO 45001 helps the organization prevent risks. The internal auditing system provides helps in spotting potential threats to health and safety.

ii. It increases Return-on-Investment (RoI). By implementing ISO 45001, the efficiency of staff improves, whilst workplace injuries reduce, implying productivity levels can be improved significantly across the board. This improvement in productivity and general employee safety can have a positive impact on the expenditures like insurance premiums for the organization by reducing the work-related insurance claims thus lowering the cost of insurance for the business.

iii. Occupational focus is another advantage of this ISO. The attention is primarily on the employees' physical and mental wellbeing at work contrasted with the conventional quality management of the workplace systems and tools.

iv. ISO 45001 implementation also results in improved morale of the employees. It perks up individual safety as well as organizational since it addresses the personal health and safety risks to the individual due to any process or use of machinery within the organization. This includes both mental health and physical safety within the workplace.

v. This ISO deals with both the risk and opportunities whereas previous standards primarily dealt with the risks presented by the organizational process and characteristics.

vi. ISO 45001 leads to increased productivity as a result of reduced absenteeism and staff turnover. The standard is built around the best OHS practices. Having a strong, consistent standard means that the organization is more efficient all around. It improves staff morale, which has a significant impact on staff turnover and retention rates. The consistency achieved due to the standard translates into efficiency.

vii. Implementing ISO 45001 results in reduced insurance costs due to lower insurance premiums as it proves the organization is sincerely managing and protecting their employees.

viii. As the ISO requires top-down approach, it involves participation by all the employees of the organization. This translates into better health and safety culture due to active role by employees in their own OHS.

ix. This particular ISO ensures responsibility and ownership lies with top level management. It reinforces leadership commitment to OH&S performance due to enhanced and proactive participation by management towards OHS. With the involvement of top leadership and a clearly communicated process for



identifying hazards, there is continuous improvement in the occupational health and safety over time.

- x. The implementation of this certification also results into improved compliance to meet legal and regulatory requirements.
- xi. It leads to enhanced reputation of the organization. By implementing the latest and the most upgraded occupational health and safety standard, the organization is considered in the leading category among the similar organizations and internationally recognized. This level of excellence is acknowledged worldwide and gives an edge to the organization over its competitors.

It also increases mutual trust between employees and the organization and between organization and the outer world. By demonstrating continuous improvement of employees' morale, safety and performance, people trust and hold the organization socially accountable for the staff's well-being. By being transparent and promoting corporate social responsibility, the opinion and trust of the public, future employees and prospective clients improves considerably.

Difference between OHSAS 18001 and ISO 45001

An organisation already accredited to OHSAS 18001, had time to transit to the ISO 45001 and the benefits that come with it until 30th September 2021 with little efforts due to the availability of some of the necessary tools and systems in place to implement ISO 45001. Since both the accreditations are concerned with the occupational health and safety, people often confuse ISO 45001 and OHSAS 18001 to be same although there are significant differences between these two accreditations. It is important to understand these differences along with the significance that one has with the other.

1. **Annex SL:** Annex SL is a new management system format that helps streamline creation of new standards, and eases the implementation of multiple standards within an organization easier. The Annex SL is a section of the ISO/IEC directives part 1 that prescribes documentation of ISO Management System Standards (MSS).

ISO 45001:2018, like most other ISO standards, has adopted the Annex SL High Level Structure (HLS) which is the core of any modern ISO standard accreditation. Annex SL is designed to simplify integration with other management

systems like ISO 9001 and 14001 with consistent language and matching sub-clauses, making it easier for an organisation to build and manage an integrated management system.

2. **Inclusion of Top Management:** Clause 5 of ISO 45001 strongly emphasises and encourages the incorporation of health and safety into the broader management system of the organisation. This aspect ensures enhanced role of the top management who are now expected to take a stronger top-down leadership role. Under ISO 45001 the role of the management representative is permitted but strongly discouraged unlike OHSAS 18001, where the operation of the occupational health and safety management system could be delegated by senior management to a representative. There are 3 main reasons for this:

(i) ISO 45001 places a strong emphasis on risk like all modern ISO standards. If health and safety responsibility is delegated to a single person or a very few then it is a risky proposition indeed, especially in the context of larger organisations.

(ii) In contrast, If the above responsibility is distributed among many employees and at many levels then it will certainly lead to improvement over a period of time.

(iii) The involvement of top management will imply that they cannot afford to escape from the obligations of the process of the health and safety management system by simply appointing and delegating OHS responsibilities to a representative.

3. **Top Down Operations:** This is a direct outcome of point 2 which translates into the operations of health and safety management system as described in the following points:

(i) Frequent reviews of the health and safety system performance by the management;

(ii) Management actively collecting feedback from employees for improvement and corrective/preventive action;

(iii) Management Initiating and participating in safety audits;

(iv) Management encouraging and rewarding hazard identification and constructive ideas;

(v) Availability, both timely and sufficiently of resources, like quality management tools, safety and protective gears.



4. All-inclusive Health and Safety Culture and Greater Participation by Staff: ISO 45001, by removal of the management representative position and greater top-down focus, encourages health and safety responsibility and engagement as much as possible so that most of the employees can support and contribute to a culture of health and safety. Not only all the employees are trained on health and safety procedures and required to abide by them, but are aware of the objectives and advantages of a safe, healthy and efficient workplace and authorized to contribute to it.

A firm integration of health and safety culture into the organisation is reflected in many ways and should begin with its inclusion in the recruitment itself, followed by policies which make sure that the employees have enhanced participation and consultation and policies are devised around their feedback. Also, the employees are encouraged to flag the risks and opportunities during their routine jobs. Management is also obliged to openly share accident investigation and enquiry results, as well as planned changes and developments.

5. Managing Risks and Hazards: Whereas OHSAS 18001 is just aimed on controlling hazards, ISO 45001 encourages 'risk-based thinking' to identify and treat risks. In tune with the recent ISO standards, ISO 45001 has adopted a more proactive, flexible and preventative approach based on dealing with a broader range of risks before they precipitate.

ISO 45001 also lays greater emphasis on opportunities by encouraging organisations to scope, evaluate and utilize these opportunities for continuous improvement instead of simply reacting to non-conformances. It also includes an expanded section on preparing for and responding to emergency situations, thus providing a more holistic perception of health and safety risk.

6. Wide-ranging Planning: ISO 45001 has greater stress than OHSAS 18001 with respect to enacting organisational goals, connecting them to health and safety objectives, fixing priorities and generating documentation for the same. With stronger emphasis on planning and setting objectives in tune with the resource availability, staff accountability, and timelines etc.

7. Mental health, stress and fatigue: Mental health is now widely recognised as part of total health in occupational health

background. Though it is not singularly stated in ISO 45001, there are several areas of ISO 45001 where mental health is mentioned and regarded as an important component of health e.g., Clause 4.2 (the needs of workers and interested parties include mental wellbeing), Clause 6.1.2.1 (employee stress and fatigue as part of hazard/risk identification); Clause 6.2 (integration of mental health in health and safety improvement objectives and plans); Clause 8.1.2 (treating mental health risks and lowering the score of their residual risk).

8. Terminology: Except three terms, none of the total 37 definitions and terms used in the ISO 45001 are identical with those in OHSAS 18001. For example, it now defines 'worker' and 'workplace', and replaces the term 'documents and records' with 'documented information' indicating broader scope of the standard.

Conclusions

The issue Health and safety at workplace is one of the most important concern for any organization. ISO 45001, as a global standard for Occupational Health and Safety Management Systems provides a practical solution to improve the safety and occupational health of both employees and other personnel. This standard has been designed with an intention to be applicable for any workplace regardless of its size, type and nature. There are numerous benefits for implementing ISO 45001. It is an excellent management system that aims to reduce health and safety risks within the workplace and places the protection of employees' health at the forefront of all processes and planning.

Acknowledgement

The author is grateful to the present Director of Health, Safety and Environment Group, BARC (formerly director of CSIR-National Physical Laboratory, New Delhi) for his keen interest and guidance in the field of standardization and best practices, and constant encouragement in carrying out scientific research, reviews, and publication.

References

- [1]. "ISO members" (2021). International Organization for Standardization <https://www.iso.org/members.html>
- [2]. "Let the migration begin" (2018). International Organization for Standardization <https://www.iso.org/members.html>



Dr. A.P. Tiwari, Director, KMG (right) and Dr. Soumyakanti Adhikari, Head, SIRD hand over to a participant of the student contingent from Gujarat a book on non power applications of nuclear technologies during a program at DAE Convention Centre.

Students from Gujarat pose for a group photo at the program venue.

Students of Gujarat visit Trombay

Students of Gujarat who have excelled in a state-wide STEM Quiz conducted by the State Council for Science and Technology during early 2022 have been provided an opportunity to interact with the BARC scientific community directly by visiting the Trombay campus on 18th of June.

The day before their visit to BARC Trombay campus, the twelve students and their instructors had been to Tata Institute of Fundamental Research, an institute which has gained significant reputation as a centre of excellence for pure and applied research in physics and mathematics in India. Here, students closeted with the scientists to make good sense of the work being pursued unrelentlessly over the years by the scientific community.

After cosying up to the warm hospitality extended by BARC at the newly created DAE Convention Centre in Anushaktinagar soon after their arrival in the evening hours of 17th, these students went to bed with high hopes realising the fact that the “experience (for which) we have been waiting so keenly ever since” is set to unfold the following day.

“As soon as I came to know (the fact that) we would get a chance to enter BARC, I couldn’t control my anxiety levels,” said a student when asked about his initial impression after the visit. In the midst of nature’s abode, these students “enjoyed every moment” in the company of scientists as they visited Dhruva facility, Modular Laboratories, Nuclear Agriculture and Biotechnology labs as well as those housing the Food Technology facilities.

The second half of the day, students paid attention to presentations on research reactors of BARC and the life saving role of radioisotopes, which originate primarily in these reactors and are processed in later stages before they are

dispatched to hospitals for treating various life-threatening diseases, including cancer.

Following this, a skit was enacted in which the performing characters (BARC staff) have addressed the unfounded myths associated with the nuclear energy by employing a mix of popular songs and folk to shed the potential negative publicity about nuclear energy activities. The research activities under nuclear agriculture and biotechnology in BARC have so far yielded 52 new varieties of crops and the finer aspects of this activity have been covered in a presentation for the students, which according to them was “quite informative”.

In the last leg of the program, each of the 12 students were presented with certificates of appreciation signed by Director of Knowledge Management Group as well as a hard copy of the book entitled ‘Non-power Applications of Nuclear Technologies’, edited by Director BARC and Director of Chemistry Group. BARC bid adieu to the students on 19th of June.

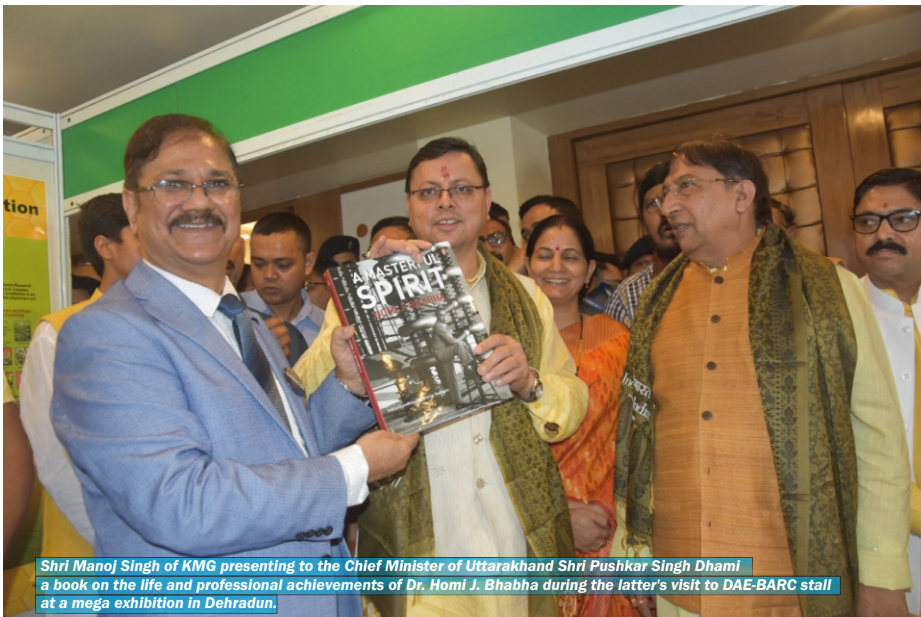
Mega Exhibition in Dehradun

‘Rise in Uttarakhand – A Mega Exhibition’ - has been promoted by the state government and it saw participation from various scientific research bodies under the ambit of state as well as the union government, including DAE, ISRO, DRDO and CSIR. Besides, state-run industrial units, rural cooperative bodies constituted by women self help groups too participated by setting up their stalls at the event.

As per the organisers, the event was planned to bring both industry as well as general public under a single roof so as to facilitate sharing of prospective ideas, which may result in setting up of new industrial units and contribute to job opportunities for the young and educated people of the state.



A majority of the visitors at DAE exhibition in Dehradun expressed deep sense of satisfaction on the positive contributions made by DAE and its constituent units in making India self reliant in several highly sophisticated technology domains over the last more than seven decades.



Shri Manoj Singh of KMG presenting to the Chief Minister of Uttarakhand Shri Pushkar Singh Dhama a book on the life and professional achievements of Dr. Homi J. Bhabha during the latter's visit to DAE-BARC stall at a mega exhibition in Dehradun.



Children converge at the DAE-BARC stall in Dehradun to know about the activities of atomic energy.



The students of Ramakrishna Mission Residential College, Narendrapur in Kolkata pose for a group photo alongside senior officials of DAE.

School students and engineering graduates of prominent institutes situated in the vicinity as well as far-flung areas of Dehradun thronged the three-day exhibition in a major way, which began on 7th of July. Prominent individuals who visited the event include Chief Minister of Uttarakhand Shri Pushkar Singh Dhama, a Rajya Sabha member from the state and various cabinet level ministers of the state government.

At the event, the Department of Atomic Energy was represented by Bhabha Atomic Research Centre (BARC). The BARC stall was attended by two officers of Scientific Information Resource Division, who engaged with the visitors constructively and gave them a detailed account on the multi-diversified nature of scientific research in the centre and also new innovations to support the growth of nuclear energy activities in India. R&D activities of BARC which are specific to the state of Uttarakhand, such as rejuvenation of ageing springs in the upper reaches of Himalayan ranges were increasingly brought to the notice of the visitors to the stall.

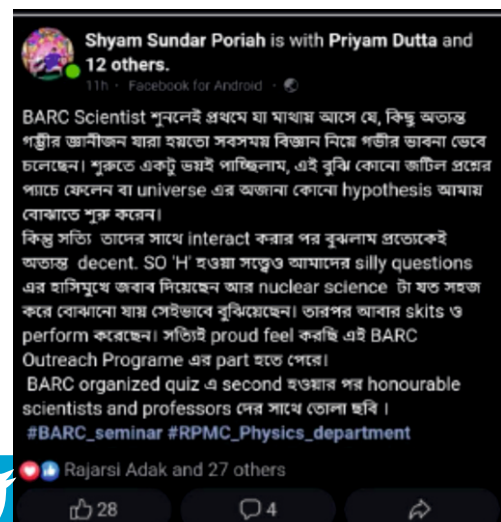
A majority of the visitors expressed deep sense of satisfaction on the positive contributions made by DAE and its constituent units over the last more than seven decades in making India self reliant in several highly sophisticated technological domains

DAE scientists warm up to students in Kolkata

As part of their mission to educate young minds on the positive benefits of nuclear energy, senior officers of several DAE units, including BARC, VECC, BRIT have visited colleges in the vicinity of Kolkata during April 26th-30th, 2022, including to Ramakrishna Mission Residential College in Narendrapur; Vijaygarh Jyotish Ray College in Jadavpur; College Square campus of University of Calcutta, and Raja Peary Mohan

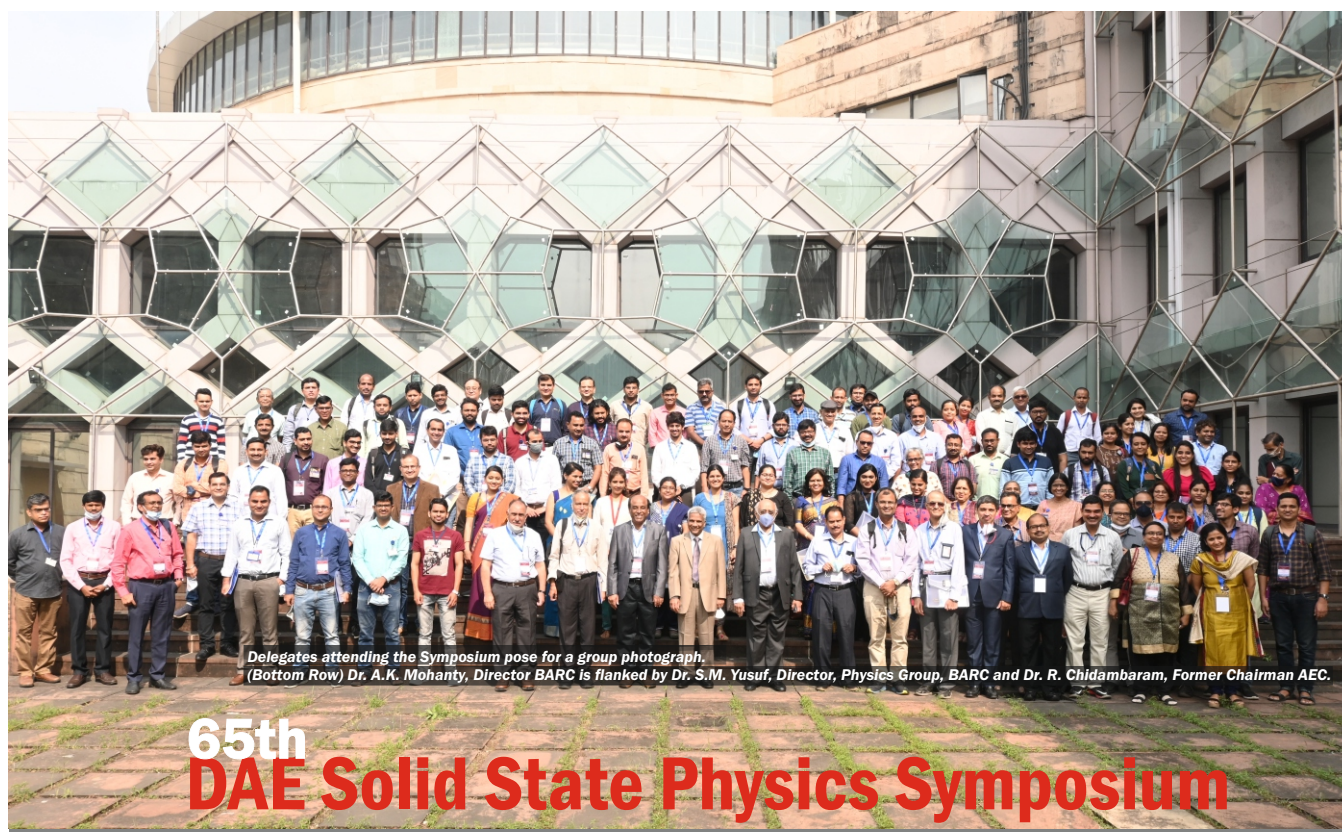
College in Hooghly.

The program included presentation by scientists on multi topics such as on Nuclear Reactors, The World of Neutrinos, Innovation and Career Opportunities in DAE, Applications of Radiation and Radioisotopes in Agriculture and Healthcare etc. To strike a positive chord with the students and to also drive home the message properly, stage plays were performed on nuclear energy by making use of terminology which forms part of our daily routine. In addition, quiz programs were organized and the winning students were recognized and feted properly.



“...Despite being senior scientists with designation of SO/H, they answered all of our silly questions smilingly and made us understand ‘Nuclear Science’ in a simplest way. They have performed skits also. I really feel proud to be part of this ‘BARC Outreach Programme’...”

Reports from symposia, workshops and conferences



The latest edition of Solid State Physics symposium was organized at DAE Convention Centre in Mumbai recently. The symposium had been sponsored by BRNS and the scientific program was planned and organized by Physics Group, BARC.

Three outstanding plenary talks were delivered on specialized topics, including on *Bandgap of Disordered Semiconductors in relation to Optoelectronic* by Prof. Amlan J. Pal, UGC-DAE CSR, Indore, *Advanced Magnetic X ray Spectro-microscopies of Novel Topological Spin Textures* by Prof. Peter Fischer of Lawrence Berkeley National Laboratory at Berkeley CA; *Multi-scale Modelling of Nanomaterials: From Nanotubes to Ants* by Prof. Douglas S. of Galvao State University of Campinas and Brazilian Academy of Sciences, Brasil.

4 Young Achievers, 6 best Ph.D. theses, 26 posters have been recognized and were duly awarded with at the event. The proceedings of the symposium have been uploaded online in DAE SSPS website (www.daessps.in) with ISBN number: 81-8372-085-4.



Phase transitions and dynamics

Soft Condensed Matter including Biological Systems

Nano-materials

Experimental Techniques and Devices

Glasses and Amorphous Systems

Surfaces, Interfaces and Thin Films

Computational Methods and Electronic Structures

Single Crystals Growth and Characterization

Transport Properties

Semiconductor Physics

Magnetism, Superconductivity, and Spintronics

Energy Materials

TSRP-2022

A Symposium on Radiation & Photochemistry



Proceedings of TSRP-2022 released during the Inaugural Function.
(R-L) Dr. Awadhesh Kumar (Head, RPCD), Dr. A.K. Mohanty (Director, BARC),
Dr. A.K. Tyagi (Director, Chemistry Group, Dr. J. Mohanty (RPCD) and Dr. P. Mathi (RPCD).

The 16th DAE-BRNS 'Trombay Symposium on Radiation & Photochemistry' (TSRP-2022) was held virtually during January 12-15 this year at BARC Training School in Mumbai.

The Radiation & Photochemistry Division (RPCD) of Chemistry Group alongside Indian Society for Radiation and Photochemical Sciences (ISRAPS) organized the program, which included 16 scientific sessions comprising 4 plenary lectures and 30 talks by invited experts.

The proceedings of the entire program have been covered in detail in a souvenir, which was released by Dr. A.K. Mohanty, Director, BARC during the inaugural event. A special ISRAPS bulletin was also unveiled at the program. 250 delegates, including 26 eminent scientists from India and abroad from the ranks of several reputed R&D institutes attended the 4-day program.

The fundamental aspects of Photo and Radiation Chemistry, Chemical and Biological Applications of Radiation and Photochemistry, Ultrafast Processes, Chemical Kinetics and Dynamics at Interfaces, Metal and Semiconductor Nanoparticles, Radiation Induced Synthesis of Polymers, Nonlinear Spectroscopy, Energy and Electron Transfer, Development of Light Energy Conversion Devices, have been covered in the form of talks and presentations by the participants.

Meritorious persons have been recognized by awarding them with Dr. Harimohan Memorial Award in Radiation Chemistry and Dr. P.K. Bhattacharya Award in Photochemistry during the program.

Fundamental aspects of Photo and Radiation Chemistry

Chemical and Biological Applications of Radiation and Photochemistry

Ultrafast Processes

Chemical Kinetics and Dynamics at Interfaces

Metal and Semiconductor Nanoparticles

Radiation Induced Synthesis of Polymers

Nonlinear Spectroscopy

Energy and Electron Transfer

Development of Light Energy Conversion Devices

Symposium topics

Tarun Datta Memorial Award to BARC scientist

Dr. Tirumalesh Keesari, a Scientific Officer in Isotope Hydrology Section of Isotope Radiation and Application Division (BARC), recently received the prestigious Tarun Datta Memorial Young Scientist Award in recognition of his outstanding contributions in the field of nuclear and radiation chemistry – “fundamental or applied research”.

The Indian Association of Nuclear Chemists and Allied Scientists (IANCAS) presents the annual Tarun Datta Memorial Young Scientist Award to scientists for their outstanding contributions in the field of Nuclear and Radiochemistry.

Dr. Keesari's research interests include water contamination, geochemical modeling, groundwater recharge, spring revival in Himalayan regions, coastal salinity and studies on extreme climatic regions of India. He is currently working on the application of isotope technology employing environmental isotope and injected tracers for sustainable water resources management.

In the recent past, Dr. Keesari played a pivotal role in the application of isotope technology consisting of environmental isotopes (^2H , ^{18}O , ^{13}C , ^{34}S , ^3H , ^{14}C , ^{222}Rn) and injected tracers (^3H , ^{82}Br) for sustainable water resources management. Besides this, he was also successful in delineating the anthropogenic and natural sources for fluoride contamination in many parts of India through isotope finger-printing. His endeavor has benefited water authorities from fluoride impacted regions of Talcher (Odisha), Nalgonda (Telangana), Bagalkot (Karnataka)



Dr. Tirumalesh Keesari working on samples at a dedicated laboratory.

and central parts of Rajasthan in planning effective remediation protocols. Through application of reactor produced tracers (^{82}Br and ^3H), he has accurately demarcated the susceptible zones for contaminant migration in groundwater of Indian Rare Earths Ltd. site (Kerala) and saltpan areas in Mahim and Kelwe regions (Maharashtra). These results were crucial in adopting suitable preventive measures.

Dr. Keesari has over 80 international journal publications to his credit and is also a recipient of DAE Science and Technology Award and Indo-US Science and Technology Award. He is an Associate Professor in Chemical Sciences in Homi Bhabha National Institute, Mumbai.

This page is intentionally left blank



Dhruva Research Reactor Facility (Inside view)

Edited & Published by
Scientific Information Resource Division
Bhabha Atomic Research Centre, Trombay, Mumbai-400 085, India
BARC Newsletter is also available at URL:<http://www.barc.gov.in>